REPORT DOCUMENTATION PAGE

Form Approved
OMB NO. 0704-0188

1. AGENCY USE ONLY (Leave Blank)	2. REPORT DATE	3. REPORT TYPE AND DATES COVERED
	November 25, 2002	Final Technical Report, 4/1/98 –3/31/01

4. TITLE AND SUBTITLE

Development of an All Solid-State Raman Image Amplifier

5. FUNDING NUMBERS

DAAG55-97-1-0331

6. AUTHOR(S)

R.C. Powell, L.K. Calmes, J.T. Murray

7. PERFORMING ORGANIZATION NAME(S) AND ADDRESS(ES)

Optical Sciences Center   University of Arizona
Tucson, AZ 85721

8. PERFORMING ORGANIZATION REPORT NUMBER

9. SPONSORING / MONITORING AGENCY NAME(S) AND ADDRESS(ES)

U. S. Army Research Office
P.O. Box 12211
Research Triangle Park, NC 27709-2211

10. SPONSORING / MONITORING AGENCY REPORT NUMBER

11. SUPPLEMENTARY NOTES

The views, opinions and/or findings contained in this report are those of the author(s) and should not be construed as an official Department of the Army position, policy or decision, unless so designated by other documentation.

12 a. DISTRIBUTION / AVAILABILITY STATEMENT

Approved for public release; distribution unlimited.

12 b. DISTRIBUTION CODE

13. ABSTRACT (Maximum 200 words)

This report describes a new type of eye-safe, range-gated lidar sensing element based on solid-state Raman image amplification (SSRIA) in a solid-state optical crystal. SSRIA can amplify low-level images in the eye-safe infrared at 1.556 µm with gains up to 10^6 with the addition of only quantum-limited noise. The high gains from SSRIA can compensate for low quantum efficiency detectors and can reduce the need for detector cooling. The range-gate of SSRIA is controlled by the pulse width of the pump laser and can be as short as 30 – 100 cm, using pump pulses of 2 – 6.7 nsec FWHM. A rate equation theoretical model is derived to help in the design of short-pulsed Raman lasers. A theoretical model for the quantum noise properties of SSRIA is presented. SSRIA results in higher SNR images throughout a broad range of incident light levels, in contrast to the increasing noise factor with reduced gain in image intensified CCD's. A theoretical framework for the optical resolution of SSRIA is presented and it is shown that SSRIA can produce higher resolution than ICCD's.

14. SUBJECT TERMS

Image amplifier; lidar; Raman effect

15. NUMBER OF PAGES

130

16. PRICE CODE

17. SECURITY CLASSIFICATION OR REPORT	18. SECURITY CLASSIFICATION ON THIS PAGE	19. SECURITY CLASSIFICATION OF ABSTRACT	20. LIMITATION OF ABSTRACT
UNCLASSIFIED	UNCLASSIFIED	UNCLASSIFIED	UL

NSN 7540-01-280-5500

Standard Form 298 (Rev.2-89)
Prescribed by ANSI Std. 239-18
298-102

Enclosure 1

20030227 105

SOLID STATE RAMAN IMAGE AMPLIFICATION

Final Report on Army Research Office Grant DAAG55-97-1-0331

November 25, 2002

Written by Lonnie K. Calmes
In partial fulfillment of the requirements for the Doctor of Philosophy Degree

Under the supervision of Principal Investigator Professor Richard C. Powell
With the assistance of Dr. James T. Murray

TABLE OF CONTENTS

LIST OF ILLUSTRATIONS

LIST OF ILLUSTRATIONS - *Continued*

LIST OF TABLES

ABSTRACT

Amplification of low-light-level optical images is important for extending the range of lidar systems that image and detect objects in the atmosphere and underwater. The use of range-gating to produce images of particular range bins is also important in minimizing the image degradation due to light that is scattered backward from aerosols, smoke, or water along the imaging path. For practical lidar systems that must be operated within sight of unprotected observers, eye safety is of the utmost importance. This thesis describes a new type of eye-safe, range-gated lidar sensing element based on Solid-state Raman Image Amplification (SSRIA) in a solid-state optical crystal. SSRIA can amplify low-level images in the eye-safe infrared at 1.556 μm with gains up to 10^6 with the addition of only quantum-limited noise. The high gains from SSRIA can compensate for low quantum efficiency detectors and can reduce the need for detector cooling. The range-gate of SSRIA is controlled by the pulsewidth of the pump laser and can be as short as 30 – 100 cm, using pump pulses of 2 – 6.7 nsec FWHM. A rate equation theoretical model is derived to help in the design of short pulsed Raman lasers. A theoretical model for the quantum noise properties of SSRIA is presented. SSRIA results in higher SNR images throughout a broad range of incident light levels, in contrast to the increasing noise factor with reduced gain in image intensified CCD's. A theoretical framework for the optical resolution of SSRIA is presented and it is shown that SSRIA can produce higher resolution than ICCD's. SSRIA is also superior in rejecting unwanted sunlight background, further increasing image SNR. Lastly, SSRIA can be combined with optical pre-filtering to perform optical image processing functions such as

high-pass filtering and automatic target detection/recognition. The application of this technology to underwater imaging, called Marine Raman Image Amplification (MARIA) is also discussed. MARIA operates at a wavelength of 563 nm, which passes most efficiently through coastal ocean waters. The imaging resolution of MARIA in the marine environment can be superior to images produced by laser line scan or standard range-gated imaging systems.

1   Introduction

1.1 Motivation for Research

The desire to operate atmospheric lidar (light detection and ranging) systems in the "eye-safe" wavelength region around 1.56 μm has motivated much research into new laser sources and the use of nonlinear optical elements to shift the fundamental laser source to the desired wavelength. The region around 1.56 μm is advantageous because this wavelength is not transmitted to the retina of the eye as is the 1.06 μm line of Nd:YAG or visible lines of other lasers.[1] This allows the use of greater energy pulses for illumination of scenes of interest without endangering surrounding personnel. Pulsed lidar systems use the technique of "range gating" to reject the intervening scattered light due to smoke or fog. Range gating is typically accomplished by controlling the timing between the outgoing laser pulses and the gating or exposure of the sensing element of the lidar system.[2]

The sensing element of an imaging lidar system is usually an intensified CCD (Charge Coupled Device) array or a streak tube / CCD array combination.[2] Image intensifier tubes operate by using a photoemissive detector coupled to a microchannel plate (MCP) electron amplifier. The gating of the intensifier is accomplished by switching the voltage between the photocathode and the input of the MCP while the gain is controlled by adjusting the high voltage across the MCP.[3] Current commercial image intensifiers are limited to gains of around 10^5, gating times of around 20 nanoseconds, and resolutions of around 50 to 100 μm at the photocathode. In addition, infrared photocathodes suffer from low quantum efficiencies that limit the achievable signal to noise ratio of images.

The contents of this dissertation introduce a new technique for image amplification that uses stimulated Raman scattering in solid-state crystals. Solid-state Raman Image Amplification (SSRIA) offers the potential of extended gain, much shorter gating times, lower noise, and higher resolution than conventional image intensifiers.

1.2 Discovery of Raman Scattering

In 1928, C. V. Raman discovered the inelastic light scattering phenomenon that now carries his name.[4,5] Raman discovered that the spectra of light scattered by liquid benzene included a component that was downshifted in frequency from the original light source. He pointed out that the frequency change was related to the infrared vibrational frequencies of the molecules of the liquid. Almost simultaneously, the Russian physicists G. Landsberg and S. Mandel'shtam discovered the same effect in light scattering experiments from crystalline quartz.[6] For his discovery of Raman scattering and his other researches into the diffusion of light, Raman was awarded the Nobel Prize in 1930.

Raman's experimental discovery was anticipated by theoretical work that predicted the associated change of frequency in inelastic light scattering. In 1923, the Russian physicist, A. Smekal, considered light scattering from an energy conservation point of view.[7] Smekal showed that an atom of mass M in an energy state E_l moving with a velocity v can, upon collision with a photon of energy $\hbar\omega$, make a transition to another energy state E_k and also experience a change of velocity to v'. From the principle of conservation of energy these quantities are related by Equation (1.1)

$$\frac{1}{2}Mv^2 + E_l + \hbar\omega = \frac{1}{2}Mv' + E_k + \hbar\omega' \qquad (1.1)$$

where $\hbar$ is Planck's constant and ω' is the frequency of scattered light. Smeckal showed that the change in velocity was negligible so that

$$E_l + \hbar\omega = E_k + \hbar\omega' \qquad (1.2)$$

or, rearranging

$$\omega' = \omega - \frac{(E_k - E_l)}{\hbar} \qquad (1.3)$$

which is interpreted to mean that the photon gives up some of its energy to the atom and is scattered with less energy. This is Raman scattering. If the change in light frequency is zero and the atom does not change its state l, then the process is known as Rayleigh scattering.

In 1925, H. A. Kramers and W. Heisenberg published a landmark paper in quantum mechanics that considerably amplified Smekal's simple ideas.[8] In this paper, Kramers and Heisenberg showed that not only is it possible to produce scattered light that is red shifted as described by Equation (1.3), but also the converse process is possible, whereby the atom loses energy and the scattered light is blue shifted. In modern terminology, Raman scattering that produces red shifted light is called Stokes shifted, for Sir George Stokes, who studied fluorescence.[9] Blue shifted light is now called anti-Stokes shifted. Kramers and Heisenberg also introduced the concepts that light scattering with frequency change is incoherent (in the spontaneous Raman scattering regime) and that the process must occur by way of a virtual intermediate state m.

Raman made his discovery using filtered sunlight as the illumination source. After the discovery and subsequent follow-up papers, further work on the Raman effect soon

transferred to the field of chemistry, where Raman scattering was exploited as an analytical tool. Progress in the field seemed to stagnate until the invention of the laser brought a sudden revival of interest and work in Raman scattering. The higher intensities and electric fields produced by lasers induce polarizations in a molecule or atom that are nonlinear in the field. In conventional Raman scattering (i.e. the type of effect studied by Raman using weak light sources), the strength of the induced polarization is linearly proportional to the electric field strength. With the higher field strength of a laser, the polarization becomes nonlinear in the electric field, involving the square, cube, etc. of the incident electric field. The most useful nonlinear effect of this type is called stimulated Raman scattering.

1.3 Stimulated Raman Scattering

Stimulated Raman scattering (SRS) was first observed in 1962 by Woodbury and Ng[10] while studying Q-switching of a ruby laser with a nitrobenzene Kerr cell. They observed an infrared component in the laser output at a frequency that was downshifted by 1345 cm^{-1} from the laser frequency. Woodbury and Eckhardt[11] recognized that this infrared component must result from stimulated Raman emission in nitrobenzene. SRS can be described classically as a parametric generation process with one of the electromagnetic waves replaced by a material excitation wave (phonon). Early interest in SRS arose because it could provide intense coherent radiation at new wavelengths and because it was a possible loss mechanism in propagating high-power laser beams through the atmosphere or in a laser fusion plasma. Consequently, most work involved the study of SRS in gases, both in the atmosphere and in gas cell mixtures. In particular, SRS from

H_2 gas has been studied extensively.[12] Typically, SRS from H_2 gas produces intense Raman output from a gas cell of about a meter long at a few atmospheres pressure using a visible laser intensity of several megawatts per square centimeter.

1.4 SRS in Gas Cells

In the 1980's, research in the area of laser fusion led to the investigation into using SRS gas cells as high power Raman amplifiers. Partanen and Shaw[13] investigated the use of low-pressure molecular hydrogen in a light guide as a beam combiner for a high-power KrF laser. Such a Raman amplifier may be used in the forward direction as an optical beam combiner where many pump beams are combined into a single Stokes beam. As shown by Partanen and Shaw and others, such an amplifier need not imprint phase or intensity variations onto the Stokes beam, and nearly distortionless amplification can be obtained. Recently, researchers at the Naval Research Laboratory have investigated the use of a gas cell, stimulated Raman amplifier for low-light-level, quantum-noise-limited amplification of images.[14]

1.5 SRS in Solid-State Crystals

Researchers at Lite Cycles, Inc., and the University of Arizona Optical Sciences Center have been investigating SRS in solid-state nonlinear crystals. SRS in solid-state media offers the advantage of very high Raman gain in a more compact, rugged design. Work to date at Lite Cycles and the University of Arizona Optical Sciences Center has concentrated on the generation of 1.56 μm radiation through intracavity solid-state Raman shifting in $Ba(NO_3)_2$ nonlinear crystals.[15] Intracavity Raman lasers offer the

unique ability to convert a highly multi-spatial-mode pump beam into a near-diffraction-limited output beam. Such high-brightness, eye-safe beams are ideal for illuminating the object of a pulsed lidar imaging system. In addition, intracavity solid-state Raman lasers can be designed to produce temporally short pulses through the process known as nonlinear cavity dumping. This is also important in lidar systems, as the range resolution of a gated lidar system is a function of the convolution of the illuminating laser pulse and the optical gatewidth of the receiver. Chapter 2 of this dissertation discusses the dynamics of intracavity Raman lasers and shows how short output pulses are a natural outcome of intracavity Raman conversion. A rate equation model for the intracavity Raman laser is derived and model calculations are presented.

1.6 Raman Image Amplifiers

The high Raman gain of solid-state nonlinear crystals and the possibility of distortionless amplification suggest the use of these crystals for the amplification of optical images. Stokes wavelength light reflected from an object can be imaged through a Raman crystal amplifier that is pumped by a pulsed laser. The image light acts as a Stokes seed for SRS in the crystal. The initially weak image light can be amplified greatly by SRS and then relayed to an optical detector. In addition, because the Raman gain in the crystal is a function of the pump intensity, the Raman image amplifier can produce range-gated images through control of the timing between the returned Stokes image pulse and the amplifier pump pulse.

Similar work has been done using SRS gas cells. Duncan[14] and others at the Naval Research Laboratory have investigated the noise characteristics and the low-light-level

imaging capabilities of a gas cell, stimulated Raman amplifier. Their studies used collinear pumping of a 1-meter long cell filled with molecular hydrogen at 20 atmospheres. They used both direct imaging and Fourier-transform imaging of the Stokes signal through the Raman amplifier with an amplifier gain of 3×10^4. Duncan, et. al., concluded that Raman amplification can be used with input signal levels approaching the quantum limit of one photon per amplifier mode. They also concluded that Fourier-transform amplification might have advantages for minimizing noise levels as well as potential advantages in maximizing the field of view.

Moon, et. al.[16], have demonstrated three-dimensional reflective image reconstruction through a scattering medium based on time-gated Raman amplification in a H_2 gas cell. Using a frequency doubled, Q-switched, mode-locked Nd:YAG laser producing 30 ps pulses at 532 nm, they demonstrated less than 1-cm depth resolution through a distance of more than 8 attenuation lengths of turbid material. Their experimental design used an optical delay arm to vary the delay times of the pump pulse for the Raman amplifier. They made the projection that for an illumination level of 1 J per pulse, 10^4 pixels per image, and an overall object reflectivity/collection efficiency of 10^{-3}, an imaging depth of ~13 attenuation lengths should be possible. This corresponds to imaging through 27 meters of typical coastal water with an attenuation length of 2 meters.

In Chapter 3 of this dissertation, the theory of Raman image amplification is presented with a particular emphasis on solid-state nonlinear crystals. Chapter 3 shows that high gains can be attained using Raman crystals of approximately 1 cm. x 1 cm. x 5 cm. size, in contrast to H_2 gas cells which require cells of about 1 meter in length. Chapter 3 also

contains a derivation of the noise properties of Raman image amplifiers. Although the Raman image amplification process does add noise to the incoming signal, it will be shown in Chapter 3 that this noise is the minimum required by quantum theory and is more than offset by the high preamplification gain provided by SSRIA.

Chapter 4 contains a discussion of the optical design aspects of Raman image amplifiers such as the achievable field-of-view and the limiting optical resolution.

Chapter 5 contains results of an experimental demonstration of SSRIA. The experiment consists of three main optical parts: 1.) a Stokes seed source laser, which is a Q-switched, flashlamp-pumped, intracavity Raman laser emitting up to 30 mJ per pulse of 1.56 μm radiation at a 1 Hz repetition rate, 2.) a Raman amplifier pump laser, which is a Q-switched, flashlamp-pumped Nd:YAG laser emitting up to 89 mJ per pulse of 1.34 μm radiation at a 1 Hz repetition rate, and 3.) the Solid-state Raman Image Amplifier which is configured in a Fourier transform arrangement where the amplifier crystal is at the Fourier transform plane of the input image.

1.7 Applications of Raman Image Amplification

Solid-state Raman image amplification has the potential to improve on the current state of image intensifier and streak tube performance, particularly in the infrared where photocathode intensifiers have poor quantum efficiency. It offers the potential of being less expensive, simpler, more rugged, and having higher performance than current sensor devices.

Applications for military use include eye-safe imaging lidars that can be used for autonomous vehicle identification and targeting at 20 km and greater ranges, such as

required by the Air Force. Reduced background radiation through narrow receiver spectral bandwidths and increased range resolution from short amplifier laser pulsewidths are realizable with SSRIA sensors. The increased range resolution will also improve clutter rejection. SSRIA also has the potential to perform optical image processing functions that will allow automatic target recognition or aimpoint designation in real-time without the need for extensive digital signal computations. This is readily accomplished in SSRIA by pre-filtering the optical image before amplification. Matched-filtered output from the image amplifier can be obtained. A suitable threshold can then be applied to the amplified image to produce an all-optical, automatic target recognition process.

Other military applications include underwater imaging of mines and submarines. Underwater imaging of objects during daylight hours requires methods to reduce the sunlight reflected from the water surface into the camera or sensor. These reflected sunlight glints could overwhelm a lidar signal return from under the water, even with narrow bandpass filters in front of the camera lens. Sub-nanometer receiver spectral bandwidths can be realized with the SSRIA receiver, enabling a system to image underwater objects with less degradation from the sun. Any imaging application that requires high range resolution - limited by the amplifier laser pulse width - could be realized from the SSRIA sensor.

Medical applications include imaging through highly scattering media. The SSRIA sensor would enable amplification and detection of ballistic photons transmitted through tissue with very high range resolution. This resolution would enable production of 3-dimensional images of small, millimeter-dimension targets such as tumors. By using

mode-locking technology, the Raman illuminator and amplifier pump laser pulses can be temporally compressed to tens of picoseconds FWHM. The resulting gate for Raman imaging would allow separation of the "ballistic" photons, which pass unscattered through soft tissue, from the multiply scattered photons, which would normally mask the desired image. Mahon, et al., have demonstrated that features as small as 125 μm can be imaged through dense scattering media with light extinction factors of up to e^{-33} using Raman image amplification in Hydrogen gas.[17] By using solid-state Raman image amplification, a medical imaging device can be made smaller and more compact, with even higher spatial resolution. This technology could result in much earlier detection of carcinomas, particularly those associated with melanomas.

Chapter 6 discusses the optical design issues of these applications, including issues in the design of eye-safe imaging lidar and issues in the design of an underwater lidar system based on Raman image amplification.

Chapter 7 presents conclusions drawn from this study and points to future directions of study.

2 Temporal Dynamics of Raman Lasers

2.1 Rate Equation Model

The physical system that is modeled in this chapter is shown schematically in Figure 2.1-1. It consists of a solid-state, Nd-doped, YAG laser crystal between two mirrors which are highly reflecting at 1.34 μm. The Nd:YAG is optically pumped by a flashlamp. In another optical cavity that shares one of the highly reflecting mirrors of the 1.34 μm optical cavity, there is a $Ba(NO_3)_2$ nonlinear Raman crystal. The other mirror of the 1.56 μm Raman cavity is a partially reflecting output coupler. An intracavity telescope is included in the 1.34 μm cavity that reduces the beam radius of the 1.34 μm light inside the Raman crystal. A Pockels cell Q-switch is also present in the fundamental cavity to rapidly switch the optical loss in the cavity and to produce giant pulse output.
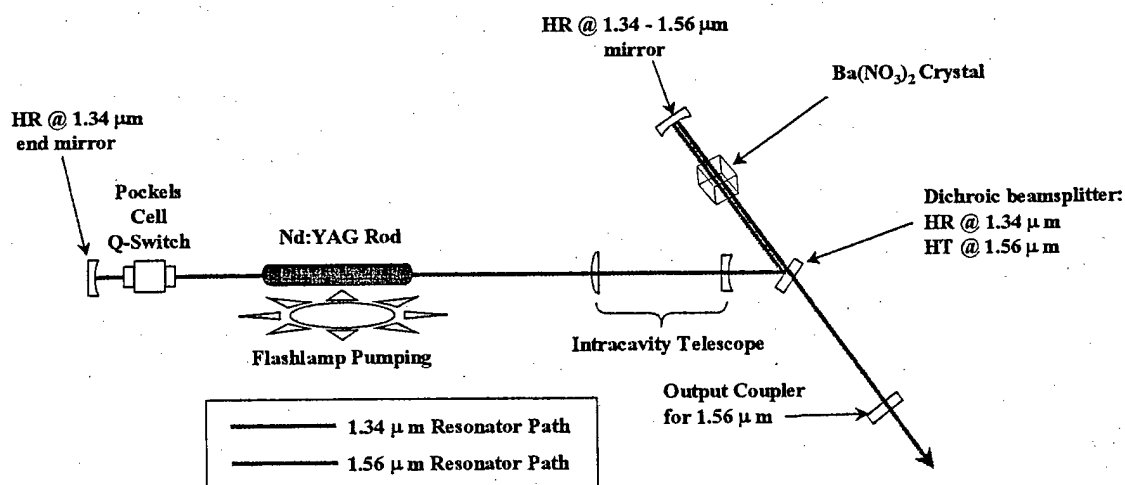
Figure 2.1-1 Coupled cavity Raman laser

Consider first the amplification of light in the Nd:YAG rod. Figure 2.1-2 shows a schematic diagram of the physical process of light amplification.
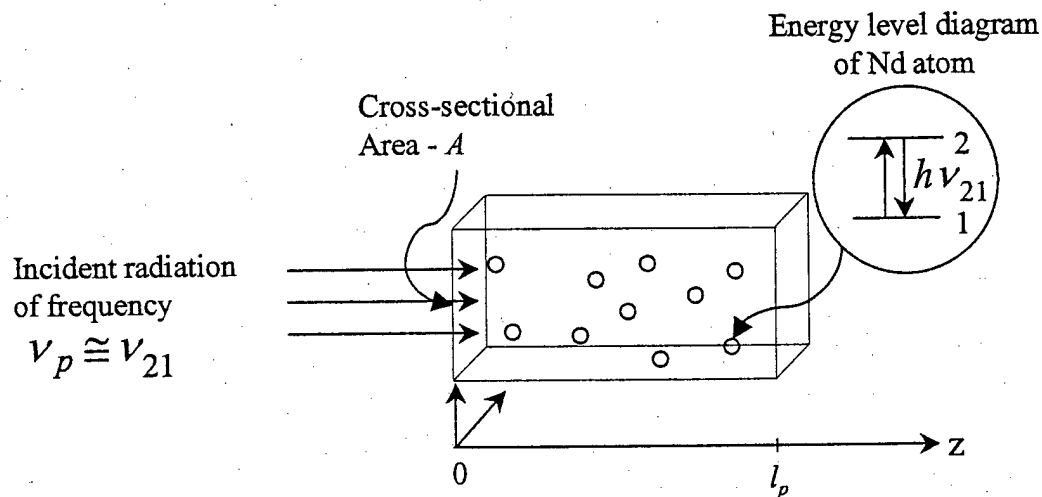
Figure 2.1-2 The propagation of radiation of frequency $v_p \cong v_{21}$ in a medium of atoms with a transition frequency v_{21}.

The incident radiation is assumed to be a quasi-monochromatic plane wave of frequency v_p and irradiance I_p, $\left(W/cm^2\right)$, propagating in the +z direction (p represents "pump" since the fundamental at 1.34 μm is the pump for the Raman process). The rate at which electromagnetic energy passes through the plane of cross-sectional area A at z is $I_p(z)A$.

At an adjacent plane at $z + \Delta z$, the rate is $I_p(z + \Delta z)A$ and the difference is:

$$\left[I_p(z + \Delta z) - I_p(z)\right]A = \frac{\partial}{\partial z}\left(I_p A\right)\Delta z \qquad (2.1)$$

in the limit of very small Δz. Equation (2.1) gives the rate at which electromagnetic energy leaves the volume $A\,\Delta z$. In terms of the energy density u_p of the light, the rate balance can be written:

$$-\frac{\partial}{\partial t}\left(u_p A \Delta z\right) = \frac{\partial}{\partial z}\left(I_p A\right)\Delta z \qquad (2.2)$$

A and Δz are constant, and $u_p = I_p/c$, where c is the speed of light, so Equation (2.2) can be written as:

$$\frac{1}{c}\frac{\partial}{\partial t}I_p + \frac{\partial}{\partial z}I_p = 0. \qquad (2.3)$$

This equation is called the *equation of continuity*, and is an example of Poynting's theorem, in one space dimension.[18] Equation (2.3) applies to a plane wave propagating in a vacuum. For a wave that is propagating in a medium, the zero on the right hand side of this equation must be replaced by the rate per unit volume at which electromagnetic energy changes because of the medium. This rate of change is proportional to the rate of change of the population inversion density, n, in the medium, and modifies the equation of continuity to:

$$\left(\frac{1}{c}\frac{\partial}{\partial t} + \frac{\partial}{\partial z}\right)I_p = \sigma_p I_p n \qquad (2.4)$$

where σ_p is the stimulated emission cross-section of the pump $\left(cm^2/atom\right)$, and n is the population inversion density $\left(atoms/cm^3\right)$.

In a resonant cavity, there are both right- and left-going waves inside the medium. This leads to two equations of continuity:

$$\frac{\partial I_p^+}{\partial z} + \frac{1}{c}\frac{\partial I_p^+}{\partial t} = \sigma_p n I_p^+ \quad \left(right-going\right) \qquad (2.5)$$

$$-\frac{\partial I_p^-}{\partial z} + \frac{1}{c}\frac{\partial I_p^-}{\partial t} = \sigma_p n I_p^- \quad (left-going). \tag{2.6}$$

Adding these two equations produces:

$$\frac{\partial}{\partial z}\left(I_p^+ - I_p^-\right) + \frac{1}{c}\frac{\partial}{\partial t}\left(I_p^+ + I_p^-\right) = \sigma_p n\left(I_p^+ + I_p^-\right). \tag{2.7}$$

If it is assumed that there is no variation in the z-direction (the so-called rate equation approximation), then the first term in Equation (2.7) can be dropped, resulting in:

$$\frac{d}{dt}\left(I_p^+ + I_p^-\right) = c\sigma_p n\left(I_p^+ + I_p^-\right) \tag{2.8}$$

If the gain medium does not fill the resonator, then $n = 0$ outside the laser crystal. Integrating both sides of Equation (2.8) over z from $z = 0$ to $z = L_p$ (the length of the pump cavity) we obtain:

$$\int_0^{L_p}\frac{d}{dt}\left(I_p^+ + I_p^-\right)dz = \int_0^{L_p} c\sigma_p n\left(I_p^+ + I_p^-\right)dz. \tag{2.9}$$

Since the LHS of this equation is independent of z (by the rate equation approximation), we obtain the relation:

$$\frac{d}{dt}\left(I_p^+ + I_p^-\right)L_p = c\sigma_p n l_p\left(I_p^+ + I_p^-\right), \tag{2.10}$$

where l_p is the length of the gain medium. Rearranging the terms in this equation we obtain:

$$\frac{d}{dt}\left(I_p^+ + I_p^-\right) = c\sigma_p\left(\frac{l_p}{L_p}\right)n\left(I_p^+ + I_p^-\right) \tag{2.11}$$

The number of pump photons in the cavity, P, is proportional to the total irradiance so,

$$\frac{dP}{dt} = c\sigma_p \left(\frac{l_p}{L_p}\right) nP \qquad (2.12)$$

Relating the inversion density, n, to the total number of inverted atoms by $nV_g = N$, where V_g is the volume in the gain medium which interacts with the pump cavity mode, we obtain:

$$\frac{dP}{dt} = c\sigma_p \left(\frac{l_p}{L_p}\right) \frac{N}{V_g} P \qquad (2.13)$$

But $V_g = l_p A$, where A is the cross-sectional area of the mode, and $V_p = L_p A$, so Equation (2.13) can be written as:

$$\frac{dP}{dt} = \frac{c\sigma_p}{V_p} NP \qquad (2.14)$$

Including the round-trip loss terms in the cavity, Equation (2.14) becomes:

$$\frac{dP}{dt} = \frac{c\sigma_p}{V_p} NP - \gamma_{cp} P, \qquad (2.15)$$

where $\gamma_{cp} = \delta_p / t_{prt}$, δ_p is the pump cavity loss parameter, and $t_{prt} = p_p / c$ is the roundtrip cavity time. The pump cavity loss parameter[19] is given by:

$$\delta_p \equiv 2\alpha_{p0} p_p + \ln\left(\frac{1}{R_1 R_2}\right) \qquad (2.16)$$

where α_{p0} is the internal loss coefficient for the pump, p_p is the perimeter of the pump cavity, and R_1, R_2 are the reflectivities of the pump cavity mirrors.

So far, Equation (2.15) includes the effects of stimulated transitions (stimulated emission and stimulated absorption), and also cavity loss terms, but not yet spontaneous emission terms. The form of Equation (2.15) makes it simple to add the effect of spontaneous emission to the cavity. A fundamental principle of quantum mechanics states that the spontaneous emission rate from any given set of atoms into any one cavity mode is exactly equal to the stimulated emission rate that would be produced from the same atoms by *one photon* of coherent signal energy present in the same mode.[20] So the inclusion of spontaneous emission results in one "extra photon" in Equation (2.15):

$$\frac{dP}{dt} = \frac{c\sigma_p}{V_p} N(P+1) - \gamma_{cp}P \qquad (2.17)$$

The corresponding rate equation for the atoms can be written as:[21]

$$\frac{dn}{dt} = -\sigma_p n \Phi_p \qquad (2.18)$$

where Φ_p is the pump photon flux $\left(photons/cm^2 \cdot \sec\right)$. The photon flux is related to the total number of photons in the cavity by:

$$\Phi_p = \frac{cP}{V_p} \qquad (2.19)$$

and since $nV_g = N$, Equation (2.18) becomes:

$$\frac{dN}{dt} = -\sigma_p N \frac{cP}{V_p} = -\frac{c\sigma_p}{V_p} PN \qquad (2.20)$$

The inclusion of the spontaneous emission term in Equation (2.17) implies a loss of the inversion density n. So Equation (2.20) must be modified to:

$$\frac{dN}{dt} = -\frac{c\sigma_p}{V_p}(P+1)N .$$ (2.21)

A similar line of reasoning can be extended to the Stokes irradiance inside the Stokes cavity. If I_s^+ and I_s^- are the right- and left-going Stokes irradiances, then:

$$\frac{d}{dt}\left(I_s^+ + I_s^-\right) = c\sigma_s p\left(I_s^+ + I_s^-\right)$$ (2.22)

where σ_s is the stimulated Raman scattering cross-section and p is the pump photon density $p = P/V_p$. Integrating both sides over z from $z = 0$ to $z = L_s$ (the length of the Stokes cavity), and realizing that $\sigma_s = 0$ outside of the Raman crystal of length l_s, we obtain:

$$\frac{d}{dt}\left(I_s^+ + I_s^-\right) = c\sigma_s\left(\frac{l_s}{L_s}\right)p\left(I_s^+ + I_s^-\right).$$ (2.23)

As done with the pump, the number of Stokes photons in the cavity is proportional to the total intensity, so Equation (2.23) becomes:

$$\frac{dS}{dt} = c\sigma_s\left(\frac{l_s}{L_s}\right)pS .$$ (2.24)

Using the relation $p = P/V_p$ and including the loss terms for the Stokes cavity, we obtain:

$$\frac{dS}{dt} = \frac{c\sigma_s}{V_p}\left(\frac{l_s}{L_s}\right)PS - \gamma_{cs}S$$ (2.25)

For the physical case considered in Figure 2.1-1, an intracavity telescope is used to reduce the pump beam size in the Raman crystal. This requires a modification of

Equation (2.25) to account for the increased pump beam irradiance inside the crystal. As was assumed previously, the total Stokes irradiance is proportional to the total number of Stokes photons in the cavity, with the exact relationship given by:

$$S = \frac{V_s}{h\nu_s}\left(I_s^+ + I_s^-\right) \qquad (2.26)$$

Similarly, the expression for the total number of pump photons in the pump cavity is:

$$P = \frac{V_p}{h\nu_p}\left(I_p^+ + I_p^-\right). \qquad (2.27)$$

The effect of the intracavity telescope is to increase the pump beam irradiance in the crystal by a factor of A/A_{inside}, where A_{inside} is the cross-sectional area of the beam inside the Raman crystal. So the pump photon number, P, in Equation (2.25) must be boosted by a factor of A/A_{inside} to account for intracavity focusing. The resulting expression is:

$$\frac{dS}{dt} = \frac{c\sigma_s}{V_p}\left(\frac{l_s}{L_s}\right)\left(\frac{A}{A_{inside}}\right)PS - \gamma_{cs}S \qquad (2.28)$$

Raymer and Walmsley[22] show that the source term for spontaneous Raman scattering is completely analogous to the case of atomic spontaneous emission, i.e. the spontaneous Raman emission rate is just the stimulated Raman scattering rate for one Stokes photon in the cavity mode. In other words, we can replace S in the stimulated emission term of Equation (2.28) with $S+1$ to produce:

$$\frac{dS}{dt} = \frac{c\sigma_s}{V_p}\left(\frac{l_s}{L_s}\right)\left(\frac{A}{A_{inside}}\right)P(S+1) - \gamma_{cs}S \qquad (2.29)$$

Neglecting the loss terms for the moment, the total number of photons must be conserved. This is just a way of enforcing conservation of energy. Therefore, the Stokes

photon gain rate must be balanced by a corresponding decrease or loss in the pump photon rate. So the inclusion of pump conversion to Stokes light results in the following rate equation for the pump photons:

$$\frac{dP}{dt} = \frac{c\sigma_p}{V_p} N(P+1) - \frac{c\sigma_s}{V_p}\left(\frac{l_s}{L_s}\right)\left(\frac{A}{A_{inside}}\right)P(S+1) - \gamma_{cp}P \quad (2.30)$$

Treatment of the second Stokes light in the same fashion leads to:

$$\frac{d}{dt}\left(I_{ss}^+ + I_{ss}^-\right) = c\sigma_{ss}s\left(I_{ss}^+ + I_{ss}^-\right) \quad (2.31)$$

where σ_{ss} is the stimulated second Stokes Raman scattering cross-section. Integrating both sides over z from $z = 0$ to $z = L_s$ (where it is assumed that the second Stokes radiation is contained in the Stokes cavity), yields:

$$\frac{d}{dt}\left(I_{ss}^+ + I_{ss}^-\right) = c\sigma_{ss}\left(\frac{l_s}{L_s}\right)s\left(I_{ss}^+ + I_{ss}^-\right), \quad (2.32)$$

which, when converted to second Stokes photons becomes:

$$\frac{dSS}{dt} = \frac{c\sigma_{ss}}{V_s}\left(\frac{l_s}{L_s}\right)S \cdot SS. \quad (2.33)$$

Using the same arguments of balancing the rate of loss of Stokes photons, and of spontaneous second Stokes emission, leads to the complete set of coupled rate equations for the physical system (Equations (2.21) and (2.30) have been repeated here):

$$\frac{dN}{dt} = -\frac{c\sigma_p}{V_p}(P+1)N \quad (2.34)$$

$$\frac{dP}{dt} = \frac{c\sigma_p}{V_p} N(P+1) - \frac{c\sigma_s}{V_p}\left(\frac{l_s}{L_s}\right)\left(\frac{A}{A_{inside}}\right)P(S+1) - \gamma_{cp}P \quad (2.35)$$

$$\frac{dS}{dt} = \frac{c\sigma_s}{V_p}\left(\frac{l_s}{L_s}\right)\left(\frac{A}{A_{inside}}\right)P(S+1) - \frac{c\sigma_{ss}}{V_s}\left(\frac{l_s}{L_s}\right)S(SS+1) - \gamma_{cs}S \quad (2.36)$$

$$\frac{dSS}{dt} = \frac{c\sigma_{ss}}{V_s}\left(\frac{l_s}{L_s}\right)S(SS+1) - \gamma_{css}SS \quad (2.37)$$

To check the conservation of energy of this system of equations, take the sum of the rates to find:

$$\dot{N} + \dot{P} + \dot{S} + \dot{SS} = -\gamma_{cp}P - \gamma_{cs}S - \gamma_{css}SS \quad (2.38)$$

or, equivalently,

$$\dot{N} + \dot{P} + \dot{S} + \dot{SS} + \gamma_{cp}P + \gamma_{cs}S + \gamma_{css}SS = 0. \quad (2.39)$$

This is essentially a statement of the *Manley-Rowe relations*[23] for this physical process. If we integrate Equation (2.39) over time, we will find a useful relationship between the total energies of the pump, Stokes, and second Stokes pulses and the initial atomic inversion in the Nd:YAG gain medium:

$$\int_0^\infty \left\{ \dot{N} + \dot{P} + \dot{S} + \dot{SS} + \gamma_{cp}P + \gamma_{cs}S + \gamma_{css}SS \right\} dt = 0 \quad (2.40)$$

or,

$$[N(\infty) - N(0)] + [P(\infty) - P(0)] + [S(\infty) - S(0)] + [SS(\infty) - SS(0)] +$$

$$\gamma_{cp}\int_0^\infty P dt + \gamma_{cs}\int_0^\infty S dt + \gamma_{css}\int_0^\infty SS dt = 0. \quad (2.41)$$

But the initial and long-time conditions are, respectively:

$$N(0) = N_i, \quad P(0) = S(0) = SS(0) = 0 \qquad (2.42)$$

and,

$$N(\infty) = P(\infty) = S(\infty) = SS(\infty) = 0 \qquad (2.43)$$

where N_i is the initial atomic inversion. Since $\gamma_{cp} P$ is the number of pump photons per second leaking out of the system, $\left(hc/\lambda_p\right)\gamma_{cp} P$ is the power (in W) leaking from the system, and $E_p = \dfrac{hc}{\lambda_p}\gamma_p \int_0^\infty P(t)\,dt$ is the total energy that leaked out of the cavity. Thus Equation (2.41) can be written as:

$$-N_i + \frac{\lambda_p}{hc}E_p + \frac{\lambda_s}{hc}E_s + \frac{\lambda_{ss}}{hc}E_{ss} = 0, \qquad (2.44)$$

or,

$$E_p + \frac{\lambda_s}{\lambda_p}E_s + \frac{\lambda_{ss}}{\lambda_p}E_{ss} = \frac{hc}{\lambda_p}N_i \qquad (2.45)$$

2.2 Numerical Model

A detailed numerical model of the intracavity Raman laser dynamics has been constructed in a Mathematica® notebook. Before discussing some of the results of this modeling, it is necessary to derive modified versions of the coupled rate Equations (2.34) - (2.37). These equations describe the rates of change of numbers of inverted atoms and photons. The equations can be converted to atomic and photon *densities* by dividing through by the appropriate volumes. The relationships between atomic (or photon) numbers and atomic (or photon) densities are expressed by:

$$n = \frac{N}{V_g}, \quad p = \frac{P}{V_p}, \quad s = \frac{S}{V_s}, \quad ss = \frac{SS}{V_s} \tag{2.46}$$

where n, p, s, and ss are the atomic, pump photon, Stokes photon, and second Stokes photon densities, respectively. Dividing through Equations (2.34) - (2.37) by the proper volumes, as specified in Equations (2.46) results in the density rate equations:

$$\frac{dn}{dt} = -r_p \left(p + \frac{1}{V_p} \right) n \tag{2.47}$$

$$\frac{dp}{dt} = r_p n \left(p + \frac{1}{V_p} \right) - r_s \left(\frac{l_s}{L_p} \right) \left(\frac{A_s}{A_{inside}} \right) p \left(s + \frac{1}{V_s} \right) - \gamma_{cp} p \tag{2.48}$$

$$\frac{ds}{dt} = r_s \left(\frac{l_s}{L_s} \right) \left(\frac{A}{A_{inside}} \right) p \left(s + \frac{1}{V_s} \right) - r_{ss} \left(\frac{l_s}{L_s} \right) s \left(ss + \frac{1}{V_s} \right) - \gamma_{cs} s \tag{2.49}$$

$$\frac{dss}{dt} = r_{ss} \left(\frac{l_s}{L_s} \right) s \left(ss + \frac{1}{V_s} \right) - \gamma_{css} ss \tag{2.50}$$

where $r_p = c\sigma_p$, $r_s = c\sigma_s$, and $r_{ss} = c\sigma_{ss}$. The quantity A_s is the cross-sectional area of the Stokes mode volume, i.e. $A_s = V_s/L_s$. The Stokes cross-section is related to the running gain in the Raman crystal, g_s, by:

$$\sigma_s = \frac{g_s h c^2}{\lambda_p}. \tag{2.51}$$

The running gain at a pump wavelength of 1.064 μm is 11.0 cm/GW, and at the pump wavelength of 1.338 μm it is $g_s = (1.064/1.338) \cdot 11 (cm/GW) = 8.75 (cm/GW)$. The

Nd:YAG laser cross-section at 1.338 μm is $\sigma_p = 1.0 \times 10^{-19} cm^2$. The second Stokes

cross-section is given by:

$$\sigma_{ss} = \frac{\lambda_p}{\lambda_s} \sigma_s.$$ (2.52)

The set of Equations (2.47) - (2.50) is solved numerically using Mathematica's built-in

function for solving differential equations, *NDSolve*[].[24] The initial conditions are set to

be the initial inversion density, and the spontaneously emitted pump, Stokes, and second

Stokes photon densities. Table 2-1 shows a list of the pump parameters used to model

the intracavity Stokes laser used as the illuminating laser (see Stokes Laser Section).

Table 2-1 Pump Parameters

Wavelength	1.338 μm
Cavity Length	54.05 cm
Host Length	7.6 cm
Host Diameter	0.6 cm
Mode Diameter	0.6 cm
Mode Diameter in Raman	0.24 cm
HR Reflectivity	99.5%
OC Reflectivity	99.5%
Dichroic Reflectivity	95.0%
Cavity Lifetime	5.265 nsec

Table 2-2 shows the list of first Stokes parameters used in the model.

Table 2-2 First Stokes Parameters

Wavelength	1.556 μm
Cavity Length	20.2 cm
Raman Length	2.2 cm
Raman Mode Diameter	0.166 cm
HR Reflectivity	99.5%
OC Reflectivity	50.0%
Cavity Lifetime	1.31 nsec

Table 2-3 shows the second Stokes parameters used in the model.

Table 2-3 Second Stokes Parameters

Wavelength	1.859 µm
Cavity Length	20.2 cm
Raman Length	2.2 cm
Raman Mode Diameter	0.166 cm
HR Reflectivity	1.0%
OC Reflectivity	1.0%
Cavity Lifetime	0.14 nsec

Finally, shows the host pumping parameters used in the model.

Table 2-4 Host Pumping Parameters

Max. Flashlamp Energy	48.8 J
Pumping Efficiency	1.1 %
Max. Extractable Energy	59.6 mJ
Initial Inversion Ratio	2.4
Final Inversion Ratio	0.3
Maximum Intracavity Irradiance	2.8 GW/cm^2

Figure 2.2-1 shows the model output at the maximum flashlamp energy of 48.8 Joules. As shown in the figure, the total predicted Stokes pulse output is $E_s(out) = 33.6\ mJ$. The Stokes pulse shows an extremely fast rise time, and a fall time which is consistent with the 1.31 nanosecond cavity lifetime of the first Stokes cavity. Note that the model predicts *multiple pulses*. This is due to the fact that the model calculation shows the first Stokes pulse reaching threshold and depleting the pump before the pump pulse reached its peak value. As a result, some inversion is left over and another pump pulse builds up, causing a second pulse of first Stokes light. This is obviously an undesirable phenomena for an illuminating laser, since the two pulses occur with a time separation of only about

100 nanoseconds. This corresponds to a one-way distance of about 15 meters in air, meaning that lidar return pulses from objects 15 meters apart would coincide at the receiver, causing range-gating ambiguity.
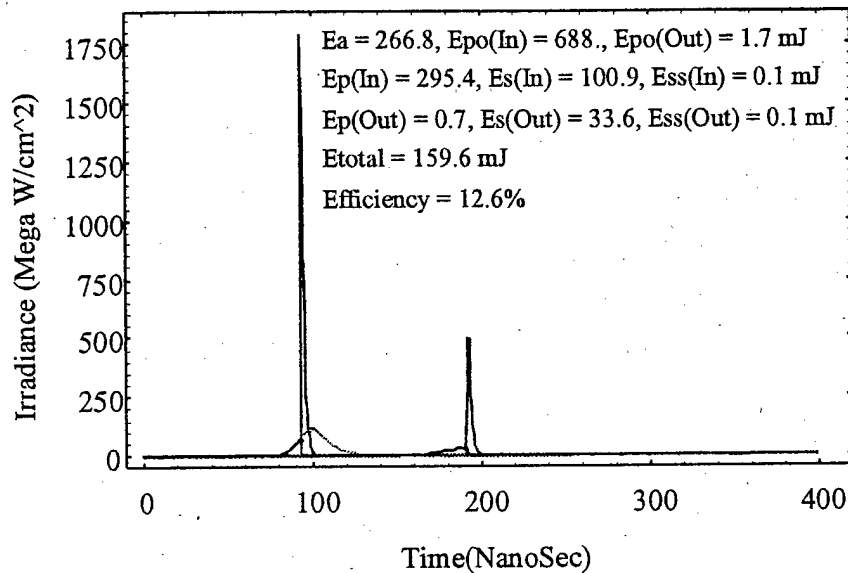
Figure 2.2-1 Model Output at 48.8 J Flashlamp Input
Gray line – Undepleted pump pulse, Blue line – Depleted pump pulse, Red line – First Stokes pulse.

Figure 2.2-2 shows the model output at a flashlamp energy of 35 Joules. This is the level at which the seed Stokes laser was operated during the subsequent imaging experiments. The figure shows that only a single first Stokes pulse is generated with an output energy of 11.1 mJ. The actual output was measured to be 12 mJ under these conditions (see Stokes Laser Section). Thus the rate equation model accurately predicts both the multiple-pulsing behavior and the output energy of the Stokes pulses.
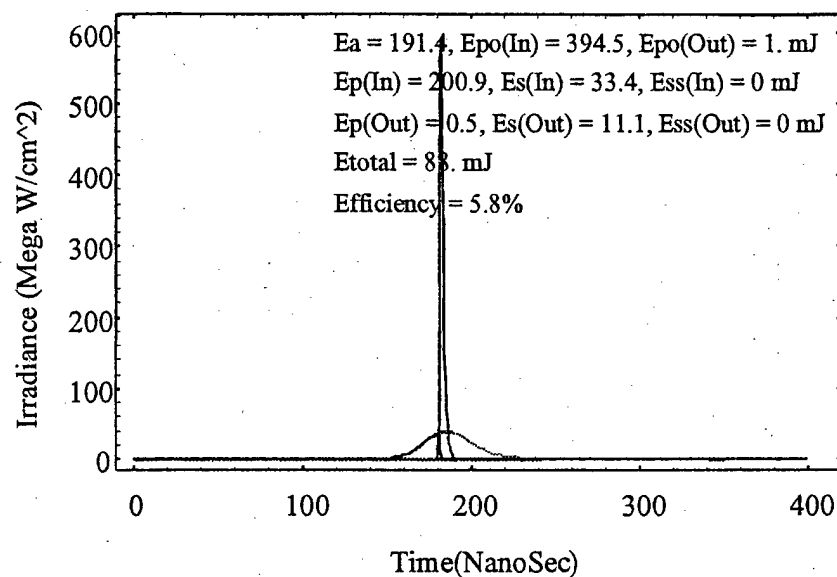
Figure 2.2-2 Model Output at 35 J Flashlamp Input
Gray line – Undepleted pump pulse, Blue line – Depleted pump pulse, Red line –
First Stokes pulse.

3 Raman Image Amplifier Theory

3.1 Semi-classical Theory of Raman Amplification

Raman scattering is a two-photon process whereby one photon at ω_P is absorbed and one photon at ω_S is emitted, while the material makes a transition from the initial energy state, E_0, to the final state, E_1, as illustrated in Figure 3.1-1. Energy conservation requires that $\hbar(\omega_P - \omega_S) = E_1 - E_0 = \hbar\omega_V$, which is just the energy difference between the final and initial states. A Raman active medium is able to couple frequencies that differ by the frequency of the molecular vibration or optical phonon in the material. This coupling interaction between the pump and Stokes beams can be analyzed classically using the wave equation for the electric field and treating the molecular vibrations as damped harmonic oscillators.[13]
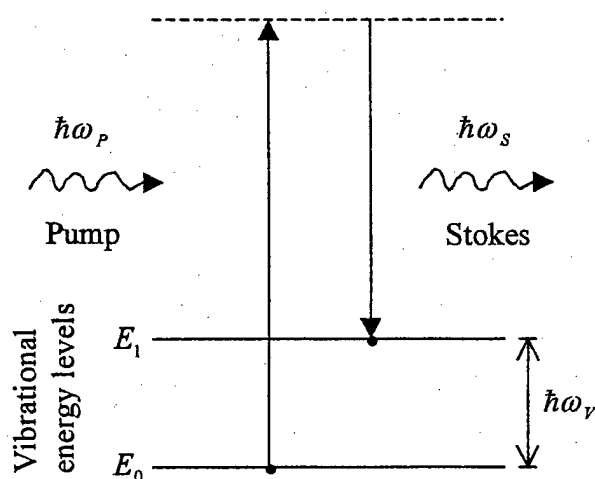
Figure 3.1-1 Raman Scattering:
Pump photon absorbed, Stokes photon emitted, and material raised to an excited level.

By the application of the slowly varying amplitude approximation, the equations coupling the pump and Stokes beam intensities are:

$$\frac{\partial I_P}{\partial z'} = -\frac{\omega_P}{\omega_S} g I_P I_S \qquad (3.1)$$

and

$$\frac{\partial I_S}{\partial z'} = g I_S I_P \qquad (3.2)$$

where g is the Raman gain coefficient. The frequency shifts and Raman gains for several

substances are shown in Table 3-1.

Table 3-1 Frequency Shift and Stimulated Raman Gain for Several Substances

Substance	Raman shift (cm^{-1})	Raman Gain (cm/GW)
Gas H_2	4155	1.5 (300 K, 10 atm)
Liquid N_2	2326.5	17
$Ba(NO_3)_2$	1047.3	18.9 (1.56 μm)

Differential equations (3.1) and (3.2) describe the depletion of the pump beam and the

amplification of the Stokes beam, respectively, as the two beams copropagate. This set

of equations can be solved by considering that the number of photons is conserved in

Raman scattering. Thus the quantity

$$I_0 = I_P(z') + \frac{\omega_P}{\omega_S} I_S(z') \qquad (3.3)$$

must remain constant. The solution to differential equations (3.1) and (3.2) is given by

equation (3.4):

$$I_S(z') = I_0 \frac{\frac{I_S(0)}{I_P(0)} \exp(g I_0 z')}{1 + \frac{\omega_P}{\omega_S} \frac{I_S(0)}{I_P(0)} \exp(g I_0 z')} \qquad (3.4)$$

where $I_S(0)$ and $I_P(0)$ are the input intensities of the Stokes and pump beams,

respectively. Figure 3.1-2 shows the behavior of the output Stokes intensity as a function

of input Stokes intensity for a fixed pump intensity and crystal length. For input Stokes

intensities that approach the pump intensity, the amplifier output Stokes intensity saturates.
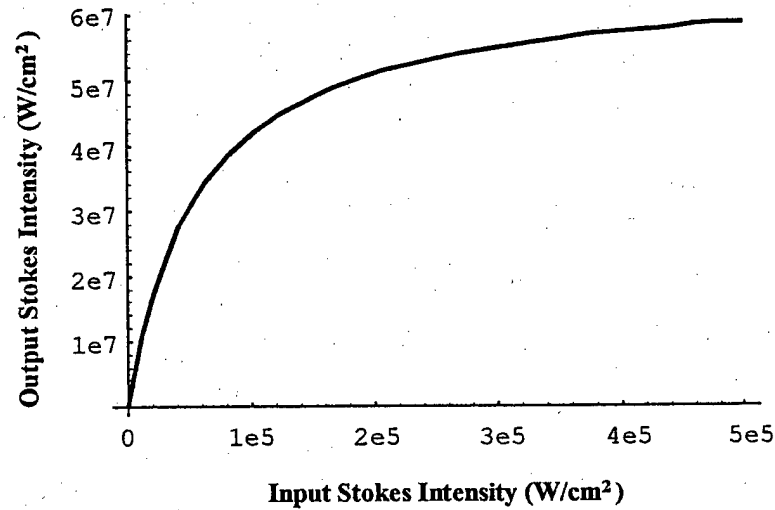
Figure 3.1-2 SSRIA Output vs. Input Intensity showing saturation behavior

For Stokes beam intensities that are small compared to the pump beam intensity, which is the usual case for the SSRIA, equation (3.4) simplifies to:

$$I_S(z') = I_S(0)\exp(gI_P z')$$
(3.5)

For a SSRIA crystal of length, L_R, the output Stokes intensity is thus:

$$I_S(L_R) = I_S(0)\exp(gI_P L_R)$$
(3.6)

The SSRIA can thus be characterized by a linear input-output relationship,

$$I_S^{out} = GI_S^{in}$$
(3.7)

where the overall amplifier gain, G, is given by:

$$G = Exp(gI_P L_R) = Exp(G_R).$$
(3.8)

Figure 3.1-3 shows the gain region investigated in this study. Typical amplified images were made at a gain level of around 900. The gain exponent, G_R, is proportional to the pump intensity in the SSRIA crystal. By varying the pump energy, along with changing the focusing lens at the output of the pump laser, the pump intensity in the SSRIA crystal was adjusted over the total range shown in the figure. Note the region hatched in blue in the figure. This represents a gain region which is not accessible to image amplification, because experiments showed that beyond a gain of 10^6 the amplifier begins to produce single-pass stimulated Raman scattering with no signal input to the crystal.
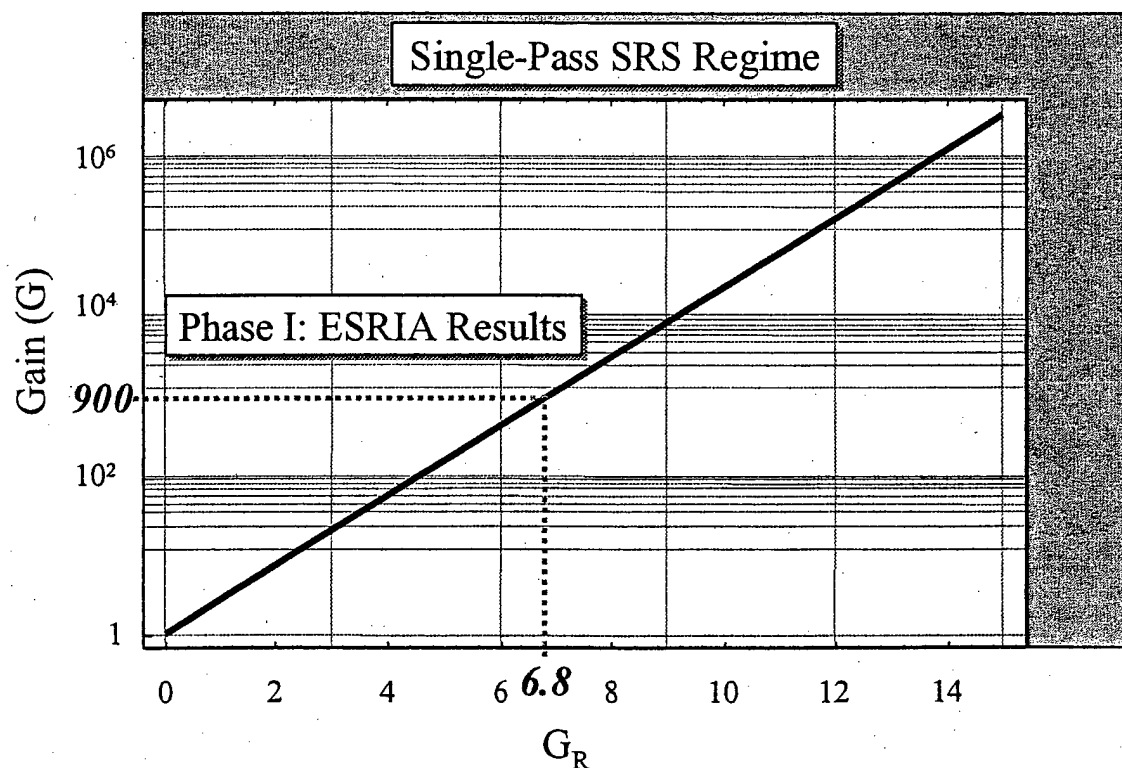
Figure 3.1-3   Available Gain Region of SSRIA

3.2 Minimum Amplifier Noise

One could consider that an "ideal" optical amplifier would be one that amplifies an input signal with the addition of no extra noise. However, it has been proven that it is impossible to build such an "ideal" amplifier.[25] In fact, such a noise-free amplifier would violate Heisenberg's uncertainty principle, and is therefore forbidden. To show that this is true, consider the usual statement of the uncertainty principle regarding the simultaneous measurement of a particle's momentum, p, and position, x. The uncertainties, Δp and Δx, associated with this measurement are related by

$$\Delta p \Delta x \geq \frac{\hbar}{2} \qquad (3.9)$$

where $\hbar$ is Planck's constant divided by 2π. If we now consider photons propagating along the x-axis, the momentum of the photons (and the associated uncertainty, Δp) are given by

$$p = \hbar k = \hbar \frac{\omega}{c} = \frac{E}{c}; \Delta p = \frac{\Delta E}{c} \qquad (3.10)$$

where k is the wave vector of the electromagnetic field associated with the photons, E is the photon energy and c is the speed of light. The photon arrival time at a particular location (and the associated uncertainty, Δt) are given by

$$t = \frac{x}{c}; \Delta t = \frac{\Delta x}{c} \qquad (3.11)$$

Substituting the uncertainties given in Equations (3.10) and (3.11) into the uncertainty relation of Equation (3.9) yields the related uncertainty relation between energy and time:

$$\Delta E \Delta t \geq \frac{\hbar}{2} \qquad (3.12)$$

If the uncertainty in the energy is due to an uncertainty in the number of photons while the photons' frequency is fixed, then the energy uncertainty is $\Delta E = h\nu\Delta n$. The phase uncertainty of the optical wave is related to the time uncertainty by $\Delta\varphi = 2\pi\nu\Delta t$. Substitution of these last two expressions into Equation (3.12) yields the uncertainty relation between photon number and phase:

$$\Delta n \Delta \varphi \geq \frac{1}{2} \qquad (3.13)$$

Assume now that we have an ideal linear optical amplifier that is completely noiseless. Assume that the photon number of the input stream of photons is $n_0 \pm \Delta n_0$. Then the output of the ideal amplifier is

$$n \pm \Delta n = G n_0 \pm G \Delta n_0 \qquad (3.14)$$

meaning that the input signal is linearly amplifier with gain G, and no additional noise has been added. Assuming that the phase of the input signal is $\varphi_0 \pm \Delta\varphi_0$, the output phase is given by

$$\varphi \pm \Delta\varphi = \varphi_0 + \theta \pm \Delta\varphi_0 \qquad (3.15)$$

where θ is just a phase shift accounting for the propagation through the amplifier and any other physical effect. In other words, this assumes that the amplifier is "phase preserving". So the net effect of the amplifier is to increase the output photon number uncertainty by a factor of G, while leaving the output phase uncertainty unchanged.

Now let us assume that we have an ideal optical detector that is sensitive to both photon number and phase and has unity quantum efficiency. The first condition implies that the detector has the smallest possible uncertainty, i.e.

$$\Delta n \Delta \varphi = 1/2 \qquad (3.16)$$

while the second condition implies that every photon that strikes the detector produces one photocount.[26] Assuming that our ideal optical amplifier is placed in front of this ideal detector to produce a composite, pre-amplified photon detector, we can consider this system to be a new input/output device. Looking at the input/output relationship of this composite device, we see that the output signal has the minimum possible uncertainty (i.e. Equation (3.16)). To find the corresponding uncertainty in the input signal, we must substitute Equations (3.14) and (3.15) into Equation (3.16) to arrive at

$$\Delta n_0 \Delta \varphi_0 = \frac{1}{2G} \qquad (3.17)$$

This implies that for arbitrarily large gains G, the uncertainty product of the input photon stream can be made arbitrarily small. This directly contradicts Heisenberg's uncertainty principle, Equation (3.13), and so we have reached a logical contradiction in our argument. Tracing back the steps in the argument, we see that the assumption of a completely noise-free optical amplifier must be in error. Therefore, such a noise-free optical amplifier *physically cannot exist* – some *noise must be added* in the amplification process to satisfy the uncertainty principle.

This conclusion is valid for all *phase-insensitive* linear optical amplifiers, i.e. linear amplifiers for which a phase shift of the input produces the same or opposite phase shift

of the output. If the phase shift of the output is the same, then the amplifier is called *phase-preserving*; if the phase shift of the output is opposite, then the amplifier is called *phase-conjugating*.[27] Examples of phase-preserving amplifiers are standard laser amplifiers and Raman amplifiers. *Phase-sensitive* linear optical amplifiers do not preserve the phase of the input signal and have gains which depend on the input phase. An example of a phase-sensitive optical amplifier is the optical parametric amplifier (OPA). OPA's have both a *signal* channel and an *idler* channel. An OPA that has both input channels excited is sensitive to the phase of the input signal. This phase-sensitive amplifier amplifies both the signal and the noise in the quadrature that carries the signal, but deamplifies the noise in the conjugate quadrature that carries no information.[28] In this case, it is possible to achieve "noiseless" optical amplification by the concept of "squeezing".[28] However, this can only be accomplished by giving up the preservation of the optical phase and thus makes this method of amplification unsuitable for optical images.

Given that the uncertainty principle must always be satisfied, it is possible to derive the minimum amount of linear amplifier noise consistent with it. This will establish a lower bound on amplifier noise. Assume that we have a linear, phase-insensitive amplifier which adds noise to the signal, followed by an ideal detector. The uncertainties in photon number and phase associated with the amplifier are Δn_a^2 and $\Delta \varphi_a^2$, respectively. Likewise, the uncertainties associated with the detector are Δn_d^2 and $\Delta \varphi_d^2$. The amplifier noise and the detector noise are assumed to be uncorrelated, so the total uncertainty of the output signal is given by

$$\Delta n^2 = \Delta n_a^2 + \Delta n_d^2$$
$$\Delta \varphi^2 = \Delta \varphi_a^2 + \Delta \varphi_d^2 \qquad (3.18)$$

The uncertainty obtained at the detector is related to the input uncertainty (before the amplifier) by

$$\Delta n^2 = G^2 \Delta n_0^2$$
$$\Delta \varphi^2 = \Delta \varphi_0^2 \qquad (3.19)$$

Substituting Equation (3.19) into Equation (3.18) and taking the product of the uncertainties we obtain

$$\Delta n_0^2 \Delta \varphi_0^2 = \frac{1}{G^2} \left\{ \Delta n_a^2 \Delta \varphi_a^2 + \Delta n_d^2 \Delta \varphi_d^2 + \Delta \varphi_a^2 \Delta \varphi_d^2 \left(\frac{\Delta n_a^2}{\Delta \varphi_a^2} + \frac{\Delta n_d^2}{\Delta \varphi_d^2} \right) \right\} \qquad (3.20)$$

By imposing the assumption that the detector has minimum uncertainty, we can substitute Equation (3.16) into Equation (3.20) to obtain

$$\Delta n_0^2 \Delta \varphi_0^2 = \frac{1}{G^2} \left\{ \Delta n_a^2 \Delta \varphi_a^2 + \frac{1}{4} + \frac{\Delta \varphi_a^2}{2} \frac{\Delta \varphi_d}{\Delta n_d} \left(\frac{\Delta n_a^2}{\Delta \varphi_a^2} + \frac{\Delta n_d^2}{\Delta \varphi_d^2} \right) \right\} \qquad (3.21)$$

To proceed we must make the further requirement that the detector uncertainty *ratio*, $\Delta n_d^2 / \Delta \varphi_d^2$, is chosen to minimize the output number-phase uncertainty. This is done by minimizing Equation (3.21) with respect to $\Delta n_d^2 / \Delta \varphi_d^2$ and leads to the relation:

$$\frac{\Delta n_a}{\Delta \varphi_a} = \frac{\Delta n_d}{\Delta \varphi_d} \qquad (3.22)$$

In other words, minimizing the output number-phase uncertainty with respect to the detector uncertainty ratio means that the amplifier and the detector need to be matched in terms of the ratio of their introduced uncertainties.[25] Imposing the condition that the number-phase uncertainty product inferred for the input signal is at the minimum

allowed, i.e. $\Delta n_0 \Delta \varphi_0 = 1/2$, and substituting Equation (3.22) into Equation (3.21), we obtain:

$$\Delta n_a^2 \Delta \varphi_a^2 + \Delta n_a \Delta \varphi_a - \frac{G^2 - 1}{4} = 0 \qquad (3.23)$$

with the unique solution:

$$\Delta n_a \Delta \varphi_a = \frac{G-1}{2} \qquad (3.24)$$

To proceed further, we need to make the assumption that the uncertainty associated with the amplifier is an additive white noise process with Gaussian statistics. If we also assume that the signal-to-noise ratio (SNR) is large, then the output signal statistics are closely Gaussian.[29] Based on these assumptions, the phase variance is $\Delta \varphi_a^2 = P_N / 2 P_S$, where P_S and P_N are the mean powers of the signal and the noise, respectively. The noise power variance is given by $\Delta P_N^2 = 2 P_S P_N$. The noise power variance is related to the photon number variance by $\Delta P_N^2 = (h v / T)^2 \Delta n_a^2$, where T is the detector sampling interval. Substituting these relations into Equation (3.24) we obtain

$$P_N = \frac{h v}{2} \frac{1}{T} (G - 1) = h v B (G - 1), \qquad (3.25)$$

where the relation on the right assumes that the sampling interval is $T = 1/2B$ ($2B = B_0 =$ amplifier FWHM bandwidth). This result can be interpreted in the following way: assuming that amplifier noise is an additive white noise process and that the SNR and gain G are large, the minimum possible amplifier output noise power corresponds to the energy of half a photon $(h v / 2)$ in a given observation time T. This interpretation was

also reached by H. A. Haus and J. A. Mullen[30] through an approach which considered the amplifier noise in the two light field quadratures without any assumptions on their statistics. The amplifier output noise given by Equation (3.25) ensures that the uncertainty relation $\Delta n \Delta \varphi = 1/2$ is satisfied for both the amplifier input signal and the amplifier output signal.

The energy $h\nu/2$ can be interpreted as being the zero-point energy of the quantized electromagnetic field, which is given by $E_n = \left(n + \dfrac{1}{2}\right)h\nu$.[31] The minimum detectable noise power, given by $h\nu B_0/2$, is often called *quantum noise* due to its fundamental quantum origin. The quantum noise can be contrasted with thermal noise, which has a power of $h\nu B_0 / \left[\exp\left(h\nu/k_B T\right) - 1\right]$, where k_B is Boltzmann's constant and T is the temperature. At room temperature, thermal and quantum noise are equal at a wavelength near 44 μm. At the 1.556 μm wavelength of interest, the quantum noise is 13 orders of magnitude larger than the thermal noise.

3.3 Quantum Theory of Noise

The quantum theory of noise in optical amplifiers is a sub-field of quantum optics. General information on the field of quantum optics can be found in Heitler[32]; Loudon[31]; Scully and Zubairy[33]; Sargent, Scully, and Lamb[34]; and Meystre and Sargent[35]. The interaction of a quantized electromagnetic field with two-level atoms can be described through the electric dipole interaction Hamiltonian:

$$\hat{\mathcal{H}}_{ed} = e\hat{D} \cdot \hat{E} \qquad (3.26)$$

where $\hat{D}$ and $\hat{E}$ represent the atomic electric dipole and electric field operators, respectively, and e is the electric charge. The quantized electric field is expressed in terms of the photon creation and annihilation operators $a^\dagger$, a through:

$$\hat{E} = C\hat{\varepsilon}\left\{ae^{-i(\omega t - kz)} - a^\dagger e^{i(\omega t - kz)}\right\}$$ (3.27)

where C is a constant and $\hat{\varepsilon}$ is a unit vector indicating the field polarization.

If the atomic quantum states are represented by the kets $|1\rangle$ and $|2\rangle$, corresponding to the ground and excited states, with their associated energies, 0 and $\hbar\omega$, then the atomic electric dipole operator can be expressed in the form:

$$\hat{D} = d\hat{\varepsilon}'\left\{|1\rangle\langle 2| + |2\rangle\langle 1|\right\}$$ (3.28)

where d is a constant and $\hat{\varepsilon}'$ is a unit vector corresponding to the dipole orientation. The symbols $|1\rangle\langle 2|$ and $|2\rangle\langle 1|$ represent atomic lowering and raising operators, respectively. Using Equations (3.26), (3.27), and (3.28), the interaction Hamiltonian can be written as:

$$\hat{\mathcal{H}}_{ed} = edC\hat{\varepsilon}\cdot\hat{\varepsilon}'\Big\{ae^{-i(\omega t - kz)}|2\rangle\langle 1| - a^\dagger e^{i(\omega t - kz)}|1\rangle\langle 2|$$ (3.29)
$$+ ae^{-i(\omega t - kz)}|1\rangle\langle 2| - a^\dagger e^{i(\omega t - kz)}|2\rangle\langle 1|\Big\}.$$

The interactions represented by each of the four terms in Equation (3.29) correspond to absorption of a photon (terms proportional to a) or emission of a photon (terms proportional to $a^\dagger$), with the associated changes in the atomic states.

The electric field can be represented by a statistical mixture of photon number states, $|n\rangle$. The photon number states correspond to the harmonic oscillator's energy eigenstates and are governed by the creation and annihilation relations:

$$a^\dagger|n\rangle = \sqrt{n+1}|n+1\rangle$$
$$a|n\rangle = \sqrt{n}|n-1\rangle . \qquad (3.30)$$

A pure photon number state has an exactly defined number of photons but the phase is then, necessarily, indefinite (see Equation (3.13)). Conventional laser sources do not produce pure photon number states; electromagnetic waves produced by these sources do not have a definite number of photons. A better quantum state representation for lasers are the coherent states, defined as a statistical superposition of photon number states:

$$|S\rangle = \sum u_n |n\rangle. \qquad (3.31)$$

With this representation, the probability of finding exactly n photons is given by

$$P_n = \langle n|S\rangle = |u_n|^2. \qquad (3.32)$$

The coherent states have a probability distribution P_n which corresponds to Poisson statistics.

In the following simplified derivation, we shall consider pure photon number states instead of a statistical superposition. First, define the atom-photon number states $|i,n\rangle(i=1,2)$ representing the whole atom/field system. These states verify Equations (3.30) and are orthogonal. If we assume that the initial state is $|i,n\rangle$, the probability of finding the system in the final state $|j,m\rangle$ after the interaction is:

$$P_{jm;in} = \left| \left\langle j,m \left| \hat{\mathcal{H}}_{ed} \right| i,n \right\rangle \right|^2 \tag{3.33}$$

With an initial state containing k photons, the process of photon absorption is then given by the probability $P_{2,k-1;1,k}$ and the process of photon emission is given by $P_{1,k+1;2,k}$.

Figure 3.3-1 shows an energy diagram for the field with four different possible transitions associated with the absorption or the emission of one photon in a single radiation mode of the field. Using the definition for the interaction Hamiltonian, Equation (3.29), along with the relations in (3.30) and the orthogonality properties of the atom-photon number states, the probabilities associated with the events shown in Figure 3.3-1 are:

$$\begin{aligned}
P_{2,n;1,n+1} &= (n+1)P_{n+1} \\
P_{2,n-1;1,n} &= nP_n \\
P_{1,n;2,n-1} &= nP_{n-1} \\
P_{1,n+1;2,n} &= (n+1)P_n
\end{aligned} \tag{3.34}$$

where the constants in Equations (3.28) and (3.29) were ignored, and the atomic dipole is assumed to be colinear with the field. The probabilities that are proportional to the initial photon number in the system, n, represent the processes of absorption and stimulated emission. The +1 term in the last relation of Equation (3.34) represents spontaneous emission because when there are no photons present, $n=0$; but there is still a finite probability of spontaneously emitting a photon, i.e. $P_{1,1;2,0} = P_0$.
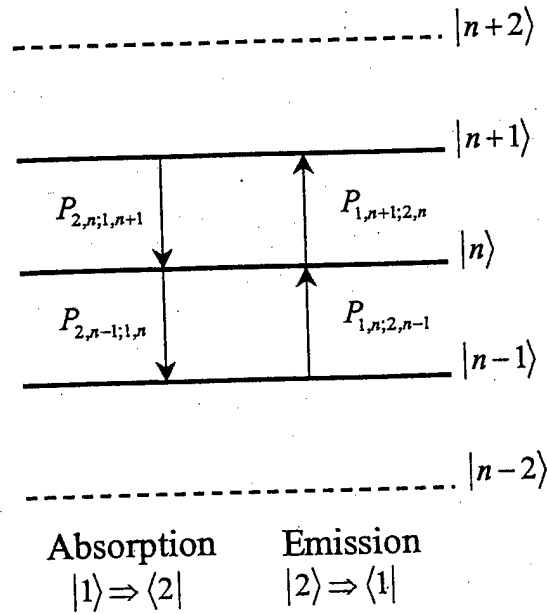
Figure 3.3-1 Energy level diagram for the photon number states $|n\rangle$ The arrows indicate the four possible transitions, with the corresponding probabilities, in which one photon is absorbed or emitted.

Now consider a collection of atoms in their ground and excited states with density at coordinate z of $N_1(z)$ and $N_2(z)$, respectively, in an infinitesimal slice of medium, dz. The cross sections for absorption and emission processes are represented by σ_a and σ_e, respectively. The change of the photon number probability dP_n between z and z+dz is given by:

$$dP_n = \left\{ \sigma_a N_1 \left(P_{2,n;1,n+1} - P_{2,n-1;1,n} \right) + \sigma_e N_2 \left(P_{1,n;2,n-1} - P_{1,n+1;2,n} \right) \right\} dz. \quad (3.35)$$

Substituting in the expressions given by Equation (3.34) and letting $a = \sigma_e N_2$ and $b = \sigma_a N_1$ we obtain:

$$\frac{dP_n}{dz} = a\left\{ nP_{n-1} - (n+1)P_n \right\} + b\left\{ (n+1)P_{n+1} - nP_n \right\} \quad (3.36)$$

which is known as the *photon statistics master equation*, and is the starting point of the famous 1957 paper by K. Shimoda, H. Takahasi, and C. H. Townes (STT)[36]. This equation is also known as the *forward Kolmogorov equation*, which governs a Markov process, defined as the random time evolution of a set $\{P_n\}$ of n variables. A Markov process described by forward or backward Kolmogorov equations is also called a birth-death-immigration (BDI) process.

The photon statistics master equation can be used to evaluate the average noise power of an optical amplifier. The rate of change of the average photon number $\langle n \rangle$ is given by the statistical mean of Equation (3.36):

$$\sum_n n \frac{dP_n}{dz} = \frac{d\langle n \rangle}{dz} = \sum_n \left[a\{n^2 P_{n-1} - n(n+1)P_n\} + b\{n(n+1)P_{n+1} - n^2 P_n\} \right] \quad (3.37)$$

Following STT, we assume that the photon number is large enough and use the substitutions $nP_{n-1} \approx (n+1)P_n$ and $nP_{n+1} \approx (n-1)P_n$, together with the normalization condition $\sum_n P_n = 1$, to find:

$$\frac{d\langle n \rangle}{dz} = a(\langle n \rangle + 1) - b\langle n \rangle. \quad (3.38)$$

The solution of Equation (3.38) is then

$$\langle n(z) \rangle = G(z)\langle n(0) \rangle + N(z) \quad (3.39)$$

where $G(z)$ is the amplifier gain, given by:

$$G(z) = \exp\left\{ \int_0^z \left[a(z') - b(z') \right] dz' \right\}, \quad (3.40)$$

and $N(z)$ is the amplified noise, given by:

$$N(z) = G(z) \int_0^z \frac{a(z')}{G(z')} dz' .$$ (3.41)

The noise represented by $N(z)$ comes from the factor $+1$ in Equation (3.38) and in the photon statistics master equation. Since this factor was previously shown to be attributed to spontaneous emission, the noise contribution is interpreted as being *amplified spontaneous emission* or ASE.

If we assume that the coefficients a and b are constant over the amplifier's length (i.e. a uniformly pumped amplifier medium) and define $\eta = \sigma_e / \sigma_a$ and $G = G(z) = \exp[(a-b)z]$, then Equation (3.41) becomes:

$$N(z) = \frac{a}{a-b}(G-1) = \frac{\eta N_2}{\eta N_2 - N_1}(G-1) .$$ (3.42)

The mean output noise power in bandwidth B can then be given as:

$$P_N = h\nu \times N(z)B = n_{sp} h\nu B(G-1)$$ (3.43)

where we have used the amplifier *spontaneous emission factor*, n_{sp}, defined by:

$$n_{sp} = \frac{\eta N_2}{\eta N_2 - N_1} .$$ (3.44)

At full medium inversion with all of the atoms in the excited state, $N_1 = 0$, and the spontaneous emission factor reaches its minimum value of one. In this case the mean output noise power becomes $P_N = h\nu B(G-1)$, which is identical to Equation (3.25)

found for the minimum noise allowed by quantum mechanics. In other words, *the minimum amplifier noise output is obtained when complete population inversion is achieved in the amplifying medium.*

In the more general case where the coefficients a and b depend on the coordinate z, the spontaneous emission factor can be defined by:

$$n_{sp}(z) = \frac{N(z)}{G(z)-1} = \frac{G(z)}{G(z)-1} \int_0^z \frac{a(z')}{G(z')} dz' . \qquad (3.45)$$

With this general definition, the mean output noise power is still given by Equation(3.43).

3.4 Photon Statistics in the Linear Gain Regime

The photon statistics master equation has been solved exactly through the use of a probability generating function (PGF)[36,37,38]. The PGF is defined as:

$$F(x,z) = \sum_n x^n P_n(z) \qquad (3.46)$$

and the probability distribution $P_n(z)$ can be calculated from it by the relation:

$$P_n(z) = \frac{1}{n!} \left(\frac{\partial^n F(x,z)}{\partial x^n} \right)_{x=0} \qquad (3.47)$$

The differential equation for the amplifier PGF is found from Equation (3.36) through the expression:

$$\frac{\partial F(x,z)}{\partial z} = \sum_n x^n \frac{dP_n(z)}{dz} = \sum_n \left[a\{nx^n P_{n-1} - (n+1)x^n P_n\} + b\{(n+1)x^n P_{n+1} - nx^n P_n\} \right]$$

$$= \sum_m \left[a\{(m+1)x^{m+1} P_m - (m+1)x^m P_m\} + b\{mx^{m-1} P_m - mx^m P_m\} \right] \quad (3.48)$$

where the summations $m = n+1$ and $m = n-1$ were used to obtain a right hand side that is a function of P_m only. If we use the relation $\sum_m mx^m P_m = x\,\partial F/\partial x$, Equation (3.48) becomes:

$$\frac{\partial F}{\partial z} = (x-1)\left\{(ax-b)\frac{\partial F}{\partial x} + aF\right\} \qquad (3.49)$$

P. Diament and M. Teich[37] have solved this last equation in a form which is particularly attractive for calculating the moments of the output photon statistics. The output PGF is shown to be:

$$F(x,z) = F[X(x,z;0),0]F_1(x,z) \qquad (3.50)$$

where

$$F_1(x,z) = \frac{1}{1-(x-1)N(z)} \qquad (3.51)$$

and

$$X(x,z;0) = 1 + \frac{(x-1)G(z)}{1-(x-1)N(z)} = 1 + \frac{(x-1)G(z)}{1-(x-1)n_{sp}(z)[G(z)-1]}. \qquad (3.52)$$

The term $F[X(x,z;0),0]$ found in Equation (3.50) can be written as:

$$F[X(x,z;0),0] = \sum_m \left[1 + \frac{(x-1)G(z)}{1-(x-1)N(z)}\right]^m P_m(0) \qquad (3.53)$$

The first and second moments, respectively, of the output photon statistics are found by:

$$\langle n(z)\rangle = \left(\frac{\partial F(x,z)}{\partial x}\right)_{x=1} \qquad (3.54)$$

$$\left\langle n^2(z) \right\rangle = \left(\frac{\partial^2 F(x,z)}{\partial x^2} \right)_{x=1} + \left\langle n(z) \right\rangle. \qquad (3.55)$$

The computation of these moments can be found in Reference 26, Appendix G. The moments are:

$$\boxed{\left\langle n(z) \right\rangle = G(z)\left\langle n(0) \right\rangle + N(z)} \qquad (3.56)$$

and

$$\left\langle n^2(z) \right\rangle = G^2(z)\left[\left\langle n^2(0) \right\rangle - \left\langle n(0) \right\rangle \right] + 4G(z)N(z)\left\langle n(0) \right\rangle + G(z)\left\langle n(0) \right\rangle + 2N^2(z) + N(z)$$
$$(3.57)$$

The output photon variance is found by using the relation $\sigma^2(z) = \left\langle n^2(z) \right\rangle - \left\langle n(z) \right\rangle^2$ and leads to the important result:

$$\boxed{\sigma^2(z) = G^2(z)\left[\sigma^2(0) - \left\langle n(0) \right\rangle \right] + G(z)\left\langle n(0) \right\rangle + N(z) + 2G(z)N(z)\left\langle n(0) \right\rangle + N^2(z)}$$
$$(3.58)$$

where $\sigma^2(0) = \left\langle n^2(0) \right\rangle - \left\langle n(0) \right\rangle^2$ is the input photon statistics variance.

The different terms that contribute to the output variance of Equation (3.58) are typically called *excess noise*, *shot noises*, and *beat noises*, respectively[39]. The first term, excess noise, is proportional to $\sigma^2(0) - \left\langle n(0) \right\rangle$ and is the only term that depends on the statistics of the input light. If the input signal follows Poisson statistics, then $\sigma^2(0) = \left\langle n(0) \right\rangle$ and so the excess noise is zero.[40] If, on the other hand, the input signal follows the statistics of chaotic or thermal light, the appropriate probability distribution is given by Bose-Einstein statistics[41] with variance of $\sigma^2(0) = \left\langle n(0) \right\rangle^2 + \left\langle n(0) \right\rangle$. Thus,

thermal light exhibits excess noise proportional to $\langle n(0) \rangle^2$ that represents the classical fluctuations of the integrated intensity. A quantity that is commonly used to characterize the amount of excess noise is the Fano factor, defined by:

$$f(z) = \frac{\sigma^2(z)}{\langle n(z) \rangle}. \qquad (3.59)$$

For Poisson statistics, the Fano factor is $f = 1$, while for Bose-Einstein statistics, $f = \langle n \rangle + 1$.

The second noise contribution, called the shot noise, is equal to the amplifier mean output power $G\langle n(0) \rangle + N$. The term shot noise comes from the effect of this noise in photodetection. The shot effect causes photocurrent noise with mean-square fluctuations $\langle i^2 \rangle = 2eB_e \langle i \rangle$ where B_e is the electronic bandwidth. Since in an ideal detector, $\langle i \rangle = \langle n \rangle B_o$, where B_o is the optical bandwidth, the shot noise is proportional to the mean number of detected photons. Actually, the use of the term shot noise is conventional here, since the present analysis does not include photodetection.

The last two terms in Equation (3.58), $2G(z)N(z)\langle n(0) \rangle + N^2(z)$, are called beat noises. The first term, $2G\langle n(0) \rangle N$, can be interpreted as the beat power between the electric field components of the amplified signal and the ASE falling on a square-law optical detector (i.e. a detector which measures only the intensity of the light). However, this interpretation is unsatisfactory from a quantum perspective, as it once again relies on an appeal to photodetection. Moreover, E. Desurvire[26] shows that even in the absence of

spontaneous emission, a noise term taking the form $2G\langle n(0)\rangle N$ appears at the output of an optical amplifier. Thus, this term cannot be interpreted as a beat component, but is instead a result of the statistical nature of the stimulated emission process. Similarly, the last term in Equation (3.58), $N^2(z)$, is a result of the statistical nature of the amplified spontaneous emission process.

The analysis above assumed that photons could only enter a single mode of the radiation field. For the analysis of a Raman image amplifier, this formalism must be extended to multiple propagation modes. For this purpose, let $\mathfrak{m}$ be the number of possible propagation modes, and let n be the total photon population distributed among these modes. If it is assumed that spontaneous emission events are equally likely for all modes, the transition probabilities in Equation (3.59) must be modified to:

$$P_{1,n;2,n-1} = (n-1+\mathfrak{m})P_{n-1}$$
$$P_{1,n+1;2,n} = (n+\mathfrak{m})P_n$$

(3.60)

The photon statistics master equation is then modified to[26]:

$$\frac{dP_n}{dz} = a\{(n-1+\mathfrak{m})P_{n-1} - (n+\mathfrak{m})P_n\} + b\{(n+1)P_{n+1} - nP_n\}$$ (3.61)

and the output mean and variance become:

$$\boxed{\langle n(z)\rangle = G(z)\langle n(0)\rangle + \mathfrak{m}N(z)}$$

(3.62)

$$\boxed{\sigma^2(z) = G^2(z)\left[\sigma^2(0) - \langle n(0)\rangle\right] + G(z)\langle n(0)\rangle + \mathfrak{m}N(z) + 2G(z)\langle n(0)\rangle N(z) + \mathfrak{m}N^2(z)}$$

(3.63)

P. Diament and M. C. Teich[37] have examined the output photon statistics probability distributions of optical amplifiers with various input signal statistics. A relevant case for

the study of Raman image amplifiers is an input signal with Poisson statistics. The input

signal probability distribution is then given by[40]:

$$P_n(0) = \frac{e^{-\langle n_0 \rangle} \langle n_0 \rangle^n}{n!}.$$ (3.64)

The output distribution is found to be described by the noncentral negative binomial

(NNB) distribution, also called the Laguerre distribution:

$$P_n(z) = \frac{N^n}{(N+1)^{n+m}} \exp\left\{-\frac{G\langle n_0 \rangle}{N+1}\right\} L_n^{(m-1)}\left\{-\frac{G\langle n_0 \rangle}{N(N+1)}\right\}$$ (3.65)

where $L_n^{(\alpha)}(U)$ is the generalized Laguerre polynomial defined by[42]:

$$L_n^{(\alpha)}(U) = \sum_{j=0}^{n} \frac{(n+\alpha)!}{j!(n-j)!(j+\alpha)!}(-U)^j$$ (3.66)

This result leads to the conclusion that *light amplification does not conserve the Poisson*

statistics for the signal. In fact, the probability distribution of Equation (3.65) actually

describes the statistics of a system where coherent and chaotic (thermal) light fields are

superimposed.[43,44]

3.5 Optical Signal-to-Noise Ratio and Noise Factor

SSRIA is a technique of gated optical preamplification. There are three main reasons

for preamplifying optical signals: 1.) to boost weak optical signals so that they are above

the level of thermal noise present in the optical detector and its associated electronics, 2.)

to compensate for low quantum efficiency of the optical detector, and 3.) to provide

optical gating. A requirement of preamplification is that it adds minimum noise to the

incident signal. The noise performance of optical amplifiers can be characterized by the power *noise factor*, F, defined by:

$$F = \frac{SNR_{input}^2}{SNR_{output}^2} \qquad (3.67)$$

where SNR_{input}^2 is the square of the signal-to-noise ratio input to the amplifier and SNR_{output}^2 is the square of the output signal-to-noise ratio from the amplifier. Here we are using the convention that the optical signal-to-noise ratio is given by:

$$SNR = \frac{\langle n \rangle}{\sigma} \qquad (3.68)$$

where $\langle n \rangle$ is the mean optical signal in photon number and σ is the root mean square (rms) noise level, defined to be the square root of the photon number variance.[45] For input signals with Poisson statistics, the mean signal level is $\langle n(0) \rangle$, while the rms noise level is $\langle n(0) \rangle^{1/2}$. This leads to an input SNR of:

$$SNR = \frac{\langle n(0) \rangle}{\sqrt{\langle n(0) \rangle}} = \sqrt{\langle n(0) \rangle} \qquad (3.69)$$

or,

$$SNR_{Poisson}^2 = \langle n(0) \rangle. \qquad (3.70)$$

At the output of the Raman amplifier, the square of the SNR can be expressed as:

$$SNR_{output}^2 = \frac{\left\langle \langle n(L) \rangle - \langle n(L) \rangle_{ASE} \right\rangle_T^2}{\sigma^2(L)} = \frac{G^2(L)\langle n(0) \rangle^2}{\sigma^2(L)} \qquad (3.71)$$

where L is the length of the Raman amplifier crystal, $\langle n(L) \rangle - \langle n(L) \rangle_{ASE}$ represents the mean photon number that contains signal information, and $\langle n(L) \rangle_{ASE} = \mathfrak{m}N(z)$ is the background ASE. Substituting the results of Equations (3.62) and (3.63) into Equation (3.71), we find that the inverse of the output SNR^2 is:

$$\frac{1}{SNR_{output}^2} = \frac{1}{\langle n(0) \rangle} \left\{ f(0) - 1 + \frac{1 + 2N(L)}{G(L)} + \frac{\mathfrak{m}N(L)[N(L)+1]}{G^2(L)\langle n(0) \rangle} \right\} \quad (3.72)$$

where $f(0)$ is the input Fano factor, defined in Equation (3.59).

So in the general case of input photon statistics, the amplifier noise factor is found by substituting Equation (3.72) into Equation (3.67), giving:

$$F = \frac{SNR_{input}^2}{\langle n(0) \rangle} \left\{ f(0) - 1 + \frac{1 + 2N(L)}{G(L)} + \frac{\mathfrak{m}N(L)[N(L)+1]}{G^2(L)\langle n(0) \rangle} \right\}. \quad (3.73)$$

If the input photon statistics are Poisson distributed, the input SNR^2 is given by Equation (3.70) and the Fano factor is unity, yielding an amplifier noise factor of:

$$F = \frac{1 + 2N}{G} + \frac{\mathfrak{m}N^2}{G^2 \langle n(0) \rangle} + \frac{\mathfrak{m}N}{G^2 \langle n(0) \rangle} \quad (3.74)$$

If the mean input is assumed to be high enough that $G\langle n(0) \rangle \gg N$ (this is equivalent to saying that the mean input level is much greater than n_{sp} at high gain), then the last two terms drop out and the noise factor becomes:

$$F = \frac{1 + 2N}{G} = \frac{1 + 2n_{sp}(G-1)}{G}. \quad (3.75)$$

In the high gain limit, the optical amplifier noise factor is reduced to:

$$\boxed{F(G \gg 1) = 2n_{sp}}$$ (3.76)

The discussion in Section 3.3 showed that the limiting value of n_{sp} is unity, therefore, *the noise factor of a high gain optical amplifier is always greater than 2.* If the noise factor is expressed in decibels, then $F \geq 3$ dB. This is the so-called *3 dB limit* or *quantum limit* referred to in the fiber communications literature.[46]

To apply the equations above to the solid-state Raman image amplifier, we must find an expression for n_{sp} that applies to Raman amplification. Following the formalism of C. Henry and R. Kazarinov[46], there are two fundamental sources of quantum noise in a system of coupled electrons and electromagnetic fields: 1.) spontaneous currents due to momentum fluctuations at optical frequencies of electrons localized by atomic or crystalline fields, and 2.) field fluctuations caused by the quantum-mechanical uncertainty of electric and magnetic fields. In quantum mechanics, the current is an operator that is related to the momentum operator, $\hat{p}$, by:

$$\hat{j} = \frac{e}{m}\hat{p}$$ (3.77)

where e is the electron charge and m is the electron mass (or effective mass). In noise theory, the frequency spectrum of the fluctuations of $\hat{j}$ is given by the Fourier transform of the correlation function $\langle \hat{j}(t)\hat{j}(0) \rangle$.

The other source of quantum noise arises from the quantum uncertainty of electric and magnetic fields. The electromagnetic field in a cavity can be decomposed into modes

which can be regarded as quantum harmonic oscillators. A mode has an energy spectrum with a level separation of $\hbar\omega$ and a ground-state energy of $\hbar\omega/2$, given by:

$$E_n = \left(n + \frac{1}{2}\right)\hbar\omega \tag{3.78}$$

The fluctuating electromagnetic field in the ground state referred to as the field of vacuum fluctuations.

Kubo[47] has shown that the induced current in an optical material is related to the susceptibility of the material by:

$$\chi(\omega) \equiv \frac{iV}{\hbar c} \int_0^\infty \left\langle \left[\hat{j}(\tau), \hat{j}^\dagger(0)\right]\right\rangle e^{i\omega\tau} d\tau \tag{3.79}$$

where V is a small volume with dimensions small compared to the wavelength of light but large enough to include many electronic states. The imaginary part of the susceptibility $\chi''(\omega)$ is given by:

$$\chi''(\omega) = \frac{V}{2\hbar c} \int_{-\infty}^\infty \left(\left\langle \hat{j}(\tau)\hat{j}^\dagger(0)\right\rangle - \left\langle \hat{j}^\dagger(0)\hat{j}(\tau)\right\rangle\right) e^{i\omega\tau} d\tau, \tag{3.80}$$

and is, therefore, the Fourier transform of the difference of antinormally and normally ordered correlation functions of spontaneous current-density operators at two different times. The same Fourier integrals occur when we are looking for the correlation functions of the positive frequency components of the spontaneous current operator, $\hat{j}_\omega$, which is found by:

$$\hat{j}_\omega = \frac{1}{\sqrt{2\pi}} \int_{-\infty}^\infty dt\, \hat{j}(t) e^{i\omega t}. \tag{3.81}$$

This leads to a statement of the fluctuation-dissipation theorem given by Callen and Welton[48] and also derived by Landau and Lifshitz[49], whereby the correlation functions of the frequency components of the spontaneous current operators are separately related to the imaginary part of the susceptibility:

$$\left\langle \hat{j}_\omega \hat{j}_{\omega'}^\dagger \right\rangle = \frac{2\hbar c}{V} \chi''(\omega) \delta(\omega - \omega')(\bar{n}_\omega + 1)$$

$$\left\langle \hat{j}_{\omega'}^\dagger \hat{j}_\omega \right\rangle = \frac{2\hbar c}{V} \chi''(\omega) \delta(\omega - \omega')\bar{n}_\omega$$

(3.82)

where $\bar{n}_\omega$ is the average optical-mode occupation factor of photons in equilibrium and can be written as:

$$\bar{n}_\omega = \frac{N_2}{N_1 - N_2} = -n_{sp}$$

(3.83)

where N_2 and N_1 are the populations of the upper and lower level, respectively, and n_{sp} is given in Equation (3.44) (where $\eta = 1$ has been assumed).

The fluctuation-dissipation theorem can be generalized to correlations between the operators at different spatial points.[46] In these generalized equations it will be convenient to express the imaginary part of the susceptibility in more commonly used optical constants,

$$\frac{4\pi}{c} \chi''(\omega) = k_\omega(\mathbf{x}) g_\omega(\mathbf{x}) = \frac{\omega^2}{c^2} \varepsilon_\omega''(\mathbf{x})$$

(3.84)

where $k_\omega(\mathbf{x})$ is the real propagation constant, $g_\omega(\mathbf{x})$ is the gain coefficient (or the attenuation coefficient), and $\varepsilon_\omega''(\mathbf{x})$ is the imaginary part of the dielectric function. These

quantities are related to the real and imaginary parts of the refractive index by $k_\omega(\mathbf{x}) = \omega n_\omega'(\mathbf{x})/c$ and $g_\omega(\mathbf{x}) = 2\omega n_\omega''(\mathbf{x})/c$. The generalized fluctuation-dissipation theorem is then given by:

$$\left(\frac{4\pi}{c}\right)^2 \left\langle \hat{j}_\omega(\mathbf{x}) \hat{j}_{\omega'}^\dagger(\mathbf{x}') \right\rangle = 8\pi\hbar k_\omega(\mathbf{x}) g_\omega(\mathbf{x})(n_{sp} - 1)\delta(\mathbf{x} - \mathbf{x}')\delta(\omega - \omega')$$

$$(3.85)$$

$$\left(\frac{4\pi}{c}\right)^2 \left\langle \hat{j}_{\omega'}^\dagger(\mathbf{x}') \hat{j}_\omega(\mathbf{x}) \right\rangle = 8\pi\hbar k_\omega(\mathbf{x}) g_\omega(\mathbf{x}) n_{sp}\delta(\mathbf{x} - \mathbf{x}')\delta(\omega - \omega').$$

The noise field in a Raman amplifier is due to amplified spontaneous Raman scattering. The optical frequency spontaneous currents that are the source of this noise field are due to fluctuations of atoms at optical phonon frequencies mixed with the pump field. This mixing is a result of the nonlinear interaction of the optical field with the atomic vibrations in the solid. The atomic motion is mostly due to the zero-point fluctuations of the vibrational levels. Following the notation of Henry and Kazarinov[46], assume that each optical phonon mode, q, is executing simple harmonic motion described in the usual way by quantized creation and annihilation operators, $\hat{b}_q^\dagger$ and $\hat{b}_q$, respectively. The energies of the vibrations are given by the Hamiltonian,

$$\hat{H}_L = \sum_q \hbar\Omega_q\left(\hat{b}_q^\dagger \hat{b}_q + \frac{1}{2}\right), \qquad (3.86)$$

where Ω_q is the angular frequency of mode q. The vibrational modes are in thermal equilibrium, with the operator averages given by:

$$\left\langle \hat{b}_q^\dagger \hat{b}_q \right\rangle = \bar{n}_q, \quad \left\langle \hat{b}_q \hat{b}_q^\dagger \right\rangle = \bar{n}_q + 1, \qquad (3.87)$$

where

$$\bar{n}_q = \frac{1}{\exp\left(\hbar\Omega_q/kT\right) - 1}.$$ (3.88)

Using the interaction representation, these operators have a time dependence of:

$$\hat{b}_q(t) = \hat{b}_q\, e^{-i\Omega_q t}, \quad \hat{b}_q^\dagger(t) = \hat{b}_q^\dagger\, e^{i\Omega_q t}.$$ (3.89)

The Raman scattering interaction can be written as a sum of products of the vibrational mode amplitudes $\left[\hat{b}_q + H.c.\right]$, the signal field at the Stokes frequency $\left[\hat{A}_{St}(t) + H.c.\right]$, and the pump field $\left[A_p \exp\left(-i\omega_p t\right) + c.c.\right]$, which is regarded as classical and monochromatic. Here $H.c.$ stands for the Hermitian conjugate and $c.c.$ stands for the complex conjugate. Calculating the spontaneous and induced currents in a small volume, V, and keeping only resonant terms with products of the fields that drive the lattice at an optical phonon frequency, the interaction Hamiltonian can be expressed as:

$$\hat{H}_{int} = \sum_q D_q \hat{b}_q^\dagger A_p e^{-i\omega_p t} \hat{A}_{St}^\dagger(t) + H.c.$$

$$= -\frac{V}{c}\hat{j}_R\, \hat{A}_{St}^\dagger(t) + H.c.$$ (3.90)

where the coefficients D_q give the strength of the interaction, and where an effective current-density operator $\hat{j}_R$ for Raman scattering has been defined. Using Equation (3.90) and Equation (3.89), this operator can be written as:

$$\hat{j}_R(t) = \frac{c}{V}\sum_q D_q \hat{b}_q^\dagger A_p e^{-i\left(\omega_p - \Omega_q\right)t}.$$ (3.91)

The frequency components of the Raman scattering current-density operator, $\hat{j}_{R\omega}$, are found by taking the Fourier transform of Equation (3.91), see Equation (3.81). The correlation functions of $\hat{j}_{R\omega}$ are found by using Equation (3.89) and by replacing $\sum_q$ with $V\int(dN/d\Omega_q)d\Omega_q$:

$$\left\langle \hat{j}_{R\omega}\hat{j}_{R\omega'}^{\dagger} \right\rangle = \frac{2\pi c^2}{V}\frac{dN}{d\Omega_q}\left|A_p\right|^2\left|D_q\right|^2\delta(\omega-\omega')\bar{n}_q$$

$$\left\langle \hat{j}_{R\omega'}^{\dagger}\hat{j}_{R\omega} \right\rangle = \frac{2\pi c^2}{V}\frac{dN}{d\Omega_q}\left|A_p\right|^2\left|D_q\right|^2\delta(\omega-\omega')(\bar{n}_q+1)$$

$$(3.92)$$

The Raman gain g_ω is related to the imaginary part of the susceptibility, which can be written with use of the Kubo formula (Equation (3.80)) as being proportional to the difference in the two correlation functions shown in Equation (3.92). The result can be expressed as:

$$g_\omega k_\omega = \frac{4\pi^2}{\hbar}\frac{dN}{d\Omega_q}\left|D_q\right|^2\left|A_p\right|^2 \qquad (3.93)$$

Finally, the fluctuation-dissipation theorem, which relates the spontaneous current correlation functions to gain, is found by combining Equations (3.92) and (3.93) while also replacing V^{-1} by $\delta(\mathbf{x}-\mathbf{x}')$:

$$\left(\frac{4\pi}{c}\right)^2\left\langle \hat{j}_{R\omega}(\mathbf{x})\hat{j}_{R\omega'}^{\dagger}(\mathbf{x}') \right\rangle = 8\pi\hbar k_\omega(\mathbf{x})g_\omega(\mathbf{x})\bar{n}_q(\mathbf{x})\delta(\mathbf{x}-\mathbf{x}')\delta(\omega-\omega')$$

$$(3.94)$$

$$\left(\frac{4\pi}{c}\right)^2\left\langle \hat{j}_{R\omega'}^{\dagger}(\mathbf{x}')\hat{j}_{R\omega}(\mathbf{x}) \right\rangle = 8\pi\hbar k_\omega(\mathbf{x})g_\omega(\mathbf{x})(\bar{n}_q(\mathbf{x})+1)\delta(\mathbf{x}-\mathbf{x}')\delta(\omega-\omega')$$

Comparing this equation with Equation (3.85), we see that the fluctuation-dissipation theorem for Raman scattering agrees with the theorem describing a conventional laser amplifier, provided that we make the substitution $n_{sp} = \bar{n}_q + 1$. The Raman shift for Ba(NO$_3$)$_2$ is 1047.3 cm^{-1}, which corresponds to a phonon of energy $E_q = \hbar\Omega_q = 2.08 \times 10^{-20}$ Joules. Using Equation (3.88), we find that the mean phonon occupation number at room temperature (300K) is $\bar{n}_q = 0.0066$. Thus, the spontaneous emission factor for a Raman amplifier is:

$$n_{sp} = 0.0066 + 1 \cong 1 \qquad (3.95)$$

showing that a Raman amplifier has a noise factor that is very close to the ideal amplifier, or, $F \cong 2$. Thus, *a solid-state Raman image amplifier at high gain operates at the quantum-noise limit.* Battle, Swanson, and Carlsten[50] came to the same conclusion using a different formalism incorporating full quantum equations for the Raman interaction.

How does this noise factor compare to the noise factor of standard image intensifiers? Assume the SNR of the optical image input to the Raman amplifier is determined by the Poisson noise of the incoming photons. Since for a Poisson random process the variance in photon number is equal to the mean number of photons, P_0, the input SNR can be written:

$$SNR_{input} = \sqrt{P_0} \qquad (3.96)$$

Substitution of the Raman amplifier spontaneous emission factor of $n_{sp} \cong 1$ into Equation (3.75) results in the expression for the Raman amplifier noise factor, F_R:

$$F_R = 2 - \frac{2}{G_R} + \frac{1}{G_R} = 2 - \frac{1}{G_R} \qquad (3.97)$$

where G_R is the overall Raman gain. If the Raman amplifier is followed by an optical detector with quantum efficiency, η, the overall amplifier + detector noise factor can be written as:[51]

$$F_R = 2 - \frac{2}{G_R} + \frac{1}{\eta G_R}. \qquad (3.98)$$

Thus the output SNR of the combined Raman amplifier and optical detector can be written as,

$$SNR_{output} = \frac{\sqrt{P_0}}{\sqrt{2 - \frac{2}{G_R} + \frac{1}{\eta G_R}}}, \qquad (3.99)$$

which in the high gain limit reduces to:

$$SNR_{output} = \sqrt{\frac{P_0}{2}} \qquad (3.100)$$

This result shows that *preamplification of optical signals by solid-state Raman scattering can compensate for low quantum efficiency detectors*. The net result of preamplification followed by detection is equivalent to an optical detector with a quantum efficiency of 50%.

In the SWIR region region around 1.56 μm, photocathodes are just now becoming available and their quantum efficiencies are low (less than 20%). Also, the process of electron multiplication in image intensifiers results in both image blurring and additional image noise. Recent work with intensified CCDs has shown that the noise factor of these

devices is a complicated function of microchannel plate (MCP) gain noise and other additive noise.[52] The overall SNR performance of ICCDs is also degraded by the quantum efficiency of the sensing photocathode. As a result, the output SNR for an ICCD device can be written as:

$$SNR_{output,ICCD} = \frac{\sqrt{\eta_{pc} P_0}}{\sqrt{F_{ICCD}}}$$ (3.101)

where η_{pc} is the photocathode quantum efficiency and F_{ICCD} is the noise factor of the ICCD. Recent studies have shown that the noise factors of current intensifiers are in the range:

$$F_{ICCD} \cong \begin{cases} 1.6 - 2.2 \text{ for GEN II} \\ 3.5 - 4.2 \text{ for GEN III} \end{cases}$$ (3.102)

and photocathode quantum efficiencies near 1.56 μm are at most 20%.

By taking the ratio of Equations (3.99) and (3.101), the figure-of-merit (FOM) performance gain of the SSRIA over the ICCD imaging system is:

$$FOM = \frac{\sqrt{F_{ICCD}}}{\sqrt{\eta_{pc}}} \frac{1}{\sqrt{2 - \dfrac{2}{G_{SSRIA}} + \dfrac{1}{\eta_d G_{SSRIA}}}}$$ (3.103)

Giving the Raman amplifier gain a value of 1000 and assuming the use of a HgCdTe array with a quantum efficiency of 60%, equation (3.103) gives an SNR performance gain of at least:

$$FOM = 2 \text{ to } 3$$ (3.104)

over the use of an intensifier-CCD combination. This SNR advantage directly translates into a factor of 2 to 3 greater range for a LIDAR system viewing a resolved target, with all other system parameters being equal.

Another advantage in using SSRIA over ICCDs is the fact that the noise factor of the Raman image amplifier is not very sensitive to the overall Raman gain. In ICCDs, the noise factor of the MCP increases dramatically with lower gain. This limits the maximum SNR of an intensified image. Figure 3.5-1 shows a comparison of noise factors of the SSRIA and intensified CCDs as a function of gain. At lower gains, the noise factor of SSRIA is significantly lower than the standard image tubes.

Figure 3.5-2 shows the overall SNR comparison between SSRIA and ICCDs as a function of input light level (given in input photons per detector pixel). The red line shows the upper limit of pure shot noise arising from the Poisson statistics of arriving photons. Shown in blue, the SNR of the SSRIA is just below this ultimate limit and tracks the shot noise through four decades of input light level. The ICCD SNR is shown in magenta and falls significantly below the SNR attained by SSRIA. In addition, the ICCD SNR essentially saturates at high input light levels due to the rising noise factor of the microchannel plate (MCP).
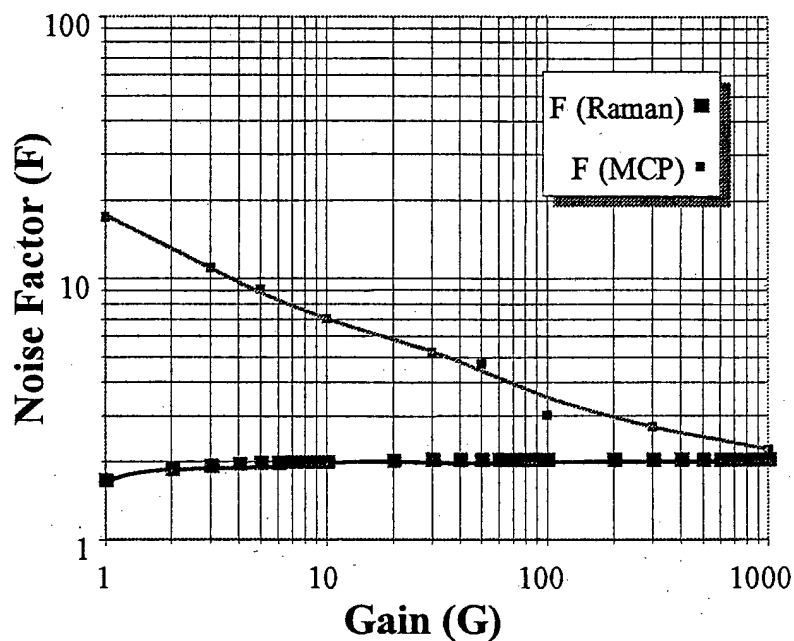
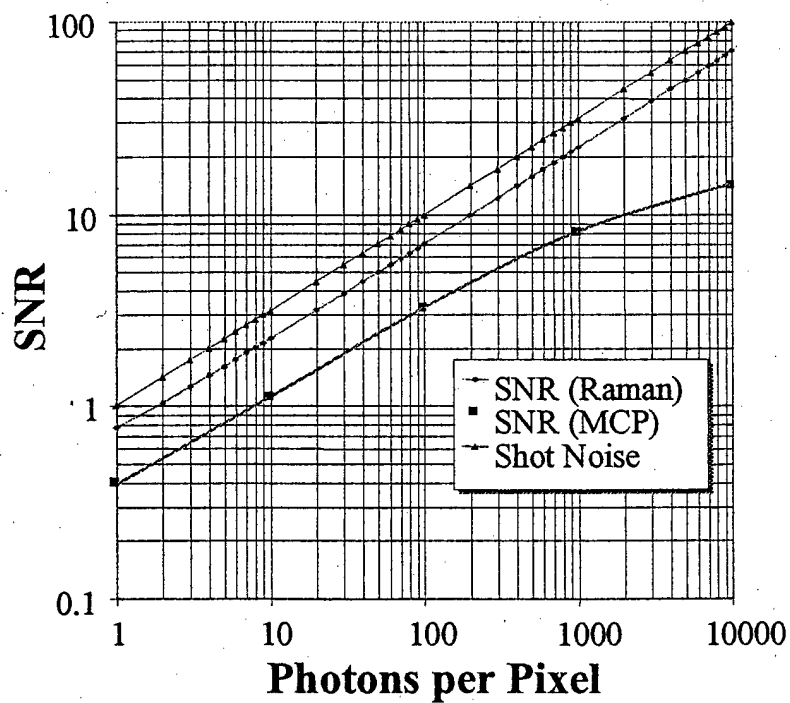Figure 3.5-1 Noise Factor Comparison of SSRIA and ICCDs

Figure 3.5-2 SNR Comparison of SSRIA and ICCDs

4 *Raman Image Amplifier Design*

4.1 Optical Design Properties of Raman Image Amplifiers

Figure 4.1-1 shows the optical layout for the Raman image amplifier used in study. A standard USAF 1951 tri-bar resolution target on a glass slide was placed at the focal plane of the Fourier transform lens. The resolution target was trans-illuminated from the left by the expanded Stokes beam. The middle of the crystal was placed in the back focal plane of the same lens. With this configuration, the two-dimensional Fourier transform of the resolution target appears in the middle of the crystal. The Fourier transform distribution is then amplified by interaction with the pump beam in the Raman crystal. The amplified transform is also in the front focal plane of the inverse Fourier transform lens with the IR vidicon camera in the back focal plane. Thus the inverse Fourier transform lens forms a real, amplified image of the resolution target on the camera plane.

The amplifier pump beam was focused with a +750 mm lens and injected co-axially into the crystal by a dichroic beamsplitter that is a high reflector at 1.34 μm and has high transmission at 1.56 μm. At the back end of the crystal, another dichroic beamsplitter reflects the remaining 1.34 μm pump beam to a dump. In addition, several long-pass filters were placed in front of the camera to further reject any remaining pump light.
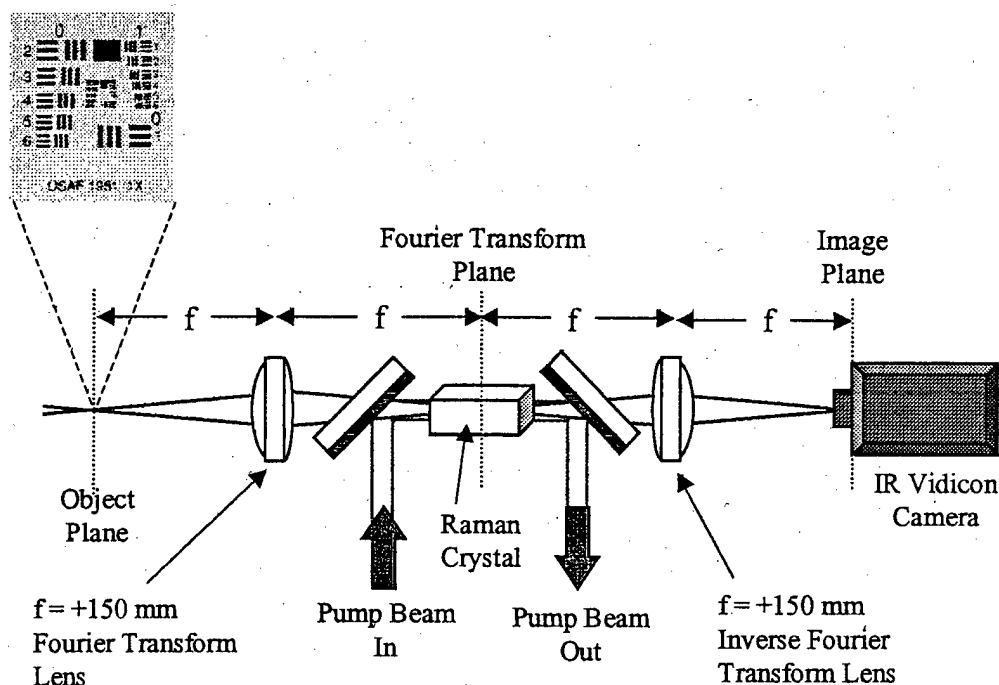
Figure 4.1-1   Optical Layout of Raman Image Amplifier

Figure 4.1-2 illustrates the operation of the SSRIA in this study. The resolution target is called "image" in this figure. The Fourier transform, FT{}, of the image appears in the center of the crystal. The Raman interaction of FT{image} and the injected pump beam amplifies FT{image} to Amp[FT{image}], while simultaneously depleting the pump beam. The inverse Fourier transform lens then forms the amplified image, Amp[image], at the camera plane.

There are several things to note about Figure 4.1-2. First, the pump beam distribution shown in the figure is the actual amplifier pump beam distribution measured at the Fourier plane of the SSRIA. Note that the astigmatism present in the amplifier pump cavity results in a non-circularly symmetric focused beam. The FT{image} shows that the vertical and horizontal resolution bars transform to vertical and horizontal structure

on the Fourier transform (the cross-shaped feature in FT{image}). Higher spatial frequencies, i.e. closer spaced tri-bars in the resolution target, transform to corresponding structure that is further from the center of the Fourier transform. The overall DC light level of the image is transformed to a peak in the center of the FT. As a result, the pump beam distribution controls the spatial frequency content of the final amplified image. High spatial frequencies that are transformed outside of the pump beam distribution receive no amplification and are lost in the final amplified image. Thus the pump beam distribution in the Raman crystal is the controlling factor for the Modulation Transfer Function (MTF) of SSRIA. Note that since the pump beam distribution is non-circularly symmetric, the MTF in the horizontal and vertical directions will be different.
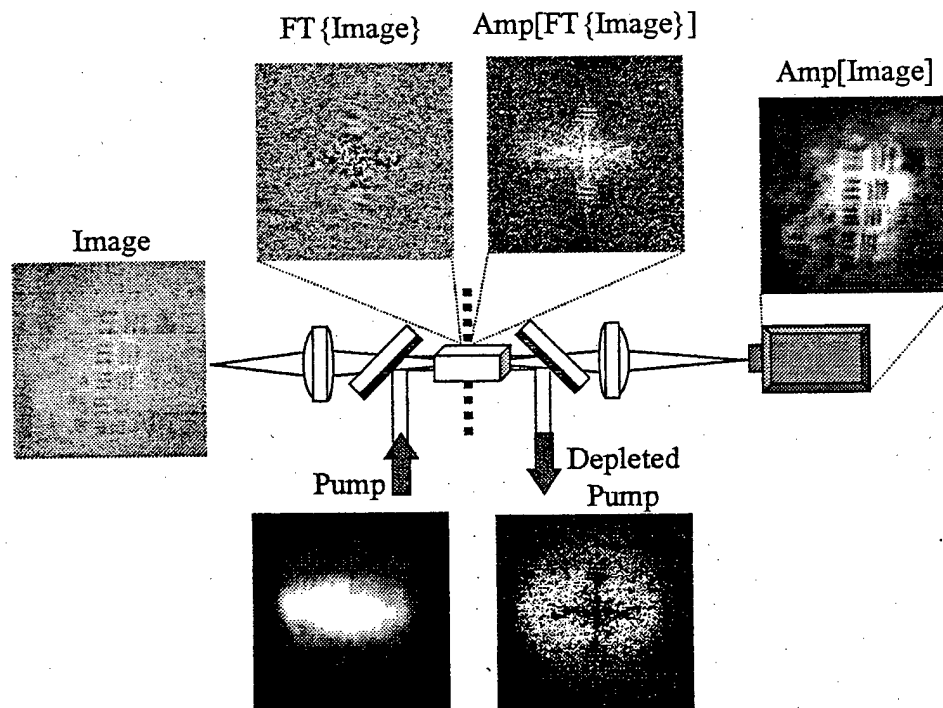

Figure 4.1-2   The Raman Image Amplification Process

A non-circularly symmetric pump beam is not ideal for high-fidelity image amplification. A solution to this problem is illustrated in Figure 4.1-3. By injecting the pump at an angle to a slab-like Raman crystal and taking advantage of total internal reflection, the pump beam zig-zags inside the crystal and forms a more uniform gain distribution for any input beam spatial distribution.
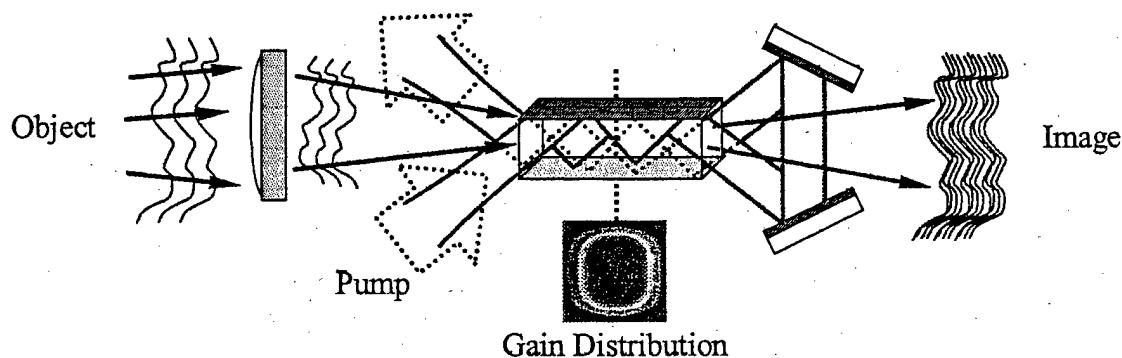

Figure 4.1-3   Smooth Raman Gain Distribution by Pump Zig-Zag

Another optical design consideration for SSRIAs involves the optical invariant at the crystal. The optical invariant, I, at a pupil plane in an optical system is defined by:

$$I = hnu \qquad (1.1)$$

where h is the height of the paraxial ray, n is the index of refraction, and u is the angle of the chief ray. Because the center of the Raman crystal is a Fourier transform plane of the object, it is also a pupil plane of the optical system. Figure 4.1-4 shows a chief ray (in red) passing through the pumped region inside the Raman crystal. The maximum angle subtended by this chief ray is determined by the geometry of the pumped region:

$$u_{max} \approx \frac{h}{\frac{L_R}{2}} = \frac{2h}{L_R} \qquad (1.2)$$

since any greater angle will result in non-overlap of the chief ray with the pump beam ($2h$ is the diameter of the pumped region). Figure 4.1-4 gives the resulting expression for the optical invariant at the crystal, where A is the cross-sectional area of the pumped region. Since the optical invariant must be the same everywhere in the optical system, the optical invariant at the entrance pupil of a receiving telescope coupled to the SSRIA must be equal to the invariant at the crystal. The expression for the optical invariant at the receiving telescope is shown in Figure 4.1-5. It shows that the invariant at the telescope is the product of the half field-of-view angle and the radius of the telescope optic. Thus, the pumping geometry in the SSRIA crystal is directly connected to the FOV and aperture size that can be used in a lidar system.
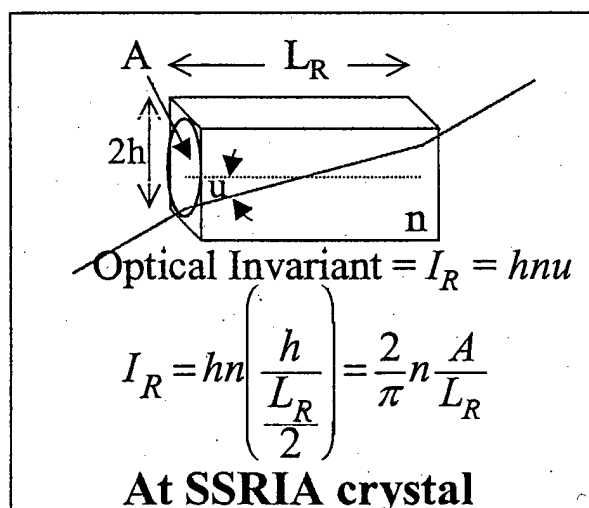

Optical Invariant $= I_R = hnu$

$$I_R = hn\left(\frac{h}{\frac{L_R}{2}}\right) = \frac{2}{\pi}n\frac{A}{L_R}$$

At SSRIA crystal

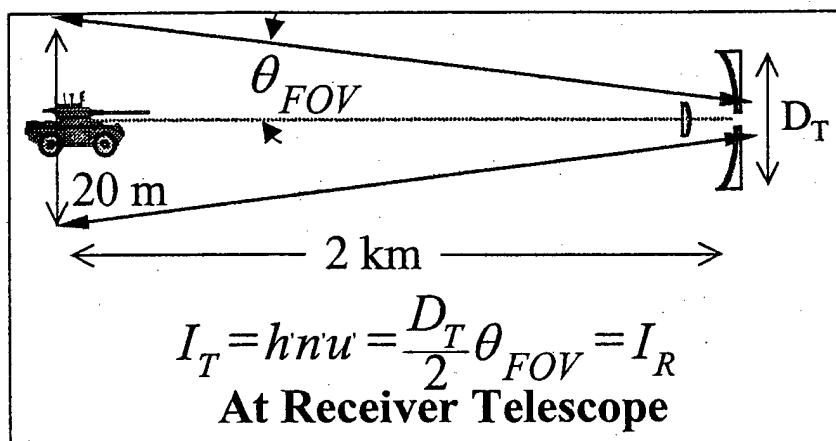Figure 4.1-4   Optical Invariant at the SSRIA Crystal

Figure 4.1-5   Optical Invariant at the Receiver Telescope

For example, if we would like to image tanks and other vehicles at a range of 2 kilometers, the total field imaged by the system should be 20 meters to encompass the entire vehicle. The half FOV is then $10m/2000m = 0.005rad$. A reasonable aperture size for this demonstrator is a telescope diameter of 30 cm. So the optical invariant is $I = 0.075cm$ and the required energy per pulse for an image amplification of 1000 is then $E_p = 143mJ$.

4.2 Optical Resolution of Raman Amplifiers

Figure 4.2-1 gives a summary of findings on the optical resolution of the SSRIA and compares SSRIA with the intensified CCD. In most ICCD systems, the resolution is limited by the combined effects of input and/or output fiber optic bundles, the electron optics of the input and output MCP spacings, and microchannel plate (MCP) blur. Current Gen II wafer tubes have limiting resolutions of 25-32 line pairs per millimeter.[53]

The SSRIA optical resolution is governed by the size of the pumped region in the Raman amplifier crystal. This is due to the Fourier transform relationship between the

optical image plane and the center of the crystal plane. Optical resolution is typically specified by the Modulation Transfer Function (MTF) which is defined by:

$$MTF = \frac{I_{max} - I_{min}}{I_{max} + I_{min}} \qquad (1.3)$$

where I_{max} and I_{min} are the maximum and minimum irradiance values, respectively, of the image of a sine-wave pattern. The limiting resolution is usually defined as the spatial frequency at which the MTF is 3%. This is considered the minimum contrast which can be seen by the eye. The advantage in using MTF to characterize resolution is that the MTF for each separate part of an optical system can be found separately and then the product of these separate MTFs gives the MTF of the entire system.
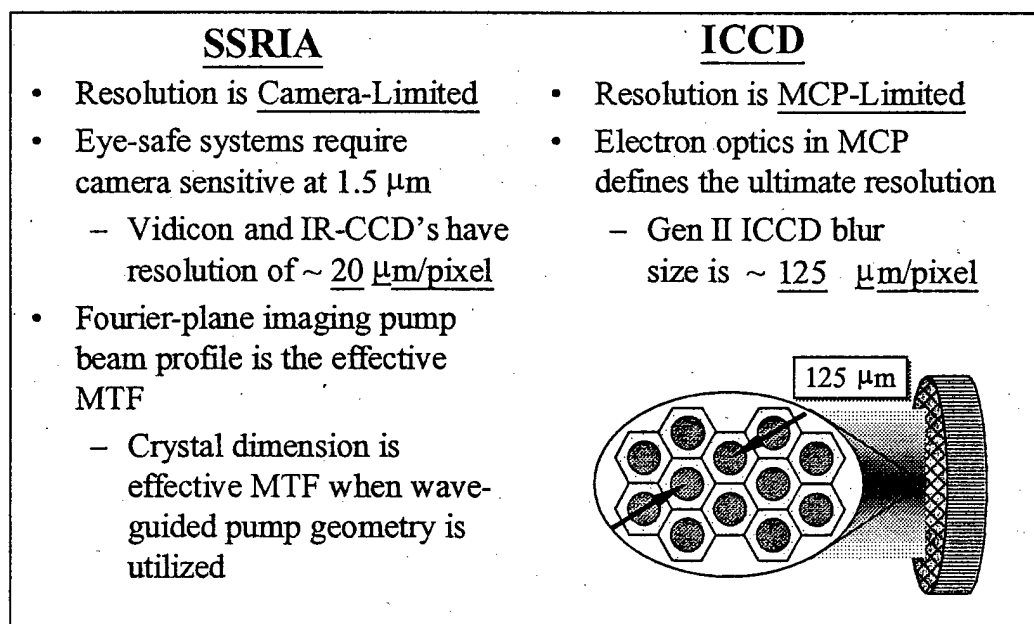

Figure 4.2-1   Resolution Comparison of SSRIA and ICCD

The MTF contribution of the Raman Image Amplifier can be found by a consideration of the Fourier transform relationship between the object plane and the center of the crystal plane. Figure 4.2-2 shows two 1-dimensional sine wave objects on the left and their corresponding Fourier transforms on the right.
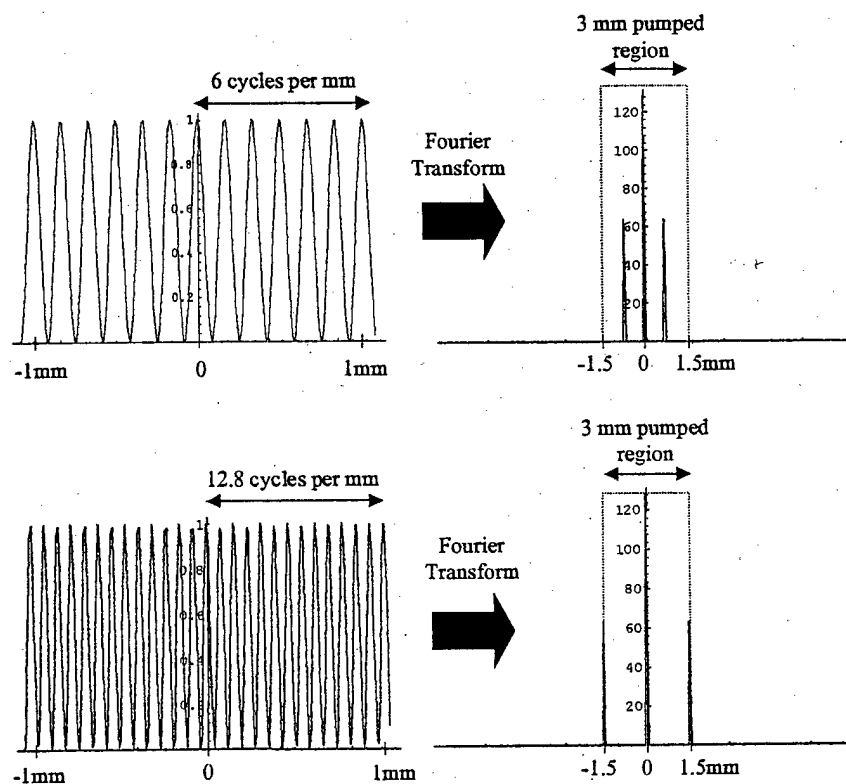

Figure 4.2-2   Fourier Transforms of Sine Wave Objects

The first object has a spatial frequency of 6 cycles per mm and the second object has a higher spatial frequency of 12.8 cycles per mm. The Fourier transforms are seen to consist of three distinct peaks: a central peak that corresponds to the DC light level, a positive frequency peak on the right, and a negative frequency peak on the left. The two outer peaks thus contain the high frequency information. As seen from the bottom transform pairs, higher spatial frequencies are mapped further from the center of the Raman crystal until, at the cutoff frequency of the SSRIA, the outer peaks are at the edge

of the pump beam in the crystal. Higher spatial frequencies than the cutoff frequency are mapped outside of the pump region and are not amplified. The cutoff frequency of the SSRIA is controlled by the diameter of the pumped region, d, and the focal length of the inverse Fourier transform lens, f_2, by the equation:

$$\rho_{SSRIA} = \left| \frac{d}{f_2 \lambda} \right|$$

(1.4)

4.3 Sunlight Background Rejection

Figure 4.3-1 shows a schematic comparison of the spectral characteristics of SSRIA and ICCDs. For a typical ICCD imaging lidar system, the use of a photocathode implies a broad spectral response. To limit the background light due to sunlight, a narrow bandpass optical filter is used in front of the ICCD optics. However, because of the shift of the center passing wavelength with angle inherent in multi-layer dielectric bandpass filters, in order to work with a reasonable field-of-view the bandpass must be limited to around 10 nanometers FWHM. Any narrower and the FOV must be decreased accordingly. Figure 4.3-1 shows that the background light within a 10 nanometer bandpass is amplified by the ICCD and appears as noise in the image.

The spectral width of the Raman amplification process is on the order of 0.1 nanometer and is not sensitive to angular shift. Thus, the sunlight background is reduced by a factor of 100 when using SSRIA compared to ICCDs.
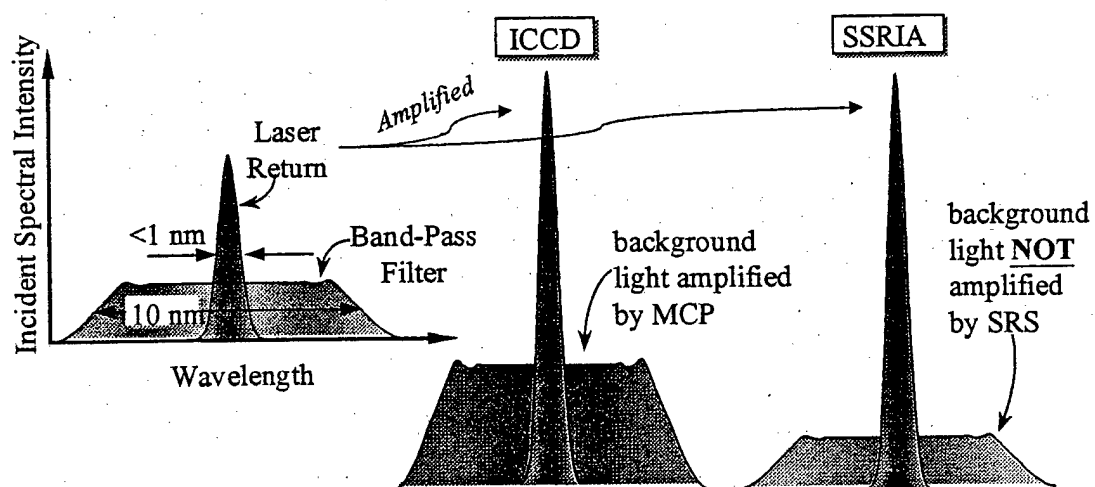
Figure 4.3-1   Spectral Acceptance Comparison

5   Raman Image Amplifier Results

The most significant findings and results produced by this research are:

SSRIA is an eye-safe LIDAR technology operating at 1.56 μm.

SSRIA can amplify low-level IR images by a factor up to 10^6.

SSRIA adds only quantum-limited noise to the amplified image.

SSRIA can compensate for low quantum efficiency IR detectors and reduces the need to cool detectors to reduce thermal noise.

SSRIA provides range-gated LIDAR images with temporal range-gates as short as $2 - 10$ nanoseconds.

A LIDAR system using SSRIA will result in an image signal-to-noise ratio (SNR) gain of more than 2 to 3 over current intensified CCD technology.

Optical resolution of SSRIA can be much higher than ICCDs.

SSRIA reduces the amount of sunlight background in gated images by a factor of 10 or more.

SSRIA can be used to perform optical image processing functions such as image enhancement and automatic target detection/recognition.

5.1 Stokes Illuminator Laser

5.1.1 Stokes Illuminator Laser Design

The Stokes seed laser resonator design was based on high peak-, high average-power, eye-safe Raman resonators previously demonstrated. Using data obtained from existing high power, eye-safe systems, and applying well-known scaling laws, the multimode spot-size required in the Raman crystal was sized to obtain the best energy conversion efficiency.

Considering these results, the optimized resonator was designed using the generalized resonator design code, called *Lasica®*. The resonator design optimization included (1) maximizing the energy extraction efficiency, (2) minimizing the accrued round-trip aberrations, (3) minimizing the potential for optical damage, (4) mode-matching the Raman cavity to the pump cavity, and (5) selection of the proper Raman output coupling percentage - Raman gain combination to ensure the desired temporal pulse profile.

Figure 5.1.1-1 shows the layout of the Stokes laser. It is a Q-switched, intracavity Raman laser that uses a nonlinear optical crystal of $Ba(NO_3)_2$ to shift the output wavelength from the fundamental 1.34 μm line of Nd:YAG to the eye-safe, Stokes-shifted wavelength of 1.56 μm. The Nd:YAG rod is pumped by a flashlamp and the fundamental stable resonator cavity at 1.34 μm is defined by a 1 meter radius-of-curvature (ROC) high reflectivity mirror at the rear end and a 10 meter ROC high reflectivity mirror at the front end. This 10 meter ROC mirror is shared by the Stokes resonator cavity. The 1.34 μm light path is shown in red in Figure 5.1.1-1. The Stokes

resonator cavity, which has a 1.56 μm light path shown in blue, consists of the 10 meter

HR, the crystal, and the flat, 50% reflective, output coupler. A dichroic beamsplitter at a
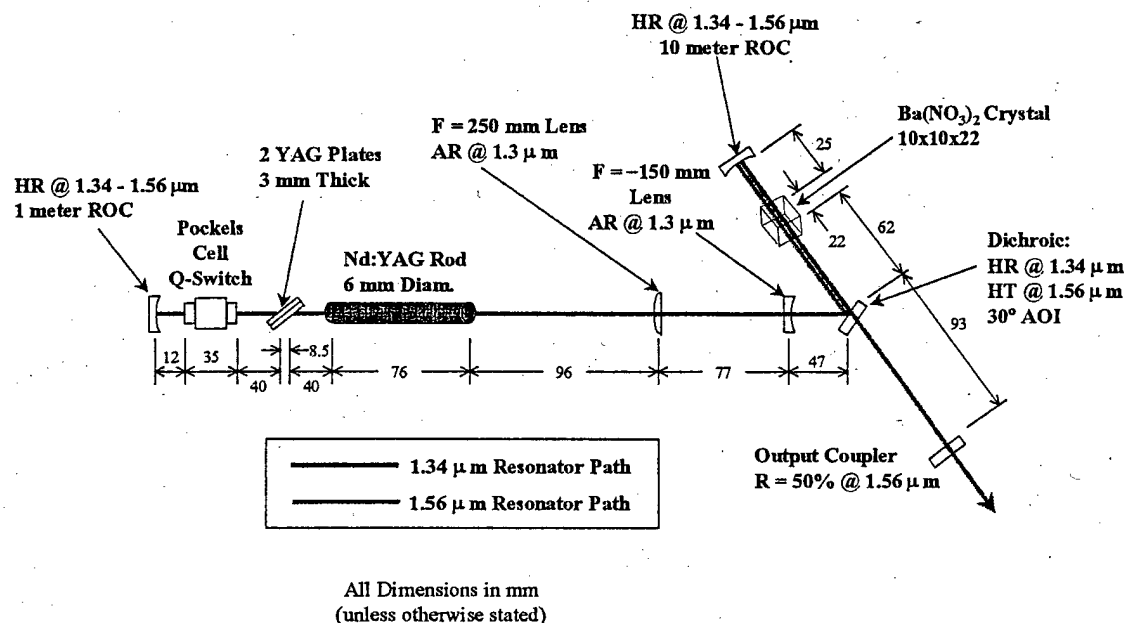
30° incidence angle couples the two cavities.

Figure 5.1.1-1 Stokes Laser Layout

Figure 5.1.1-2 shows the single-mode beam radius in the fundamental cavity as a

function of distance from the rear HR. Note that the intracavity telescope acts to decrease

the beam radius inside the nonlinear crystal and thus increases the intensity of the pump

beam in the crystal. The limiting aperture in the fundamental cavity is the rod itself and

so at the higher pumping levels (up to 48.8 Joules lamp energy), the fundamental beam is

highly multi-mode and extracts maximum energy from the rod. Figure 5.1.1-3 shows the

multi-mode beam radius as a function of distance from the rear HR (dashed red line).

Also shown in the figure is the single-mode beam radius for comparison (solid red line).

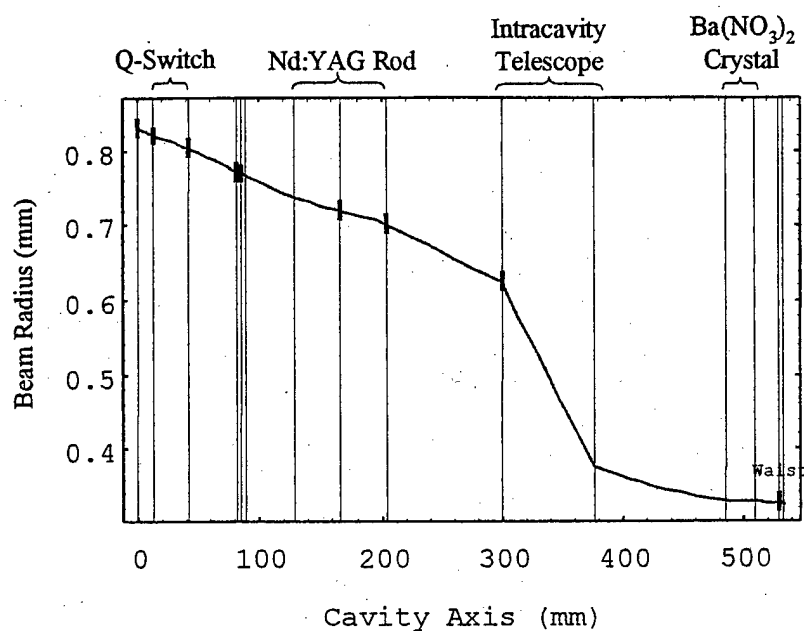Note that the beam radius in the Raman crystal is 1.2 mm.

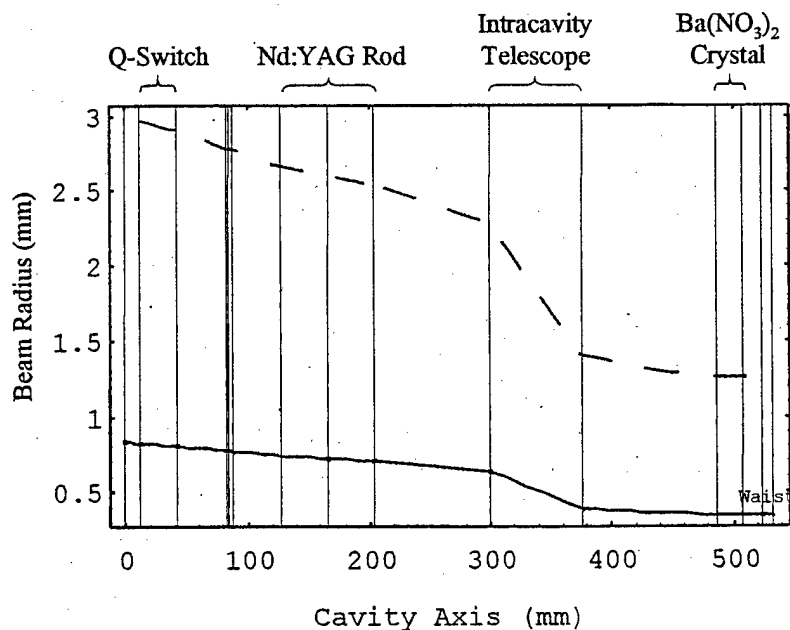**Figure 5.1.1-2 Single-mode Beam Size of 1.34 μm Resonator**

Figure 5.1.1-3 Multi-mode Beam Size of 1.34 μm Resonator

An important consideration in the design of these intracavity Raman lasers is that the

multi-mode spot size inside the crystal must provide a sufficiently high intensity to reach

the Raman laser threshold and should be matched in size to the single-mode Stokes beam size. Due to the phenomenon of Raman beam clean-up, the Stokes beam produced by intracavity Raman lasers is typically close to the fundamental Gaussian mode of the Stokes cavity regardless of the mode structure of the pump beam. Thus for maximum energy coupling and efficiency, the multi-mode pump radius should match the single-mode Stokes radius. However, this is not always possible because of the coupled cavity dynamics. Too much pump intensity inside the crystal can cause the creation of multiple Raman pulses or of Raman cascading to the second Stokes wavelength. Figure 5.1.1-4 shows the Stokes single-mode beam radius inside the Stokes cavity. The single-mode beam radius is 0.83 mm, leading to an area mismatch efficiency of

$$\eta_{mode} = \left(\frac{r_{Stokes}}{r_{pump}} \right)^2 = \left(\frac{0.83}{1.2} \right)^2 = 0.48 \tag{5.1}$$

With the use of an unstable resonator for the Stokes cavity, this efficiency can be made to approach one. For this study the efficiency was judged adequate.
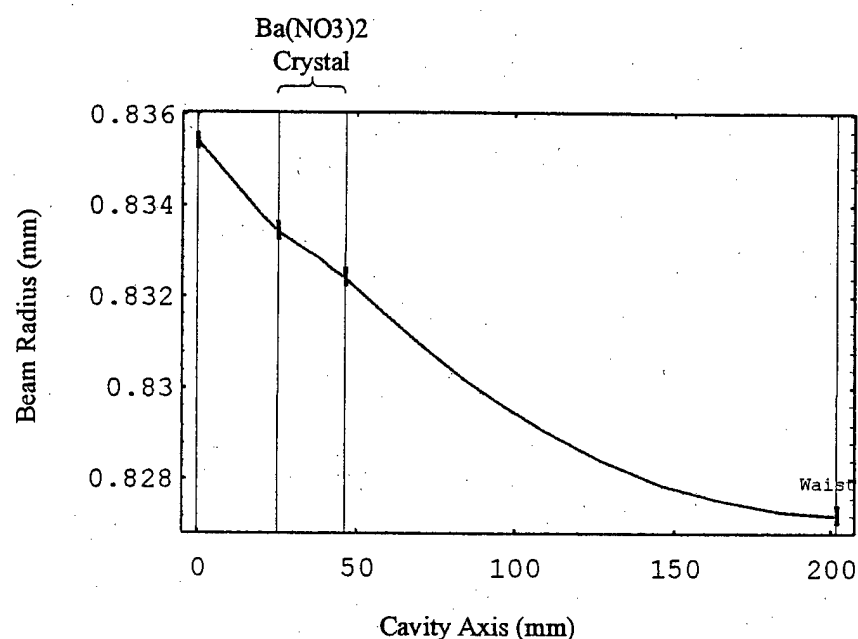
Ba(NO3)2
Crystal

Figure 5.1.1-4 Stokes Cavity Design (Single-mode)

5.1.2 Stokes Laser Characterization

The Stokes seed laser was built to verify and characterize the design. The output power and temporal pulse profiles were measured and monitored for stability. Figure 5.1.2-1 shows the spatial beam profiles of both the fundamental beam at 1.34 µm and the Stokes beam at 1.56 µm. The pump beam shows the expected highly multi-mode spatial structure. The Stokes beam is very close to the single transverse mode or TEM_{00} spatial structure. The pump/Stokes area mismatch is clearly seen in this figure and matches the size predicted by the spatial model.
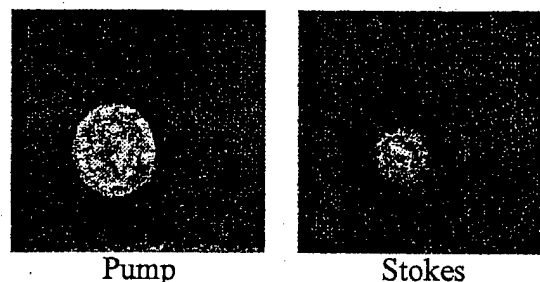
Pump   Stokes
Figure 5.1.2-1 Pump and Stokes Beam Profiles

Figure 5.1.2-2 shows the measured input/output characteristic curve for the seed Stokes laser. The output energy per pulse was measured at a pulse repetition frequency of 1 Hz. At the maximum lamp input energy of 48.8 Joules, the output energy at 1.56 μm was 30 milliJoules. For the SSRIA experiments described in Section 2.5, the lamp input energy was set at 35 J, corresponding to an output Stokes energy of 12 mJ.
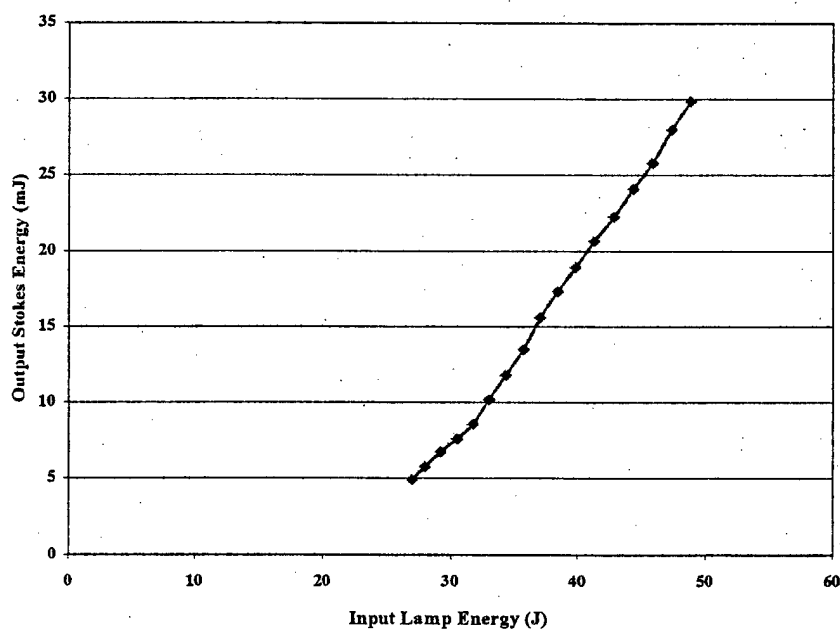

Figure 5.1.2-2 Stokes Laser Input/Output Characteristic

Figure 5.1.2-3 shows the temporal pulse profiles of the fundamental and Stokes beams. The fundamental pump beam rises until the Stokes conversion threshold is

achieved. At that point the pump is rapidly converted to the Stokes wavelength and the Stokes pulse rises very sharply. The Stokes pulse full width at half maximum (FWHM) is seen to be 6.9 nsec. The Stokes pulse depletes most, but not all, of the population inversion in the Nd:YAG. This is evinced by the second hump of the pump beam.
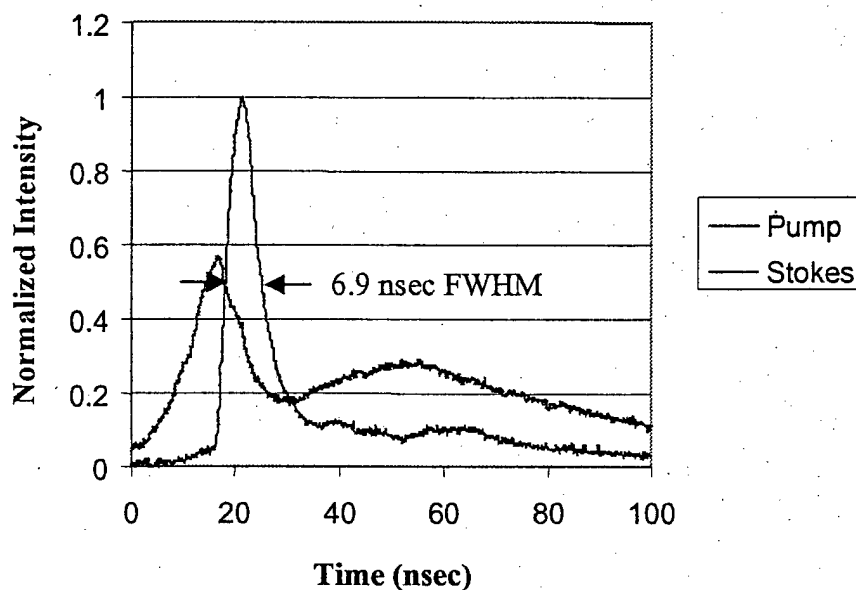
Figure 5.1.2-3 Temporal Pulse Profiles

5.2 Raman Amplifier Pump Laser

5.2.1 Raman Amplifier Pump Laser Design

The Raman amplifier pump laser design is a flashlamp-pumped Nd:YAG power oscillator configuration to produce the pump power at 1.34 μm. The resonator design was accomplished using the generalized resonator design code, *Lasica*®. The oscillator/amplifier design included (1) maximizing the energy extraction efficiency, (2) minimizing the accrued oscillator round-trip and amplifier single-pass aberrations, (3)

minimizing the potential for optical damage, (4) matching the cross-sectional area of the SSRIA crystal to ensure optimum coupling and (5) suppression of parasitic 1.06 μm oscillation.

Figure 5.2.1-1 shows the layout of the amplifier pump laser. It is a Q-switched Nd:YAG laser operating at the fundamental wavelength of 1.34 μm. The Nd:YAG rod is pumped by a flashlamp and the fundamental stable resonator cavity at 1.34 μm is defined by a 20 meter radius-of-curvature (ROC) high reflectivity mirror at the rear end and a 4 meter ROC, 50% reflectivity output coupler at the front end. Also included in the cavity are a Pockels cell Q-switch, 4 YAG plate polarizers, and two mirrors that are highly reflective at 1.06 μm and highly transmissive at 1.34 μm. These two mirrors are necessary to suppress laser oscillation at 1.06 μm.
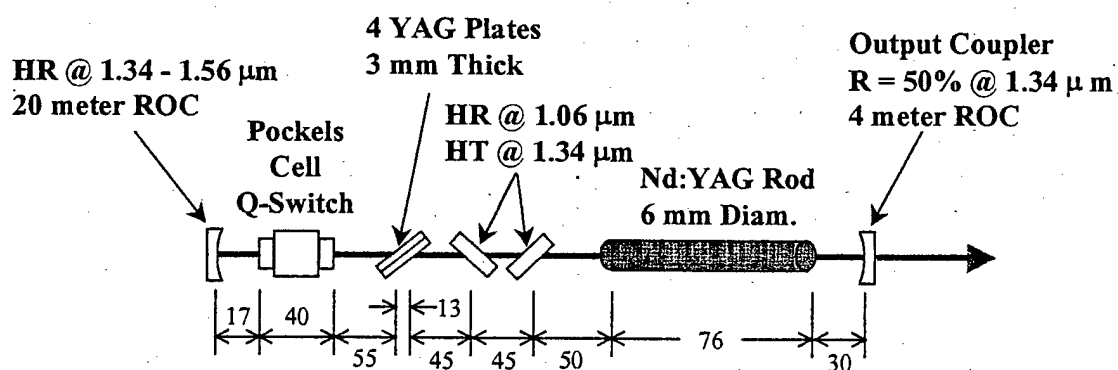
All Dimensions in mm
(unless otherwise stated)

Figure 5.2.1-1 Amplifier Pump Laser Layout

Figure 5.2.1-2 shows the single-mode beam radius in the pump laser cavity. The red curve shows the beam radius in the x-axis (i.e. in the horizontal plane, parallel to the optical table) and the blue curve shows the beam radius in the orthogonal axis. The introduction of the YAG plate polarizers and 1.06 μm mirrors cause a small amount of astigmatism in the optical cavity.
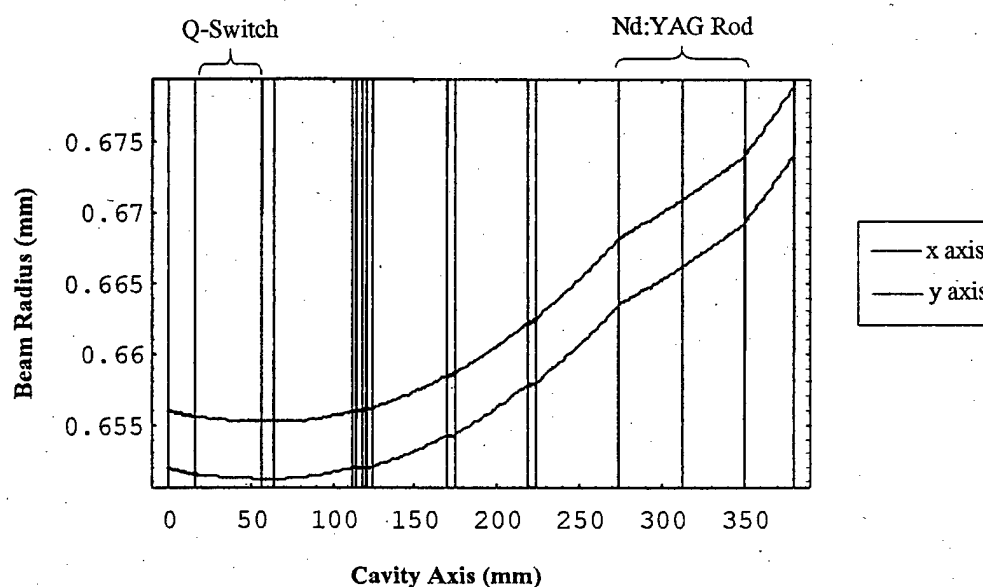

Figure 5.2.1-2 Pump Laser Single-mode Cavity

Figure 5.2.1-3 shows the multi-mode cavity plot for the pump laser. The limiting aperture in the cavity is the rod itself and so at the higher pumping levels (up to 70 Joules lamp energy), the fundamental beam is highly multi-mode and extracts maximum energy from the rod.

Q-Switch   Nd:YAG Rod
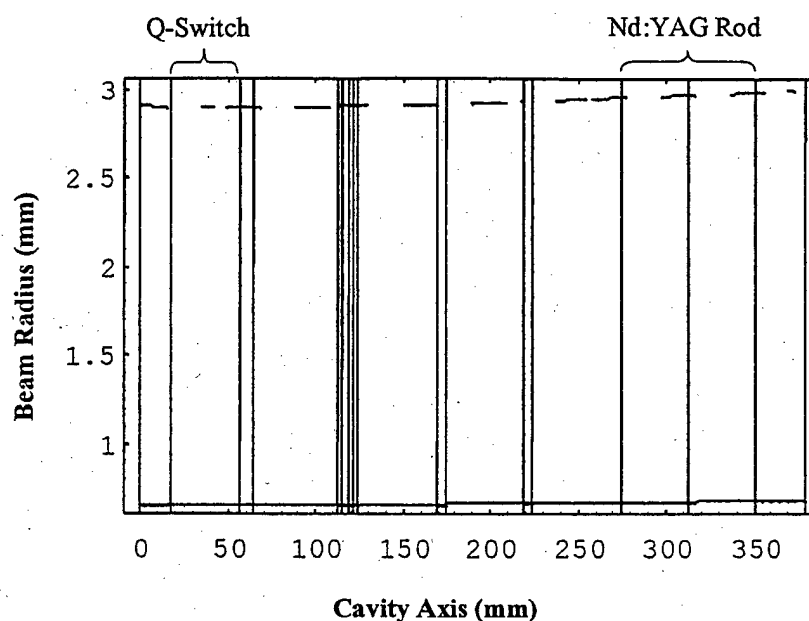
Figure 5.2.1-3 Pump Laser Multi-mode Cavity

5.2.2 Pump Laser Characterization

The designed Raman amplifier pump laser was built to verify and characterize the design. The output power and temporal pulse profiles were measured and monitored for stability. Figure 5.2.2-1 shows the spatial beam profile of the amplifier pump beam at 1.34 μm. The pump beam shows the expected highly multi-mode spatial structure.

Figure 5.2.2-1 Pump Laser Beam Profile

Figure 5.2.2-2 shows the measured input/output characteristic curve for the amplifier pump laser. The output energy per pulse was measured at a pulse repetition frequency of

1 Hz. At the maximum lamp input energy of 70.0 Joules, the output energy at 1.34 μm

was 95 milliJoules. However, as is evident from the change of slope in the figure, at

around 45 J lamp energy some parasitic oscillation at 1.06 μm starts to rob energy from

the 1.34 μm beam. For this reason, most of the experiments described in Section 5.3
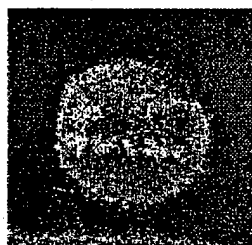
used 43 J of input lamp energy resulting in less than 80 mJ of pump energy per pulse.
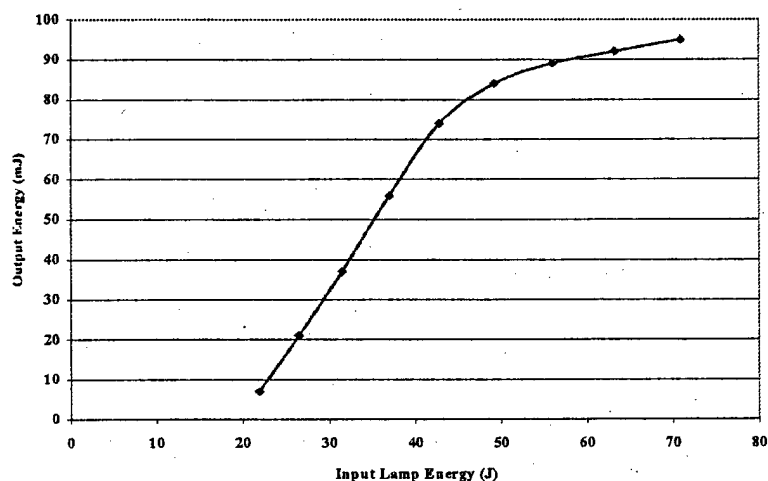
Figure 5.2.2-2 Pump Laser Input/Output Characteristic

Figure 5.2.2-3 shows the temporal pulse profile of the amplifier pump beam as taken

by the oscilloscope (the vertical scale is inverted – increasing pulse intensity is

downward). The pump beam is shown in green and the Stokes pulse is shown in red on

the same time scale. The measured FWHM of the amplifier pump pulse is shown to be

43.15 nsec on the right side of the figure. Note that the horizontal scale is 10 nsec per

division.

(Green – amplifier pump pulse; Red – Stokes pulse)
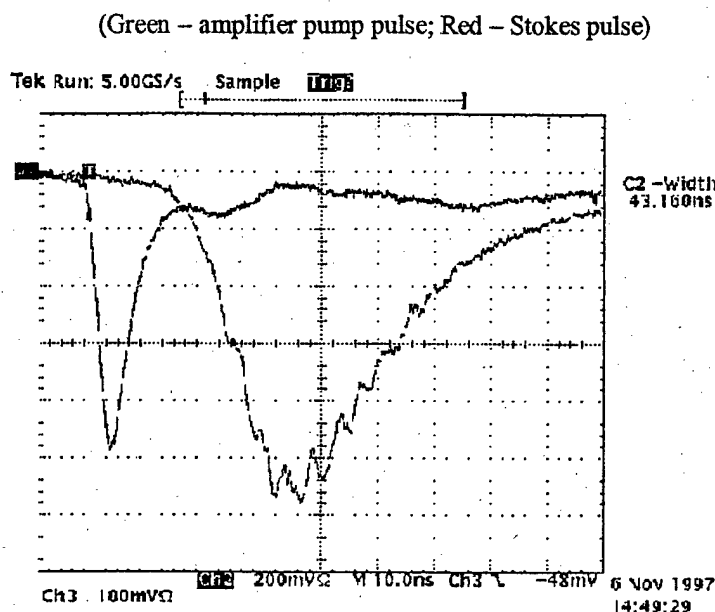
Figure 5.2.2-3 Amplifier Temporal Pulse Profile

5.3 Raman Image Amplification Results

5.3.1 SSRIA Design

Figure 5.3.1-1 shows the SSRIA Demonstrator layout that was used to demonstrate the feasibility of SSRIA. The Demonstrator consists of three main optical parts: 1) the Stokes seed source laser, which is a Q-switched, flashlamp-pumped, intracavity Raman laser emitting up to 30 mJ per pulse of 1.56 μm radiation at a 1 Hz repetition rate, 2) the Raman amplifier pump laser, which is a Q-switched, flashlamp-pumped Nd:YAG laser emitting up to 89 mJ per pulse of 1.34 μm radiation at a 1 Hz repetition rate, and 3) the Solid-state Raman Image Amplifier which is configured in a Fourier transform arrangement where the amplifier crystal of $Ba(NO_3)_2$ is at the Fourier transform plane of the input image.

A standard Air Force tri-bar resolution target was transilluminated with the expanded 1.56 μm laser pulses from the Seed Stokes source laser. The illuminating laser pulses were greatly attenuated with neutral density filters up to a total optical density value of 9.8. The amplifier pump laser was timed to overlap the illuminating pulses inside the Raman amplifier crystal. The output energy per pulse of the amplifier laser could be adjusted to moderate the amount of gain applied to the illuminating pulses. Figure 5.3.1-2, on the left, shows the image produced when no amplifier pump pulses were applied to the SSRIA crystal (the actual output gray level of this image has been boosted so that the tri-bars can be seen – the image directly out of the camera is approximately 1-bit over background). The right side of Figure 5.3.1-2 shows the corresponding image with the amplifier pump laser applied to the SSRIA crystal. The gray level is now at the saturation level of the IR camera indicating an optical gain of greater than 500. Also note that the image resolution is not degraded by the SSRIA.
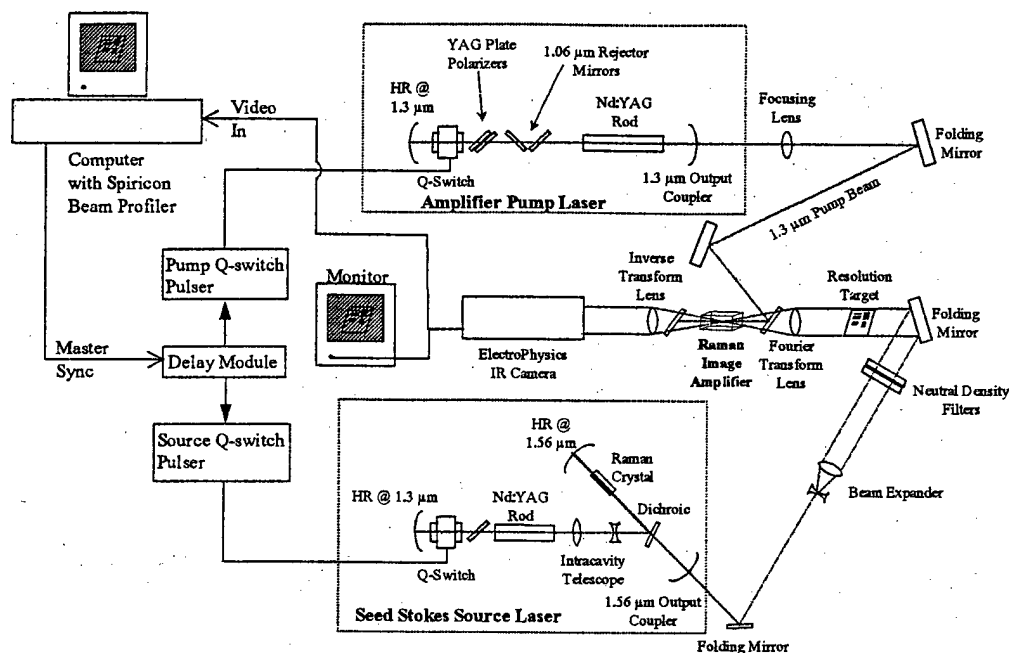
Figure 5.3.1-1 SSRIA Breadboard Demonstrator

Raw Image   Amplified Image
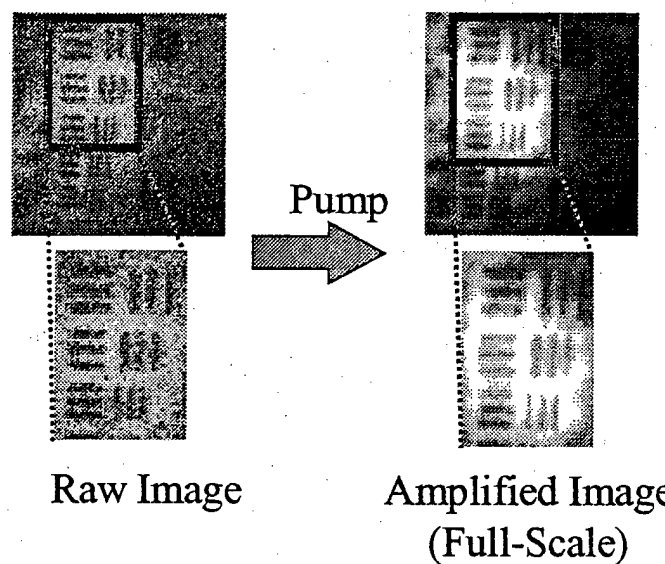(Full-Scale)

**Figure 5.3.1-2 Comparison of Unamplified and Raman Amplified Images of Air
Force Resolution Target**

5.3.2 Range-gating

The tri-bar resolution target, illuminated by the seed Stokes beam, is imaged into the

nonlinear crystal. The seed Stokes image light is amplified by stimulated Raman

scattering in the crystal. Since the seed Stokes light is only amplified if the pump light is present inside the crystal, by controlling the relative timing between the outgoing seed Stokes pulses and the Q-switched pump pulses, the range of the scene imaged can be selected. The effective "range-gate" width is controlled by the temporal pulse width of the pumps. shows the range-gating feature of SSRIA. Starting at the top left of the figure, the upper block shows a single tri-bar image that is unamplified because, as is shown in the block directly below it, the amplifier pump pulse (the wider trace) does not overlap the illuminating Stokes pulse (the narrower trace). The successive images and oscilloscope traces follow to the right and then from left to right at the bottom. These images show the amplification as a function of the temporal overlap between the illuminating Stokes pulses and the amplifier pump pulses in the Raman crystal. Each set shows the result of shifting the timing between the Stokes pulse and the amplifier pump pulse by 5 nanoseconds. Note the mismatch between the widths of the Stokes pulses and the amplifier pump pulses. The Stokes pulses are nominally 5 nanoseconds FWHM, while the amplifier pump pulses are nominally 30 nanoseconds FWHM. The effective temporal width of amplification is seen to be about 15 nsec, which corresponds to a range gatewidth of 2.25 meters in air.
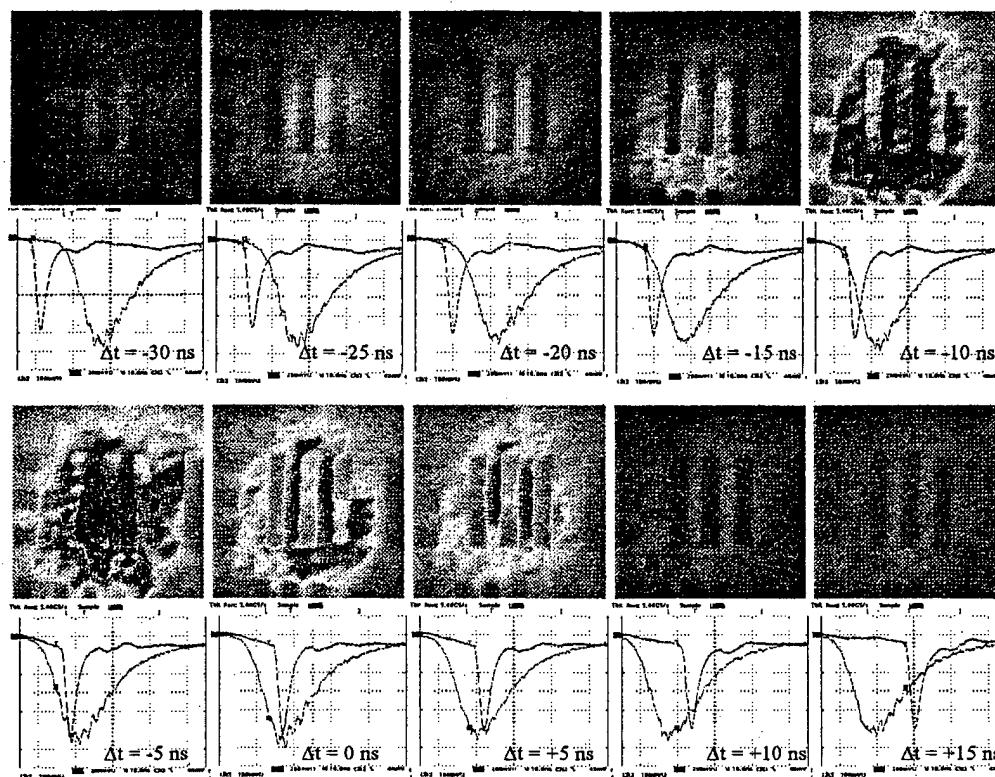
Figure 5.3.2-1 Range-gated images acquired using SSRIA.
The top figures show the amplified images of an AF resolution target. The bottom figures show the relative transmitter (red) and receiver (green) pulse profiles in the plane of the SSRIA. The relative time delays are denoted in 5 ns increments.

5.3.3 Resolution

For the experimental demonstration of SSRIA described in this dissertation, the system MTF is a product of the MTF's due to diffraction, optical aberrations, and the SSRIA. The demonstration was designed such that the SSRIA MTF would be the limiting term in the optical resolution. Figure 5.3.3-1 shows a theoretical plot of the contribution of each MTF term and the combined MTF for the breadboard demonstration.

In the experiment, one inch optics were chosen for convenience. The clear aperture of the Fourier transform lens was 19.2 mm. However, since the $Ba(NO_3)_2$ crystal used had

dimensions of 10mm x 10mm x 44 mm, the limiting aperture stop was the crystal itself. The optical cutoff frequency for a limiting aperture of 10 mm is:

$$\rho_c = \left|\frac{d}{f\lambda}\right| = 42.7 \text{ cycles per millimeter} \qquad (5.2)$$

The MTF contribution due to optical aberrations was estimated by a raytrace analysis of the SSRIA optical system. The geometrical blur size at the IR camera was determined to be approximately 8.6 μm in diameter. Assuming that the optical aberrations result in a Gaussian MTF with a standard deviation of $\sigma = 0.51r$, where r is the blur radius, the MTF due to optical aberrations is

$$MTF_{aberrations} = \exp\left(-2\pi^2\sigma^2\rho^2\right) \qquad (5.3)$$

where ρ is the optical frequency in cycles per millimeter.
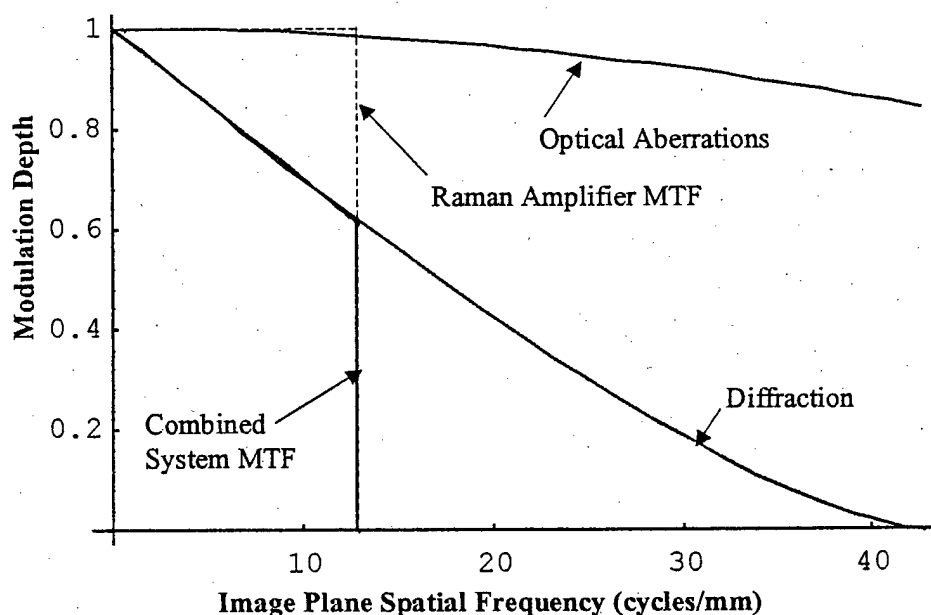
Figure 5.3.3-1 Combined MTF of Experimental Demonstration

The cutoff frequency of the SSRIA is controlled by the diameter of the pumped region, d, and the focal length of the inverse Fourier transform lens, f_2, by the equation:

$$\rho_{SSRIA} = \left| \frac{d}{f_2 \lambda} \right| \qquad (5.4)$$

In this demonstration, the focal length was chosen for convenience and the pumped region diameter was limited by the pulse energy available from the pump laser. For follow-on work, the pumped region will be increased to 5 mm and the inverse transform lens will be chosen to demonstrate a cutoff frequency of greater than 40 line pairs per millimeter. This will exceed the best resolution of current image intensifier tubes.

Figure 5.3.3-2 Amplified Image of Resolution Group +3

Figure 5.3.3-2 shows a typical amplified image of the resolution target with Group +3 centered in the picture. In this image, Element 5 was resolvable. Since Group +3, Element 5 corresponds to a resolution value of 12.7 cycles per millimeter, this confirms the MTF model for the SSRIA.

6 Raman Image Amplifier System Applications

6.1 Eye-safe Imaging Lidar

The SSRIA has the potential to improve on the current state of image intensifier and streak tube performance, particularly in the infrared where photocathode intensifiers have poor quantum efficiency. It offers the potential of being less expensive, simpler, more rugged, and having higher performance than current sensor devices.

Applications for military use include eye-safe imaging lidars that can be used for autonomous vehicle identification and targeting at 20 km and greater ranges, such as required by the Air Force's ERASER program. Reduced background radiation through narrow receiver spectral bandwidths and increased range resolution from short amplifier laser pulsewidths are realizable with SSRIA sensors. The increased range resolution will also improve clutter rejection. SSRIA also has the potential to perform optical image processing functions that will allow automatic target recognition or aimpoint designation in real-time without the need for extensive digital signal computations. This is readily accomplished in SSRIA by pre-filtering the optical image before amplification. Matched-filtered output from the image amplifier can be obtained. A suitable threshold can then be applied to this image to produce an all-optical automatic target recognition process.

6.2 Optical Image Processing

In most lidar system today, image enhancement and automatic target detection (ATD) are performed by an image processing computer after the image data has been collected.

SSRIA has the flexibility to perform real-time, Fourier-plane pre-processing of optical images. Figure 6.2-1 shows a schematic diagram of how this can be accomplished. Active and/or passive filters can be added in a Fourier-plane of the image to filter out undesirable spatial frequencies. The resulting filtered image is then amplified through the SSRIA and collected on a detector. The filters can be passive or active matched-filters providing a real-time, optical processing ATD routine. Phase-screens could also be used to amplify phase-objects which may be invisible to direct imaging.

Figure 6.2-1 shows an incoming low-level image of a resolution target. The optical filter function is a cross-shaped bandpass filter with a central ring obscuration to filter out the low spatial frequency intensity variation across the image. This filter is applied in an intermediate Fourier-plane of the image. The resulting filtered image is then amplified by SSRIA and the final amplified image shows much improved contrast of the resolution bars.
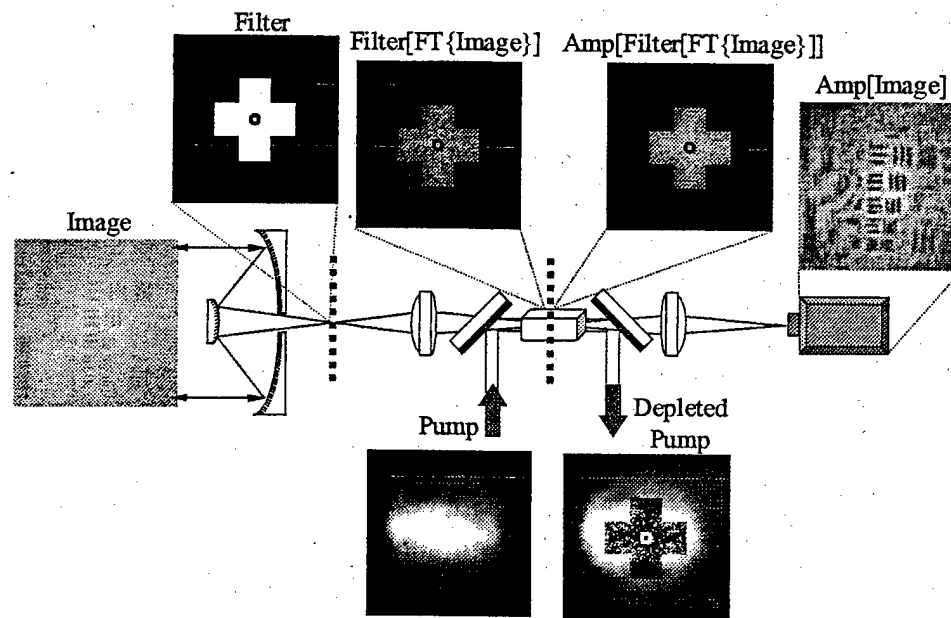
Figure 6.2-1 Filtered Fourier-Plane Image Amplification

Another application of optical image processing has been named RAPOD for "Raman Amplified Phase Object Detection." Certain objects are invisible to standard imaging lidar systems because they involve only a shift in optical phase rather than an amplitude contrast. These objects are called *phase objects* and they are typically associated with a varying index of refraction over the imaged scene. In air, these refractive index variations can be caused by a sharp pressure shock wave such as the supersonic shock wave caused by the passing of a supersonic airplane or missile. Other phase objects of interest are strong air turbulence and the wingtip vortices shed by all aircraft wings when generating lift.

Transparent phase objects can be characterized by an amplitude transmittance function

$$t(x,y) = \exp\left[i\varphi(x,y)\right] \tag{6.1}$$

where $\varphi(x,y)$ is the spatially varying phase shift of the phase object. If the phase shift is smaller than 1 radian, the amplitude transmittance can be approximated by

$$t(x,y) \cong 1 + i\varphi(x,y) \qquad (6.2)$$

where terms of the order of φ^2 and higher are neglected. The first term of Equation (6.2) leads to a strong wave component that passes through the phase object without change. The second term generates a weaker component of diffracted light that is deflected away from the axis of the system. In a conventional imaging system, the image produced by the phase object is given by

$$I_i \cong \left|1 + i\varphi\right|^2 \cong 1 \qquad (6.3)$$

where the term φ^2 has been dropped to maintain consistency.

In 1935, Fritz Zernike[54] realized that the diffracted component is not visible because it is in phase quadrature with the strong background. He proposed modifying this phase quadrature relationship by inserting a phase-changing plate in the focal plane. The strong background component is brought to a focus on-axis in the focal plane while the diffracted light is spread away from the focal point. By placing a phase-changing plate in the focal plane that consists of a glass substrate with a small dielectric dot deposited at the focal point (i.e. on the optical axis), the phase of the strong background component can be shifted relative to the diffracted component. For example, if the dot causes a phase shift of $\pi/2$ radians relative to the phase retardation of the diffracted light, the intensity in the image plane becomes

$$I_i = \left| \exp\left[i\left(\frac{\pi}{2}\right) \right] + i\varphi \right|^2 = \left| i(1+\varphi) \right|^2 \cong 1 + 2\varphi \qquad (6.4)$$

Therefore, the image intensity is now linearly related to the phase shift φ and exhibits positive phase contrast. This is the principle of the Zernike phase-contrast microscope.

Figure 6.2-2 shows an expanded view of the RAPOD system. The RAPOD system consists of a crystal of $Ba(NO_3)_2$ that is pumped by a Nd:YAP or Nd:YAG power oscillator configuration. The phase-object scene illuminated by the seed Stokes beam is imaged to a phase contrast plate (located in a Fourier plane), which has a small dielectric dot on-axis for shifting the phase of the background light relative to the diffracted light of the phase object. The phase-shifted image is then relayed to a second Fourier plane located at the center of the Raman crystal. The seed Stokes image light is amplified by stimulated Raman scattering in the crystal. Since the seed Stokes light is only amplified if the pump light is present inside the crystal, by controlling the relative timing between the outgoing seed Stokes pulses and the Q-switched pump pulses, the range of the scene imaged can be selected. The effective "range gate" width is controlled by the temporal pulse width of the pumps. The proposed Q-switched system can produce pump pulse widths on the order of 10 nanoseconds, giving an effective range-gate on the order of 1.5 meters. By using mode locking of the seed Stokes source and the Nd:YAP pump laser, it is possible to produce pulses on the order of 20-30 picoseconds, resulting in effective range gates of 3-4 millimeters. With range gates this short, it will be possible to image through very turbid media, amplifying only the unscattered "ballistic" photons and rejecting the photons which have been multiply scattered by the media.
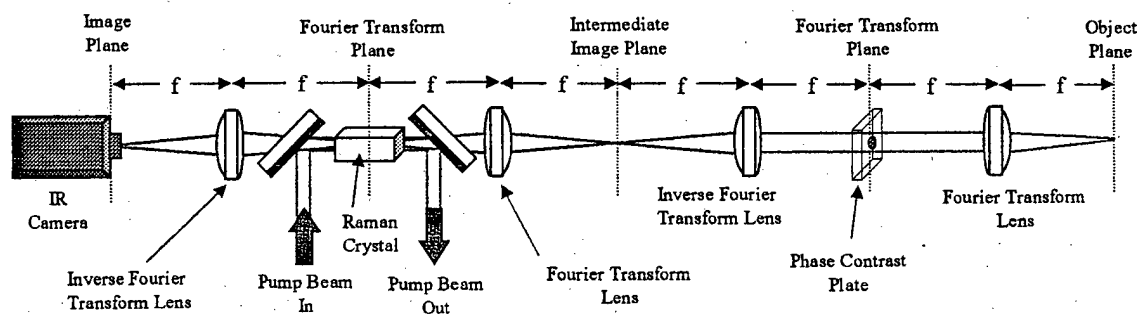
Figure 6.2-2 Raman amplified phase object detection layout

6.3 Marine Lidar

Other applications of Raman image amplification include underwater imaging of mines and submarines. Mine countermeasure (MCM) systems require high resolution, high sensitivity sensor subsystems to perform the functions of mine classification and mine identification. LIDAR-based mine detection systems, which are currently being added to the Navy's inventory, are limited in their ability to provide identification of the mine-like objects which they detect. The term "identification" in this context means associating a sensed mine-like object with a label that is unique to the target's external shape and configuration. In practical terms, this means that the sensing element must provide sufficiently high spatial resolution so that the image of a particular bottom mine, for example, can be distinguished from a discarded oil drum or some other bottom debris.

Range-gated marine LIDAR systems typically employ a pulsed laser transmitter (usually a frequency doubled Nd:YAG laser at a wavelength of 532 nm) and either intensified CCD cameras or photomultiplier tubes as receivers. Range gating is accomplished by controlling the timing between the outgoing laser pulses and the gating

or exposure of the sensing element of the LIDAR system. Image intensifier tubes operate by using a photoemissive detector coupled to a microchannel plate (MCP) electron amplifier. Current commercial image intensifiers are limited to gains of around 10^5, gating times of around 10 to 20 nanoseconds, and resolutions of around 50 to 100 μm at the photocathode. The resolution is primarily limited by the MCP blur. The signal-to-noise ratio (SNR) of the range-gated image is degraded by the quantum efficiency of the photocathode (typically < 40%) and the noise figure of the MCP (a degradation of SNR due to the electron multiplication statistics of the MCP).

The technique of SSRIA can outperform current image intensifiers and offers potential gains of 10^6, gating times of 1-5 nanoseconds (or even as short as 10-30 picoseconds by using laser mode-locking techniques), and resolution of 5-10 μm or smaller. The application of SSRIA to the marine LIDAR problem is called MArine Raman Image Amplification (MARIA).

Figure 6.3-1 shows a schematic of the MARIA LIDAR concept. The blue/green laser transmitter is an all-solid-state laser consisting of a pumped laser crystal and an external cavity, second harmonic generator (SHG). The optical frequency is then down-shifted to the first Stokes output frequency by an external cavity Raman crystal. The Stokes output illuminates the object and is diffusely reflected back to the receiver telescope optics. The resulting image is relayed to the solid-state Raman image amplifier which is configured in a Fourier transform arrangement where the amplifier crystal is at the Fourier transform plane of the input image.
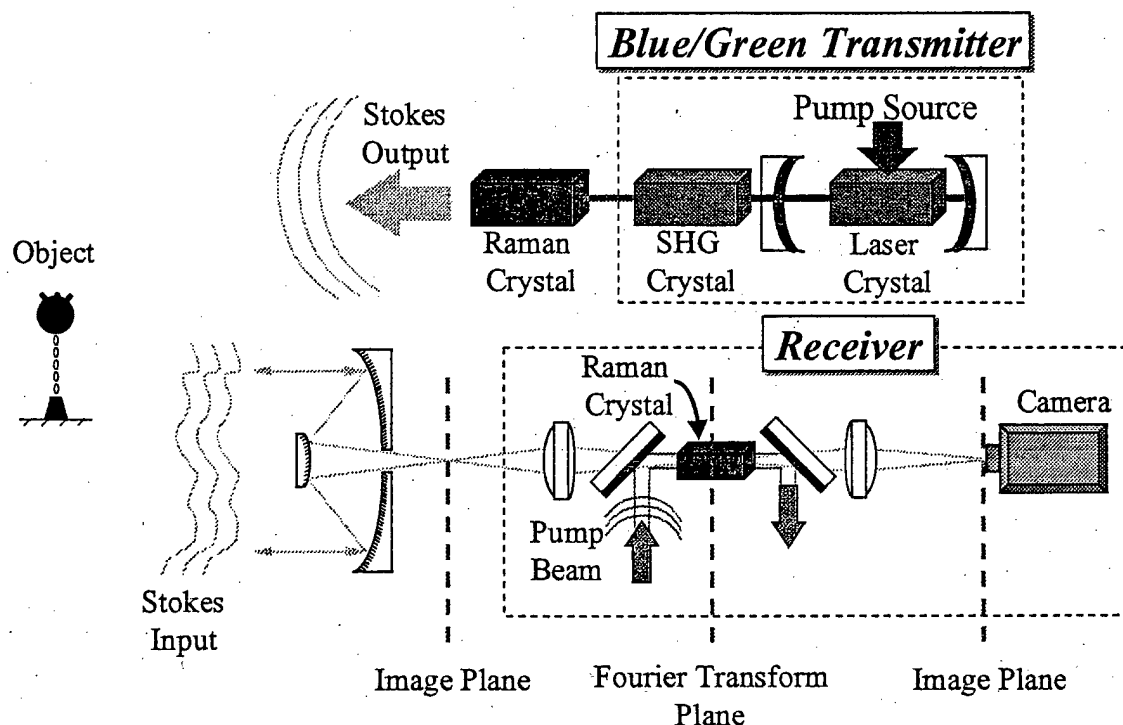
Figure 6.3-1 MARIA LIDAR Concept

The Raman image amplifier crystal is pumped by a beam from a second Q-switched, doubled solid-state laser. The Raman amplification process only occurs when the pump light is present in the Raman crystal. Therefore, the temporal pulsewidth of the amplifier pump laser determines the range-gatewidth of the resulting amplified image.

In order to quantify the performance difference of using a MARIA LIDAR system over other currently available underwater imaging systems, a set of common parameters was used to calculate the matched-filter SNR of a particular target. Both 1 nsec and 3 nsec effective gatewidths were evaluated for the MARIA system. These were compared with an imaging system based on a streak tube (STIL), a system based on a range-gated ICCD, and a laser line scan system. The LIDAR system parameters used for MARIA are shown in Table 6-1.

Table 6-1 MARIA system parameters

Parameter	Value
Optical wavelength, λ	563 nm
Laser pulse energy, Q	0.1 J
Transmitter half angles, $\theta_{x,y}$	0.011 rad
Receiver half angles (pixel), $\theta_{x,y}$	0.0005 rad
Receiver area, A_{rcvr}	$\frac{1}{4}\pi(0.18)^2$ m^2
Amplifier Noise Factor (see Section 2.4.2)	2
Raman gain	1000

The target parameters used for all cases is given in Table 6-2.

Table 6-2 Target Parameters

Parameter	Value
Radius, ρ_0	0.5 m
Area, $A_{trgt} = \pi\rho_0^2$	0.25π m^2
Reflectance, R	0.08

The parameters used for the STIL are given in Table 6-3.

Table 6-3 STIL system parameters

Parameter	Value
Optical wavelength, λ	532 nm
Laser pulse energy, Q	0.1 J
Transmitter half angles,	
Along track: θ_x	0.0005 rad
Cross track: θ_y	0.25 rad
Receiver half angles (pixel),	
Along track: θ_x	0.0005 rad
Cross track: θ_y	0.0005 rad
Receiver area, A_{rcvr}	$\frac{1}{4}\pi(0.18)^2$ m^2
Photodetector quantum efficiency, η_q	0.1

The system parameters for the ICCD system are given in Table 6-4.

Table 6-4 ICCD system parameters

Parameter	Value
Optical wavelength, λ	532 nm
Laser pulse energy, Q	0.1 J

Transmitter half angles, $\theta_{x,y}$	0.011 rad
Receiver half angles (pixel), $\theta_{x,y}$	0.0005 rad
Receiver area, A_{rcvr}	$\frac{1}{4}\pi(0.18)^2 \text{ m}^2$
Photodetector quantum efficiency, η_q	0.1

Finally, the system parameters used for the laser line scan case are given Table 6-5.

Table 6-5 Laser line scan system parameters

Parameter	Value
Optical wavelength, λ	532 nm
Laser power, P	1.5 W
Transmitter half angles, $\theta_{x,y}$	0.00025 rad
Transmitter offset, y_{xmtr}	-1.0 m
Receiver half angles (pixel), $\theta_{x,y}$	0.032 rad
Receiver offset, y_{rcvr}	1.0 m
Receiver area, A_{rcvr}	$\frac{1}{4}\pi(0.18)^2 \text{ m}^2$
Photodetector quantum efficiency, η_q	0.1
Full scan angle, Θ	0.5 rad (28 deg)
Scan time	0.0667 sec

All system parameters were chosen to be representative of current state-of-the-art devices. The scan time and laser power of the laser line scan system was selected to deposit the same laser energy over the scan as used with the other systems. This means that any differences in SNR will be due to the detailed detection processes of each system and not due to any differences in illumination.

Figure 6.3-2 shows the Jerlov[55] ocean water types with I, II, and III being clear ocean water types and 1, 4, 5, 7, and 9 being coastal water types. Notice that the irradiance transmittance for Jerlov coastal type 4 is fairly flat between 532 nm and 563 nm. Thus there is no significant difference between using the Stokes-shifted wavelength at 563 nm and the standard doubled Nd:YAG wavelength at 532 nm for Jerlov coastal type 4. This

is true for most of the coastal water types, with the more turbid cases such as types 7 and 9 being slightly more transmissive at 563 nm.
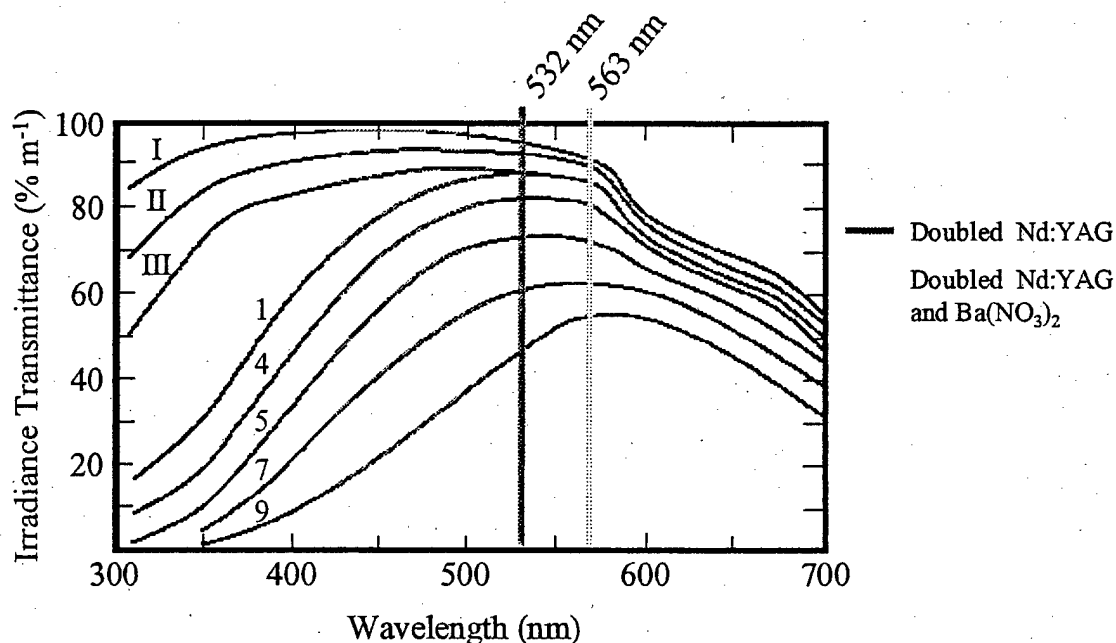
Figure 6.3-2 Jerlov Water Types

Figure 6.3-3 shows the performance comparison between all the system types. The differences between the various curves are primarily due to two factors. The first factor is the effective gatewidth employed by the system. The first curve, MARIA (1 nsec), represents the optimum performance which can be obtained in this type of coastal water. The temporal spreading due to multiple scattering is just under 1 nsec for the round trip through the water column. Thus any shorter effective gatewidth would result in a lower SNR. To achieve this performance, the MARIA system would have to employ pulses of around 1 nsec FWHM. This would present a major challenge to the amplifier pulse laser. The second curve, MARIA (3 nsec), would employ pulses of less than 3 nsec FWHM.

This is still challenging for the amplifier pulse laser but can be achieved through the use of cavity-dumping techniques.

The difference between the MARIA (3 nsec) and the STIL (3 nsec) performance is due to the second factor, which is the effective quantum efficiency of detection. As discussed in the Amplifier Theory Section, the MARIA system has an overall effective quantum efficiency of 50%. That is, the SNR noise power factor approaches the limiting value of 2 as the gain is increased. In the STIL system the effective quantum efficiency is 10% due to the lower quantum efficiency of the photocathode and the noise factor of the MCP.

The effective range gate used for the ICCD system is 25 nsec (or about 9 feet). This assumes a transmitter pulsewidth of 15 nsec, which is typical for the underwater imaging LIDAR systems in use today.[2]

Given a criterion for detection of SNR = 10 dB, the target detection depths achievable with each system are given in Table 6-6.
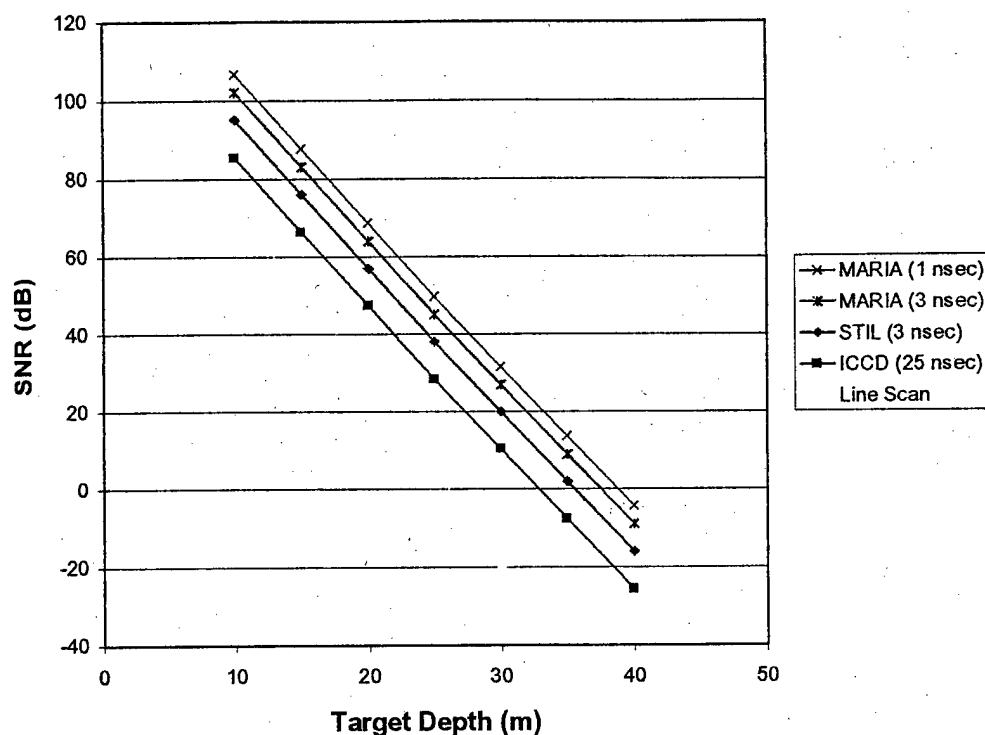
Figure 6.3-3 Performance Comparison of MARIA with STIL, ICCD, and Laser Line Scan Systems

Table 6-6 Target Detection Depths (SNR = 10 dB criterion)

System	Detection depth, D	Diffusion lengths, KD
MARIA (1 nsec)	37 m	8.0
MARIA (3 nsec)	36	7.8
STIL (3 nsec)	32	6.9
ICCD	30	6.5
Laser line scan	23	5.0

A design study was performed to determine the optimum design for the Stokes seed laser used to illuminate underwater targets. Four candidate pulsed laser designs were considered: 1. Flashlamp-pumped, Q-switched Nd:YAG; 2. Flashlamp-pumped, Q-switched and cavity dumped Nd:YAG; 3. Flashlamp-pumped, Q-switched and mode

locked Nd:YAG; and 4. Flashlamp-pumped, Nd:YAG regenerative amplifier (regen).
Flashlamp-pumped lasers were chosen for their low relative cost.

The standard Q-switched Nd:YAG laser design is shown in Figure 6.3-4. All of the
Stokes seed laser designs are shown with the second harmonic generator (SHG) and the
external Raman crystal. The pulse shape of the Q-switched Nd:YAG is governed by the
gain characteristics of the laser medium and the pulse width is typically 10 – 20 nsec.
With high optical pumping and by shortening the resonator as much as possible, the
lower limit of a standard Q-switched Nd:YAG is about 8 nsec. This temporal limit is far
greater than the pulse stretching caused by multiple scattering in typical ocean waters.
Thus the full SNR potential of range-gating is not reached by a standard Q-switched
Nd:YAG.
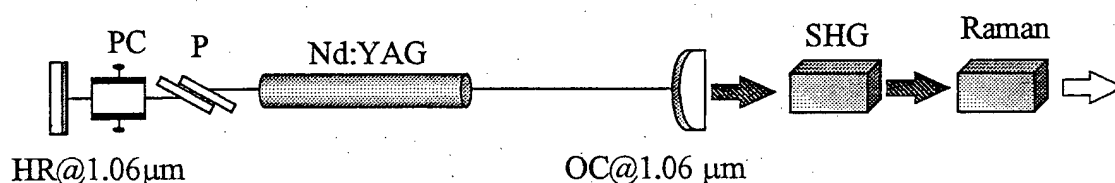
Figure 6.3-4 Q-Switched Nd:YAG

Figure 6.3-5 shows the second candidate laser design, the Q-switched and cavity-
dumped Nd:YAG. In a cavity dumped laser, both end mirrors of the laser cavity are
essentially 100% reflectors. When the flashlamp is fired, the Q-switch is held at a low
retardation voltage, which results in the horizontally polarized fluorescence being
transmitted through the thin-film polarizer and prevents lasing. Upon reaching peak
energy storage in the Nd:YAG rod, the Pockels cell is biased to its half-wave retardation
voltage. The resulting vertically polarized light is now reflected by the polarizer to the

other HR and the laser pulse energy begins to build up. When the Q-switched pulse power in the cavity reaches a maximum, the bias is quickly removed from the Pockels cell. The cavity energy is then transmitted through the polarizer, essentially dumping the entire cavity within one round-trip. The width of the laser pulse, τ_P, is then given by:

$$\tau_P \approx \frac{2L}{c} \qquad (6.5)$$

and for a short 0.5 m cavity is about 3.3 nsec. This cavity-dumped design can produce almost as much energy per pulse as the standard Q-switched design and is operated at the same range of PRF. The cost is somewhat higher due to the more demanding Q-switch electronics required to switch quickly.
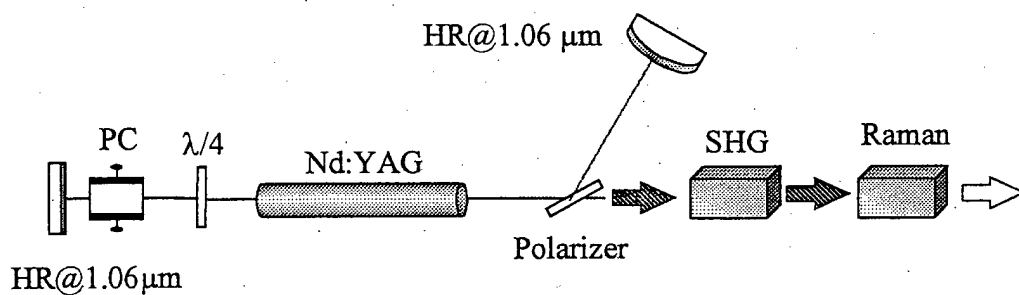
Figure 6.3-5   Q-Switched & Cavity Dumped Nd:YAG

Figure 6.3-6 shows the third candidate design, the Q-switched and mode locked Nd:YAG. By placing an amplitude modulator inside the laser cavity and driving it at exactly the frequency separation of the axial modes, the laser can be induced to generate a train of mode-locked pulses with a PRF of $f_m = c/2L$. The inclusion of a Q-switch in the laser cavity results in a burst of mode-locked pulses that are contained within the envelope of a 100 – 200 nsec Q-switch pulse. The individual mode-locked pulses are between 10 and 30 psec FWHM with an energy of up to 10 mJ at the peak of the Q-

switch envelope. These narrow pulses will be rapidly spread by the multiple scattering in ocean water and will approach 1 nsec in width on the return path. Thus the temporal (and, therefore, range) resolution afforded by using 30 psec pulses cannot be realized in an underwater environment. In addition, the PRF of the mode-locked pulses is much too frequent to allow pulses to propagate to an underwater target and return before the emission of another pulse. Thus the returns of many pulses at many different ranges will be superimposed, causing SNR degradation.
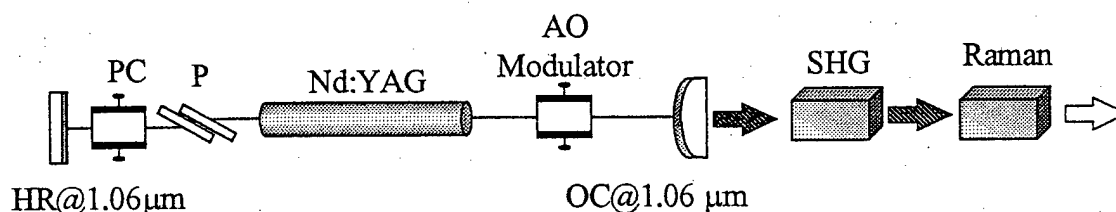

Figure 6.3-6 Q-Switched & Mode Locked Nd:YAG

The fourth candidate design, the regenerative amplifier, allows a way to produce individual picosecond pulses at lower PRF's, thus avoiding the overlap of pulse returns at different ranges. This laser system consists of a mode-locked oscillator, which provides low-energy, mode-locked pulses, and a regenerative amplifier, which selects and traps an individual mode-locked pulse, amplifies it greatly, and switches it back out. To understand the operation of the regenerative amplifier, consider a horizontally polarized pulse from a mode-locked oscillator that is transmitted through the polarizer in Figure 6.3-7. The horizontally polarized pulse will experience a 45° rotation at the $\lambda/2$ plate and a further 45° rotation from the Faraday rotator. The now vertically polarized pulse reflects from the polarizer into the laser resonator. After passing through the $\lambda/4$ plate and reflecting from the HR, the pulse once again passes through the $\lambda/4$ plate resulting in

a horizontally polarized pulse traveling toward the right. As soon as the pulse leaves the Pockels cell traveling toward the right, the Pockels cell voltage is quickly switched to $\lambda/4$ retardation. Therefore, when the pulse next makes its round trip through the $\lambda/4$ plate and Pockels cell, it remains horizontally polarized and is trapped inside the cavity. After many passes in the resonator, the energy of the pulse reaches a maximum due to gain saturation. At this point, the Pockels cell is switched to $\lambda/2$ retardation voltage. The pulse now experiences a 90° polarization rotation and the vertically polarized pulse is reflected by the two polarizers to the output port of the laser system.

The regenerative amplifier design can produce 30 psec pulses at a repetition rate up to 10 kHz with a pulse energy of up to 5 mJ. Although the regen solves the problem of overlapping mode-locked pulses as exhibited by the third design, the pulse energy is still small and the 30 psec pulses are rapidly stretched to 1 nsec by the ocean water.
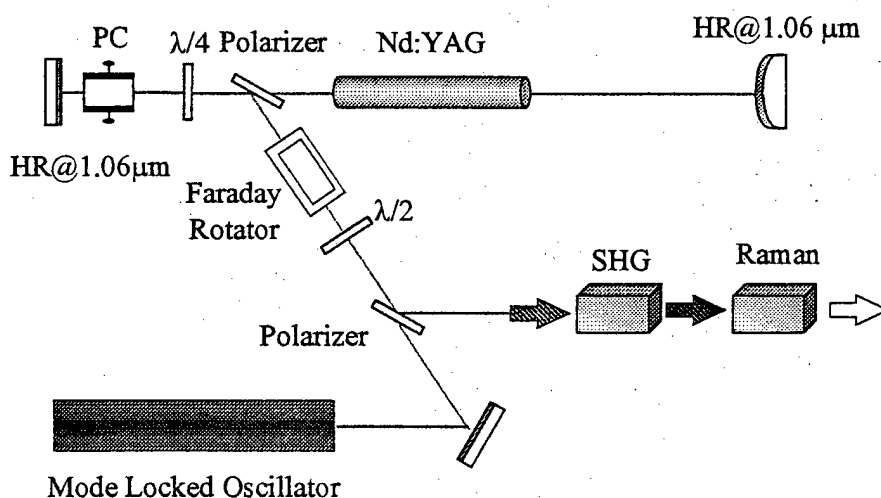

Figure 6.3-7 Regenerative Amplifier

Table 6-7 shows a summary comparison of the four candidate Stokes seed laser designs. Based on the desire to match the temporal spreading expected from multiple

scattering in the ocean and, thereby, to realize the optimum performance in terms of range resolution and water backscatter rejection, the best candidate for MARIA is the Q-switched and cavity dumped design. This design will provide the best overall performance within reasonable bounds for cost.

Table 6-7 Laser System Trade-off Comparison

Laser Pulsing Type	Pulsewidth (nsec)	PRF (Hz)	Pulse Energy (mJ)	Relative Cost
Q-switched	8 – 10	1 – 100	100 – 500	Low
Q-switched & cavity dumped	**3 – 5**	**1 – 100**	**100 – 200**	**Medium**
Q-switched & mode locked	10 – 30 psec	100 – 300 MHz	1 – 10	Medium
Regen	10 – 30 psec	1 – 10 kHz	< 5	High

The first Stokes output will be frequency doubled using an uncoated 8x8x10 mm^3 LBO crystal cut for type I non-critical phase matching ($\Theta=90°$, $\phi=0°$). The phase matching temperature of 42°C is maintained by enclosing the crystal in a temperature controlled oven. LBO was chosen as the doubling material because it exhibits a superior acceptance bandwidth ($\Delta T \cdot L \cong 6°$ C·cm) and damage threshold (>1 GW/cm2) over other candidate materials. Previous experimental results have shown that the doubling efficiency is around 55%.

The cutoff frequency of the MARIA is controlled by the diameter of the pumped region, d, and the focal length of the inverse Fourier transform lens, f_2, by the equation:

$$\rho_{MARIA} = \left| \frac{d}{f_2 \lambda} \right| \qquad (6.6)$$

The pumped region will be increased to 5 mm in diameter and the inverse transform lens will be chosen to demonstrate a cutoff frequency of greater than 40 line pairs per millimeter. This will exceed the best resolution of current image intensifier tubes.

The limiting resolution of the receiver is only half of the story for a marine imaging system. The resolution of images presented to the receiver is degraded by other factors related to the propagation of light in the turbid medium of ocean water. First, there is the image blur due to the forward scattering nature of the intervening water. This effect can be quantified by the point spread function of the water column (also called the beam spread function).[56,57] Essentially, the reflected light distribution from the illuminated object is convolved with the point spread function of the water, thereby blurring the image. This phenomena affects any type of imaging system, be it a range-gated imager or a laser line scan system. The second effect of imaging through water is that water backscatters the illuminating laser beam and this backscattered light adds to the light reflected from a target, thereby washing out the inherent contrast.[58] It is this effect which all active marine imaging systems seek to minimize. In a range-gated system, such as MARIA, the backscattered light is minimized by only opening the receiver to receive the light reflected from a definite range. By minimizing the width of the range gate, the amount of backscattered light is minimized. This has the effect of minimizing the veiling light due to the surrounding water, and maximizing target image contrast. In a laser line scanned system, the backscattered light is minimized by using a bistatic configuration. The laser output aperture is physically separated from the receiver aperture and their

respective fields-of-view only overlap near the target. Any water appearing in the overlap backscatters light to the receiver and degrades contrast.

A recent study by Ronald E. Walker and John W. McLean[59] has derived lidar equations for turbid media with the inclusion of pulse stretching caused by multiple scattering. Included in this work was an analytical comparison of the contrast transfer function (CTF) of a range-gated imaging (RGI) system with the CTF produced by a comparable laser line scanned (LLS) system. Figure 6.3-8 shows the results of this computation for the Coastal Ocean case presented in

Table 6-8. The contrast and SNR are plotted as a function of spatial frequency for a depth, D, corresponding to 4, 6, and 8 beam attenuation lengths for the CO case (i.e., $c \cdot D = 4, 6, or 8$). As shown in Figure 6.3-8, the CTF produced by both the imaging lidar system and the laser line scan system has a cutoff near 1 cycle/cm.

Figure 6.3-8 SNR and Contrast (CTF) calculations for shot-noise-limited LLS (solid) and RGI (dashed) systems at 4, 6 and 8 beam attenuation lengths in Coastal Ocean (CO) waters.

Table 6-8 Summary of Water Types

Water Type	c (m^{-1})	ω_0	k (m^{-1})
Coastal Ocean (CO)	0.398	0.551	0.22
Turbid Harbor (TH)	2.19	0.833	0.67

(c is the beam attenuation coefficient, ω_0 is the single scattering albedo, and k is the diffuse attenuation coefficient of ocean water) [60]

Figure 6.3-8 shows that at 4 beam attenuation lengths there is very little difference in the two types of imaging systems. However, at 6 and 8 beam attenuation lengths the range-gated imaging system outperforms the LLS system in terms of image contrast. This is a consequence of the increased overlap of the transmitter and receiver fields-of-view in the LLS at longer ranges. The increased overlap leads to more backscattered light admitted to the image. The RGI system rejects the backscattered light through use of a narrow range-gate, which is essentially independent of the object range (pulse stretching by the water may cause some increase of backscatter with range).

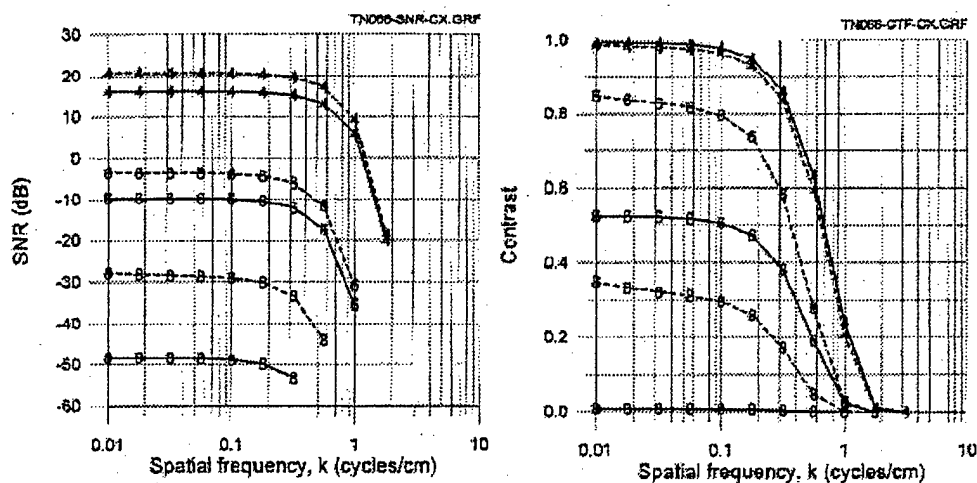Figure 6.3-10 shows the SNR and CTF comparison in Turbid Harbor (TH) waters.
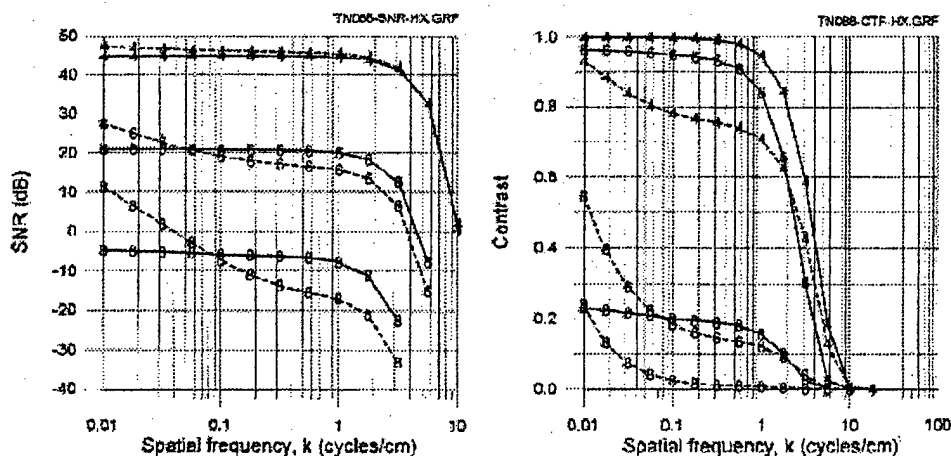

Figure 6.3-10   SNR and Contrast (CTF) calculations for shot-noise-limited LLS (solid) and RGI (dashed) systems at 4, 6 and 8 beam attenuation lengths in Turbid Harbor (TH) waters.

As shown in Figure 6.3-10, although the ultimate spatial frequency cutoff for the two systems is the same (around 10 cycles/cm), the RGI system shows much reduced contrast at intermediate spatial frequencies due to the increased amount of glow/blur caused by forward scattering of light emanating from surrounding areas of the target being imaged into other areas. Because of the narrow field-of-view of the LLS system, there is less glow present and, therefore, the image contrast is higher. In effect, the LLS system is equivalent to a high-pass filter on the image. The forward glow/blur manifests itself as a low spatial frequency noise source. Forward glow rejection can be implemented in LRG systems by affecting the same high-pass filter *before* detection as the LLS systems. In MARIA this can be done by using an optical high-pass filter (see Section 6.2). The MARIA optical architecture utilizes Fourier Transform (FT) imaging, which allows real-time optical pre-processing of the signal (image) via FT-plane intensity and/or phase masks. Standard ICCD-based LRG systems cannot use this blur/glow rejection technique because the filtering can only be performed after detection, and therefore after detector noise has been added. Therefore, *MARIA offers the blur/glow rejection capabilities of the LLS, but with the single-shot imaging capabilities of the LRG.*

The CTF of a marine imaging system depends not only on the turbidity of the ocean water, but also on the specific fields-of-view, effective gatewidths, pulsewidths, and other system parameters. It is not clear that either the imaging lidar or the laser line scan system is generally the winner in terms of contrast performance or image resolution. It is clear that a marine imaging system based on MARIA can produce high resolution images at competitive ranges (or depths) in most of the required ocean waters.

6.4 Medical Lidar

Medical applications would include imaging through highly scattering media. The SSRIA sensor would enable amplification and detection of ballistic photons transmitted through tissue with very high range resolution. This resolution would enable production of 3 dimensional images of small millimeter dimension targets such as tumors.

A modification of Raman imaging technology has potential for imaging sub-surface skin carcinomas. By using mode-locking technology, the Raman illuminator and amplifier pump laser pulses can be temporally compressed to tens of picoseconds FWHM. The resulting gate for Raman imaging would allow separation of the "ballistic" photons, which pass unscattered through soft tissue, from the multiply scattered photons, which would normally mask the desired image. Mahon, et al., have demonstrated that features as small as 125 μm can be imaged through dense scattering media with light extinction factors of up to e^{-33} using Raman image amplification in Hydrogen gas.[17] By using solid-state Raman image amplification, a medical imaging device can be made smaller and more compact, with even higher spatial resolution. The technology transfer could result in much earlier detections of carcinomas, particularly those associated with Melanomas.

7 Conclusions

In conclusion, this dissertation has shown that Solid-state Raman Image Amplification is a feasible technology for producing range-gated imagery in the eye-safe infrared. SSRIA is capable of amplifying low-level optical images with gains of 10^3 to 10^6 with the addition of only quantum-limited noise. The high gains available from SSRIA can compensate for low quantum efficiency detectors in the SWIR and can reduce the need to cool detectors to reduce thermal noise. The range-gate of SSRIA was shown to be controlled by the pulsewidth of the amplifier pump laser and can be made as short as $30 - 100$ cm, using pump pulses of $2 - 6.7$ nsec FWHM. The use of SSRIA in an imaging lidar system has been shown to result in higher SNR images throughout a broad range of incident light levels, in contrast to the increasing noise factor occurring with reduced gain in ICCDs. General equations for the gain, noise, and optical design of SSRIA have been presented. A theoretical framework for the optical resolution in SSRIA has been presented and it was shown that SSRIA can be designed to produce higher resolution than is attainable by ICCDs. SSRIA was also shown superior to ICCDs in rejecting unwanted sunlight background, further increasing the SNR of images. Lastly, it was shown how SSRIA can be combined with optical pre-filtering to perform optical image processing functions such as image enhancement and automatic target detection/recognition.

References

[1] D. Sliney and M. Wolbarsht, *Safety with Lasers and Other Optical Sources,* Plenum Press, New York (1980)

[2] B. L. Ulich, P. Lacovara, S. E. Moran, and M. J. DeWeert, "Recent results in imaging lidar," in *Advances in Laser Remote Sensing for Terrestrial and Oceanographic Applications,* R. M. Narayanan, J. E. Kalshoven, Jr., Editors, *Proceedings of SPIE* Vol. 3059, pp. 95 – 108 (1997)

[3] I. P. Csorba, *Image Tubes,* Howard W. Sams & Co., Indianapolis, Indiana (1985)

[4] C. V. Raman and K. S. Krishnan, "A new type of secondary radiation," *Nature* (London) **121,** p. 501 (1928)

[5] C. V. Raman, "A change of wavelength in light scattering," *Nature* (London) **121,** p. 619 (1928)

[6] G. Landsberg and S. Mandel'shtam, "A New Effect in the Scattering of Light in Crystals," *Naturwissenschaften* **16,** p. 557 (1928)

[7] A. Smekal, *Naturwissenschaften* **11,** p. 875 (1923)

[8] H. A. Kramers and W. Heisenberg, *Z. Phys.* **31,** p. 681 (1925)

[9] G. Venkataraman, *Journey into Light: Life and Science of C. V. Raman,* Oxford University Press, New Delhi (1988)

[10] E. J. Woodbury and W. K. Ng, *Proc. IRE* **50,** p. 2347 (1962)

[11] E. J. Woodbury and G. M. Eckhardt, U.S. Patent No. 3,371,265 (27 February 1968)

[12] R. Frey and F. Pradere, *Opt. Comm.,* **12,** p. 98 (1974); T. R. Loree, et. al, *IEEE J. Quant. Electron.,* **QE-15,** p. 337 (1979)

[13] J. P. Partanen and M. J. Shaw, "High-power forward Raman amplifiers employing low-pressure gases in light guides. I. Theory and applications," *JOSA-B* **3** (10), pp. 1374-1389 (1986)

[14] M. D. Duncan, R. Mahon, L. L. Tankersley, and J. Reintjes, "Low-light-level, quantum-noise-limited amplification in a stimulated Raman amplifier," *JOSA-B* **9** (11), pp. 2107-2121 (1992)

[15] J. T. Murray, R. C. Powell, N. Peyghambarian, D. Smith, W. Austin, and R. A. Stolzenberger, "Generation of 1.5-μm radiation through intracavity solid-state Raman shifting in Ba(NO$_3$)$_2$ nonlinear crystals," *Opt. Lett.* **20** (9), pp. 1017-1019 (1995)

[16] J. A. Moon, R. Mahon, M. D. Duncan, and J. Reintjes, "Three-dimensional reflective image reconstruction through a scattering medium based on time-gated Raman amplification," *Opt. Lett.* **19** (16), pp. 1234-1236 (1994)

[17] R. Mahon, M. D. Duncan, L. L. Tankersley, and J. Reintjes, "Time-gated imaging through dense scatterers with a Raman amplifier," *Applied Optics* **32** (36), pp. 7425-7433 (1993)

[18] P. W. Milonni and J. H. Eberly, *Lasers*, John Wiley and Sons, New York, p. 284 (1988)

[19] A. E. Siegman, *Lasers*, University Science Books, Mill Valley, CA, pp. 428-430 (1986)

[20] A. E. Siegman, *Lasers*, University Science Books, Mill Valley, CA, pp. 502-503 (1986)

[21] P. W. Milonni and J. H. Eberly, *Lasers*, John Wiley and Sons, New York, p. 297 (1988)

[22] M. G. Raymer and I. A. Walmsley, "The quantum coherence properties of stimulated Raman scattering," *Progress in Optics XXVIII*, E. Wolf, ed., Elsevier Science Publishers, New York (1990)

[23] P. W. Milonni and J. H. Eberly, *Lasers*, John Wiley and Sons, New York, p. 644 (1988)

[24] S. Wolfram, *Mathematica*, 2nd Edition, Addison-Wesley Publishing Co., Redwood City, CA, pp. 696-703 (1991)

[25] H. Heffner, "The Fundamental Noise Limit of Linear Amplifiers," *Proceedings of the IRE,* pp. 1604-1608 (July 1962)

[26] E. Desurvire, *Erbium-Doped Fiber Amplifiers: Principles and Applications,* John Wiley and Sons, Inc., New York, pp.68 – 72 (1994)

[27] C. M. Caves, "Quantum limits on noise in linear amplifiers," *Phys. Rev. D* **26** (8), pp. 1817-1839 (1982)

[28] J. A. Levenson, K. Bencheikh, D. J. Lovering, P. Vidakovic and C. Simonneau, "Quantum noise in optical parametric amplification: a means to achieve noiseless optical functions," *Quantum Semiclass. Opt.* **9**, pp. 221-237 (1997).

[29] S. O. Rice, "Statistical Properties of a Sine Wave Plus Random Noise," *Bell System Technical Journal*, Vol. 27, pp. 109-157 (1948)

[30] H. A. Haus and J. A. Mullen, "Quantum noise in linear amplifiers," Phys. Rev., Vol. 128 (5), pp. 2407-2413 (1962)

[31] R. Loudon, *The Quantum Theory of Light*, second edition, Oxford University Press, New York (1983)

[32] W. Heitler, *The Quantum Theory of Radiation*, third edition, Dover Publications, Inc., New York (1984)

[33] M. O. Scully and M. S. Zubairy, *Quantum Optics*, Cambridge University Press, Cambridge (1997)

[34] M. Sargent III, M. O. Scully, and W. E. Lamb, Jr., *Laser Physics*, Addison-Wesley, Reading, MA (1974)

[35] P. Meystre and M. Sargent III, *Elements of Quantum Optics*, Springer-Verlag, New York (1990)

[36] K. Shimoda, H. Takahasi, and C. H. Townes, "Fluctuations in amplification of quanta with application to maser amplifiers," *J. Phys. Soc. Japan* 12 (6), pp. 686-700 (1957)

[37] P. Diament and M. C. Teich, "Evolution of the statistical properties of photons passed through a traveling-wave laser amplifier," *IEEE J. Quantum Electron.* 28 (5), pp. 1325-1334 (1992)

[38] E. B. Rockower, N. B. Abraham, and S. R. Smith, "Evolution of the quantum statistics of light," *Phys. Rev. A* 17 (3), p.1100 (1978)

[39] Y. Y. Yamamoto, "Noise and error rate performance of semiconductor laser amplifiers in PCM-IM optical transmission systems," *IEEE J. Quantum Electron.* 16 (10), p. 1073 (1980)

[40] B. R. Frieden, *Probability, Statistical Optics, and Data Testing*, Springer-Verlag, New York, p. 73 (1983)

[41] J. W. Goodman, *Statistical Optics*, John Wiley & Sons, New York, p. 473 (1985)

[42] M. Abramovitz and I. A. Stegun, *Handbook of Mathematical Functions*, Dover Publications, New York, chapters 15 and 22 (1972)

[43] R. J. Glauber, "Coherent and incoherent states of the radiation field," *Phys. Rev.* 131 (6), pp. 2766-2788 (1963)

[44] J. Perina, *Quantum Statistics of Linear and Nonlinear Optical Phenomena*, D. Reidel Publishing, Boston, p. 129 (1984)

[45] E. L. Dereniak and D. G. Crowe, *Optical Radiation Detectors*, John Wiley & Sons, New York, p. 18 (1984)

[46] C. H. Henry and R. F. Kazarinov, "Quantum noise in photonics," *Rev. Mod. Phys.* **68** (3), pp. 801-853 (1996)

[47] R. Kubo, *Rep. Prog. Phys.* **29**, p. 255 (1966)

[48] H. B. Callen and T. A. Welton, *Phys. Rev.* **83**, p. 34 (1951)

[49] L. D. Landau and E. M. Lifshitz, *Statistical Physics*, Addison-Wesley, Reading, MA (1958)

[50] P. R. Battle, R. C. Swanson, and J. L. Carlsten, "Quantum limit on noise in a Raman amplifier," *Phys. Rev. A* **44** (3), pp. 1922-1930 (1991)

[51] J. A. Levenson, I. Abram, Th. Rivera, and Ph. Grangier, "Reduction of quantum noise in optical parametric amplification," *J. Opt. Soc. Am. B* **10** (11), pp. 2233-2238 (1993)

[52] S. E. Moran, B. L. Ulich, W. P. Elkins, R. L. Strittmatter, and M. J. DeWeert, "Intensified CCD (ICCD) dynamic range and noise performance," in *Ultrahigh and High-speed Photography and Image-Based Motion Measurement, Proceedings of SPIE* Vol. 3173 (1997)

[53] I. P. Csorba, *Image Tubes*, Howard W. Sams, p. 81 (1985)

[54] F. Zernike, "Das Phasenkontrastverfahren bei der Mikroskopischen Beobachtung," *Z. Tech. Phys.*, **16**, p. 454 (1935)

[55] N. G. Jerlov, *Marine Optics*, Elsevier Science, Amsterdam, p. 133 (1990)

[56] J. W. McLean, J. D. Freeman, and R. E. Walker, "Beam spread function with time dispersion," *Applied Optics* **37** (21), pp. 4701-4711 (1998)

[57] J. W. McLean and K. J. Voss, "Point spread function in ocean water: comparison between theory and experiment," *Applied Optics* **30** (15), pp. 2027-2030 (1991)

[58] J. R. Apel, *Principles of Ocean Physics*, Academic Press, New York, p. 589 (1987)

[59] R. E. Walker and J. W. McLean, "Lidar equations for turbid media with pulse stretching," Areté Associates Report #REW-TN066, April 1998.

[60] G. A. Maul, *Introduction to Satellite Oceanography*, Martinus Nijhoff Publishers, Dordrecht, Netherlands, Chapter 4 (1985)